2017

INCORPORATING SEASONAL WIND RESOURCE AND ELECTRICITY PRICE DATA INTO WIND FARM MICROSITING

Timothy A. Pfeiffer
University of Massachusetts - Amherst, tapfeiffer@umass.edu

INCORPORATING SEASONAL WIND RESOURCE AND ELECTRICITY PRICE DATA INTO WIND FARM MICROSITING

A Thesis Presented

By

TIMOTHY PFEIFFER

Submitted to the Graduate School of the
University of Massachusetts Amherst in fulfillment
of the requirements for the degree of

MASTER OF SCIENCE IN MECHANICAL ENGINEERING

May 2017

Mechanical Engineering

INCORPORATING SEASONAL WIND RESOURCE AND ELECTRICITY PRICE DATA INTO WIND FARM MICROSITING

A Thesis Presented

By:

TIMOTHY PFEIFFER

Approved as to style and content by:

_____
Matthew Lackner, Chair

_____
Erin Baker, Member

_____
James Manwell, Member

_____
Sundar Krishnamurty, Department Head
Mechanical Engineering

ABSTRACT

INCORPORATING SEASONAL WIND RESOURCE AND ELECTRICITY PRICE DATA INTO WIND FARM MICROSITING

MAY 2017

TIMOTHY PFEIFFER
B.S., UNIVERSITY OF OKLAHOMA
M.S.M.E., UNIVERSITY OF MASSACHUSETTS AMHERST

Directed By: Professor Matthew Lackner

Currently, most micrositing techniques aim to maximize annual energy production (AEP) or minimize cost of energy (COE) with no direct regard to revenue. This research study developed a method that utilizes the seasonal electricity price and wind data to microsite wind farms in terms of profitability. To accomplish this, six candidate wind farms with differing layouts and spacing were selected at a given location. They were then simulated using a wake modeling software to produce expected power outputs at different wind speeds, wind directions, and turbulence intensities. By interpolating the power output tables with wind data, a power time-series was created for each wind farm over a multi-year period. Electrical price was then incorporated with the power time-series to produce a revenue time-series of the revenue produced at each hour over the same time-period. Each relative wind farm was then rotated in increments to evaluate new candidate wind farms and revenue totals. This method is site specific and results may differ dependent on location and seasonal correlation between wind and electrical data. Overall, the method looks to exploit a different approach to the micrositing problem.

TABLE OF CONTENTS

Page

ABSTRACT ..... **iii**

LIST OF TABLES ..... **vii**

LIST OF FIGURES ..... **ix**

CHAPTER

1. INTRODUCTION **1**

2. BACKGROUND **4**

2.1 Offshore Wind 4
2.2 Wake Effects 5

2.2.1 Wake Meandering 9
2.2.2 Power Loss due to Wakes 9
2.2.3 Wake Models 11

2.2.3.1 Low-Fidelity Models 11
2.2.3.2 Medium-Fidelity Models 12
2.2.3.3 High-Fidelity Models 14
2.2.3.4 Wake Model Comparison 15

2.2.4 Important Meteorology Parameters and Wake Effect Impacts 16

2.2.4.1 Turbulence Intensity 16
2.2.4.2 Atmospheric Stability 17

2.2.5 Deep Array Effect 18

2.3 Methodologies for the Micrositing of Wind Farms 19

2.3.1 Objective Functions 21
2.3.2 Modeling of the Wind Resource 23

3. METHODOLOGY 27

3.1 Objective Function.....31
3.2 Wind Farm Layouts 32
3.3 Simulation Tools.....37

3.3.1 TurbSim 38
3.3.2 FAST and AeroDyn 38
3.3.3 DWM 39

3.3.3.1 Quasi-Steady Wake Deficit and Wake Meandering 40
3.3.3.2 Turbulence Effects 40
3.3.3.3 DWM Output 40

3.4 Metocean Data Set for Offshore Wind 41
3.5 ISO New England Power Data 44

4. RESULTS AND DISCUSSION 47

4.1 Wind Farm Power Tables 47

4.1.1 6X6 Square Wind Farm with 6D Spacing 47
4.1.2 9X4 Rectangular Wind Farm with 6D Spacing 49
4.1.3 9X4 Rectangular Wind Farm with 4D and 8D Spacing 51
4.1.4 6X6 Square Wind Farm with 8D Spacing 53
4.1.5 9X4 Rectangular Wind Farm with 8D Spacing 54
4.1.6 9X4 Rectangular Wind Farm with 6D and 10D Spacing 56
4.1.7 Power Drop for the 9X4 Rectangular Farms with 6D and 8D Spacing.....57

4.2 Metocean Buoy Data Analysis for Nantucket 58

4.2.1 Climatology for the Nantucket Buoy Location.....59
4.2.2 Power Time-Series.....64

4.3 Wind Farm Revenue 66

4.3.1 SE ISO New England Electricity Data 66
4.3.2 Revenue for the 6X6 Square Wind Farm with 6D Spacing.....68

4.3.2.1 Revenue for the Orientations of the 6X6 Square Wind Farm with 6D Spacing 70

4.3.3 Summary of the Various Wind Farms and Their Orientations.....74

5. CONCLUSIONS 77

APPENDICES

A. TIME-SERIES ELECTRICAL DATA FOR ISO NEW ENGLAND REGIONS OTHER THAN SEMASS 80

B. POWER TIME-SERIES FOR THE CANDIDATE WIND FARMS 83

C. REVENUE TIME-SERIES, ORIENTATIONS, AND TOTALS FOR THE REMAINING CANDIDATE WIND FARMS 85

D. MATLAB SCRIPTS FOR THE DWM 105

BIBLIOGRAPHY 109

LIST OF TABLES

Table **Page**

2.1 Atmospheric Stability Classes per the Obukhov Length [39] 18

3.1 Wind Speed, Wind Direction, and Turbulence Intensity Parameters 36

4.1 Average Total Power for all 36 Turbines in the 6X6 Farm with 6D Spacing (MW).....48

4.2 Summation of the Average Total Power for all 36 Turbines in the 6X6 Farm with 6D Spacing (MW) 49

4.3 Average Total Power for all 36 Turbines in the 9X4 Farm with 6D Spacing (MW).....50

4.4 Summation of the Average Total Power for all 36 Turbines in the 9X4 Farm with 6D Spacing (MW) 50

4.5 Average Total Power for all 36 Turbines in the 9X4 Farm with 4D and 8D Spacing (MW) 52

4.6 Summation of the Average Total Power for all 36 Turbines in the 9X4 Farm with 4D and 8D Spacing (MW).....52

4.7 Average Total Power for all 36 Turbines in the 6X6 Farm with 8D Spacing (MW).....53

4.8 Summation of the Average Total Power for all 36 Turbines in the 6X6 Farm with 8D Spacing (MW) 54

4.9 Average Total Power for all 36 Turbines in the 9X4 Farm with 8D Spacing (MW).....55

4.10 Summation of the Average Total Power for all 36 Turbines in the 9X4 Farm with 8D Spacing (MW) 55

4.11 Average Total Power for all 36 Turbines in the 9X4 Farm with 6D and 10D Spacing (MW) 56

4.12 Summation of the Average Total Power for all 36 Turbines in the 9X4 Farm with 6D and 10D Spacing (MW).....57

4.13 Conclusions for the Total Revenue and Orientation of Each Wind Farm 75

4.14 Conclusions for the Total Power and Orientation of Each Wind Farm 76

LIST OF FIGURES

Figure **Page**

2.1 (a) Wind resource in the United States (NREL) compared with, (b) population concentration [19] 4

2.2 Wake effect model using the actuator disk [1] 6

2.3 Simulation using LES with a scale-dependent dynamic model: averaged velocity (top), turbulence intensity (middle), kinematic shear stress (bottom) [7]....8

2.4 Wake meandering in space and in the Trefftz plane [49] 9

2.5 Power loss at the Horns Rev offshore wind farm [14]....10

2.6 Power loss at the North Hoyle wind Farm [40] 10

2.7 Relationship between the wind turbine and the near and far wakes [12]....11

2.8 Wind farm modeling using the SOWFA model [30]....15

2.9 Comparison between wake models: left (high-fidelity), middle (low-fidelity), right (medium-fidelity) [23]....16

2.10 TI and wind speed relation at the Horns Rev wind farm. Data has been binned to show the mean value (solid line) [15] 17

2.11 Wake merging in the Horns Rev wind farm [4] 19

2.12 LES simulation with a wind farm layout that has fewer rows, but more turbines per row [56] 23

2.13 Wind rose with differing sector numbers [8] [9] [10]....24

2.14 Weibull distribution for a wind speed of 6 m/s [53]....26

3.1 Flow chart of the micrositing process....30

3.2 6X6 square wind farm with 6D spacing 33

3.3 9X4 rectangular wind farm with 6D spacing....33

3.4 9X4 rectangular wind farm with 4D and 8D spacing 34

3.5 6X6 square wind farm with 8D spacing 34

3.6 9X4 rectangular wind farm with 8D spacing 35

3.7 9X4 rectangular wind farm with 6D and 10D spacing 35

3.8 6X6 square wind farm with 5° orientation 36

3.9 Relationship between turbulence intensity and wind speed for real observations, NTM, and ONT90 [77] 37

3.10 Wake meandering simulation modeled by the DWM [40] 38

3.11 Flow chart of the DWM [40] 39

3.12 Metocean database buoy locations [70] 42

3.13 Metocean wind data from Nantucket buoy location over 5-years 42

3.14 Histogram of the normalized 90m hub height wind speed at the Nantucket buoy location 43

3.15 5-year wind rose for the Nantucket location 43

3.16 ISO New England wholesale power regions in Massachusetts [29] 44

3.17 5-year time-series price and power data from Southeastern Massachusetts, including Nantucket 45

3.18 Histogram of the electrical price data for the Southeastern Massachusetts area 45

3.19 Histogram of the 5-year electrical demand data for the Southeastern Massachusetts area 46

4.1 Power drop for the 9X4 rectangular farm with 6D and 8D spacing at 90° 58

4.2 Power drop for the 9X4 rectangular farm with 6D and 8D spacing at 80° 58

4.3 Wind speed and direction averages for each season over the 5-year period 59

4.4 5-year seasonal averages at the SE Nantucket buoy location 60

4.5 Histogram of the spring wind speed for the 5-year period 60

4.6 Wind rose for the 5-year spring months at Nantucket 61

4.7 Histogram of the summer wind speed for the 5-year period 61

4.8 Wind rose for the 5-year summer months at Nantucket 62

4.9 Histogram of the fall wind speed for the 5-year period 62

4.10 Wind rose for the 5-year falls months at Nantucket 63

4.11 Histogram of the winter wind speed for the 5-year period 63

4.12 Wind rose for the 5-year winter months at Nantucket 64

4.13 Power time-series for the 6X6 square wind farm, 6D spacing, with a 0° orientation.....64

4.14 5-year mean power outputs for all relvative wind farms 65

4.15 5-year seasonal average power price and demand measurements from Southeastern New England 66

4.16 5-year seasonal averages for the power price and demand in Southeastern New England 67

4.17 Wind speed and price versus price percentile.....68

4.18 Revenue time-series for the 6X6 square wind farm, 6D spacing, at a 0° orientation.....69

4.19 5-year seasonal average revenues and revenue sums for the 0° orientation of the 6X6 square wind farm with 6D spacing.....69

4.20 Revene for the 6X6 square wind farm with 6D spacing.....70

4.21 Relationship between the total revenues and total powers for the 6X6 square wind farm with 6D spacing 71

4.22 AEP versus revenue for the 6X6 square wind farm with 6D spacing 72

4.23 6X6 square wind farm with a 5° orientation 72

4.24 Wind rose for the 6X6 square wind farm, 6D spacing, with a 5° orientation 73

4.25 6X6 square wind farm, 6D spacing, with a 60° orientation 73

4.26 Wind rose for the 6X6 square wind farm, 6D spacing, with a 60° orientation 74

4.27 Revenue totals for each orientation of the candidate wind farms 76

A.1 Time-series of the electrical power demand in Northeastern Massachusetts 80

A.2 Time-series of the electrical price in Northeastern Massachusetts 80

A.3 Histogram of the electrical demand in Northeastern Massachusetts 80

A.4 Histogram of the electrical price in Northeastern Massachusetts 81

A.5 Time-series of the electrical demand for Western Massachusetts 81

A.6 Times-series of the electrical price for Western Massachusetts 81

A.7 Histogram of the electrical price in Western Massachusetts 82

A.8 Histogram of the electrical demand for Western Massachusetts 82

B.1 Power time-series for the 9X4 rectangular wind farm with 6D spacing 83

B.2 Power time-series for the 9X4 rectangular wind farm with 4D and 8D spacing 83

B.3 Power time-series for the 6X6 square wind farm with 8D spacing 84

B.4 Power time-series for the 9X4 rectangular wind farm with 8D spacing 84

B.5 Power time-series for the 9X4 rectangular wind farm with 6D and 10D spacing 84

C.1 5-year revenue time-series for the 9X4 rectangular wind farm, 6D spacing, with a 0° orientation 85

C.2 5-year seasonal revenue for the the 9X4 rectangular wind farm, 6D spacing, with a 0° orientation 85

C.3 Total revenue values for the the 9X4 rectangular wind farm with 6D spacing at each orientation 86

C.4 Relationship between the total revenues and total powers for the 9X4 rectangular wind farm with 6D spacing 86

C.5 Orientation that produces the most amount of power and revenue for the 9X4 rectangular wind farm with 6D spacing 87

C.6 Wind rose for the 9X4 rectangular wind farm when the orientation is 95° 87

C.7 Orientation that produces the least amount of power and revenue for the 9X4 rectangular wind farm with 6D spacing 88

C.8 Wind rose for the 9X4 rectangular wind farm when the orientation is 61° 88

C.9 5-year revenue time-series for the 9X4 rectangular wind farm, 4D and 8D spacing, at an orientation of 0° 89

C.10 5-year average revenues for each season 89

C.11 Total revenue values for each orientation of the 9X4 rectangular wind farm with 4D and 8D spacing 89

C.12 Total revenue and total power for each orientation of the 9X4 rectangular wind farm with 4D and 8D spacing 90

C.13 9X4 rectangular wind farm, 4D and 8D spacing, with a 98° orientation 90

C.14 Wind rose for the 9X4 rectangular wind farm, 4D and 8D spacing, with an orientation of 98° 91

C.15 9X4 rectangular wind farm, 4D and 8D spacing, with an orientation of 62° 91

C.16 Wind rose for the 9X4 rectangular wind farm, 4D and 8D spacing, with a 62° orientation 92

C.17 5-year revenue time-series for the 6X6 square wind farm with 8D spacing 92

C.18 5-year average revenue values for each season....93

C.19 Total revenue values for each orientation of the 6X6 square wind farm with 8D spacing....93

C.20 Total revenue and power values for the 6X6 square wind farm, 8D spacing, at each orientation....94

C.21 6X6 square wind farm, 8D spacing, with a 9° orientation to maximize power and revenue 94

C.22 Wind rose for the 6X6 square wind farm, 8D spacing, with a 9° orientation 95

C.23 6X6 square wind farm, 8D spacing, with a 60° orientation that minimizes power and revenue totals....95

C.24 Wind rose for the 6X6 square wind farm, 8D spacing, with an orientation of 60° 96

C.25 5-year revenue time-series for the 9X4 rectangular wind farm with 8D spacing 96

C.26 5-year seasonal revenue for the 9X4 rectangular wind farm with 8D spacing 97

C.27 Total revenue values for each orientation of the 9X4 rectangular farm with 8D spacing 97

C.28 Total revenue and power totals for each orientation of the 9X4 rectangular wind farm with 8D spacing....98

C.29 99° orientation that maximizes power and revenue for the candidate wind farm 98

C.30 Wind rose that maximizes power and revenue for the 9X4 rectangular wind farm with 8D spacing....99

C.31 Orientation that minimizes total power and revenue for the 9X4 rectangular wind farm with 8D spacing....99

C.32 Wind rose that minimizes total revenue and power for the candidate wind farm 100

C.33 5-year revenue time-series for the 9X4 rectangular wind farm with 6D and 10D spacing....100

C.34 5-year seasonal revenue for the 9X4 rectangular wind farm with 6D and 10D spacing....101

C.35 Revenue totals for each orientation of the candidate wind farm....101

C.36 Power and revenue totals for each orientation of the candidate wind farm....102

C.37 Orientation of the candidate wind farm that maximizes revenue and power....102

C.38 Wind rose that maximizes revenue and power for the candidate wind farm....103

C.39 Orientation that minimizes revenue and power for the candidate wind farm....103

C.40 Wind rose that minimizes revenue and power for the candidate wind farm....104

D.1 Script to run TurbSim....106

D.2 Script that alters the .wnd file for FAST....106

D.3 Script that changes the main input file for FAST....107

D.4 Script that runs and parallel processes the simulations for the DWM....108

CHAPTER 1

INTRODUCTION

Alternative energy sources such as wind energy are essential for a sustainable future as fossil fuels are depleted and continue to have a negative impact on the environment. Offshore wind energy, compared to land-based, has the potential to provide higher energy density, fewer restrictions on scale, and hopefully reductions in cost [63].

Wind farms are collections of wind turbines and the layout of these farms is an important design consideration to maximize output and profitability. Kinetic energy is extracted by the wind turbines from the incoming flow, which produces downstream wakes that are characterized by lower mean wind speeds and higher turbulence intensities. In a wind farm, the upstream wakes impinge on downstream turbines, reducing their output and increasing structural loads. The design of the wind farm layout (also called "micrositing") is therefore a critical engineering challenge, with the goal of minimizing the negative impacts of wakes. This concept and specific micrositing approaches have been extensively studied to improve the economic viability of wind farms [14] [37] [47].

This study considered the impact of orienting a wind farm based on temporal variations in the wind resource and electrical prices. While most wind farm micrositing optimization studies have looked at either maximizing the annual energy production (AEP) or minimizing the cost of energy (COE), none have considered the value of the energy produced and how the temporal variations (e.g. diurnal, seasonal, etc.) in the wind resource and electricity prices are related. The hypothesis of this study was that by

orienting a wind farm based on time-varying wind data (speed and direction), electrical consumption and price data, and subsequently maximizing revenue (integrating price x power) instead of AEP, a more profitable wind farm could be designed. This approach could lead to more valuable power being produced when the energy demand is at its highest even though productivity may be decreased. The analysis conducted in this research has assessed this hypothesis by simulation of wind farms including wakes coupled with site specific and concurrent wind resource and electric grid data.

To conduct this analysis, a few key tools and data sets were utilized. The Dynamic Wake Meandering Model (DWM) [41] is a software package used to simulate wake effects. This model can calculate the total power of a specific wind farm layout based on wind direction, turbulence intensity, and wind speed. In addition, meteorological data from a Nantucket buoy location was used from the metocean data set study conducted by Stewart, et al., (2015) [70]. This allows for a time-varying wind resource to be incorporated into the analysis of the farm, rather than just using conventional statistical averages. ISO New England power consumption and price data was used to quantify when consumers use the most power and when the cost of electricity is highest. Overall, this study aimed to better understand how the temporal variations in the wind resource, electricity consumption, and electrical price can be used to inform the micrositing process.

Chapter 2 provides background information on offshore wind, wake effects, optimization methods, and wind modeling. Chapter 3 outlines the flow chart process, objective function, sample wind farm layouts, wake modeling software, metocean data,

and ISO New England power consumption and price data used in this study. Chapter 4 presents the results and discussion. Chapter 5 highlights the conclusions.

CHAPTER 2

BACKGROUND

2.1 Offshore Wind

Onshore wind development in the United States has generally occurred in the central part of the country and near locations that tend to have lower population densities (Figure 2.1b). Due to these small populations, electricity demands are lower than other regions and create problems for wind energy developers, policy makers, and grid operators to match the energy supply with the energy demand. Mountain and hill tops also provide good wind resources for potential wind farms, but these areas can be challenging in the sense of competing uses, NIMBY concerns, and installation and access.

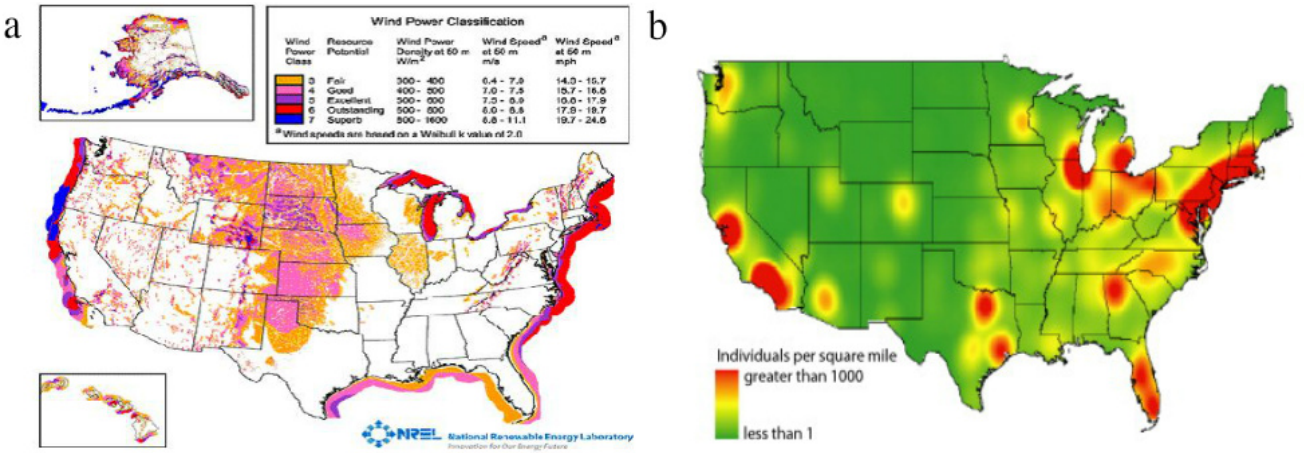

Figure 2.1 (a) Wind resource in the United States (NREL) compared with, (b) population concentration [19].

Offshore wind energy is a promising alternative because of the abundant wind resource near a large portion of the United States coast line (Figure 2.1a) and the proximity to large population centers. Offshore wind turbines (OWTs) can potentially be

placed in areas that are far from the coast, making them less of a controversy in terms of viewshed. These turbines have also been increasing in rotor diameter and are being built to heights where wind speeds are much stronger [19], allowing the turbines to produce more power. The size of current and future offshore turbines makes them almost impossible to install on land due to transportation challenges.

In 2016, Deepwater Wind constructed the very first offshore wind farm in the United States located off Block Island, RI. This project consists of five 6 MW turbines that produce power for the local community and other parts of New England [3].

2.2 Wake Effects

Because of economics of scale, it is generally more sensible to group wind turbines into a wind farm so that the fixed costs of site preparation, installation, accessibility, etc. are spread across many turbines. This allows overall higher power production compared to that of an individual turbine. The grouping of wind turbines in a wind farm, however, results in wake effects, which decrease the total power production and can reduce the lifetime of the rotors due to increased turbulence [66]. As ambient flow interacts with upstream turbines, kinetic energy is extracted. This results in the formation of wakes, which cause decreased wind speeds and higher turbulence intensities downstream. Therefore, downstream turbines experience larger fluctuating forces, and produce less power than the freestream turbines. Elliot, (1991) [27] states in his review that a 7-row array with 9-D row separation between turbines produced 20% less energy between the first and seventh rows. Other studies have indicated power losses between 5-8% when averaged over different wind directions [13].

Figure 2.2 shows a simple momentum theory model of a wake using an actuator disk. This model represents a wind turbine in an inviscid and incompressible flow with freestream velocity, U_∞. Since the disk extracts kinetic energy from the wind, the velocity gradually decreases to an average value downstream in the wake, U_w. To satisfy conservation of mass for a stream tube that encloses the disk, the cross-sectional area upstream is smaller than the areas that define the rotor and downstream cross-sectional areas [18] (Equation 2.1).

$$\dot{m} = \rho A_\infty U_\infty = \rho A_d U_d = \rho A_w U_w \tag{2.1}$$

Where A_∞, A_d, and A_w are the cross-sectional areas upstream, at the disk, and downstream.

The disk causes the static pressure to increase from p_∞ in the freestream to p^+_d, which then rapidly drops to p^-_d due to the force, F_D , exerted (Equation 2.2).

$$F_D = \dot{m}(U_\infty - U_w) = (p_d^+ - p_d^-)A_d \tag{2.2}$$

In the downstream wake, the velocity continues to decrease while the pressure gradually recovers to the ambient value p_∞ [66].

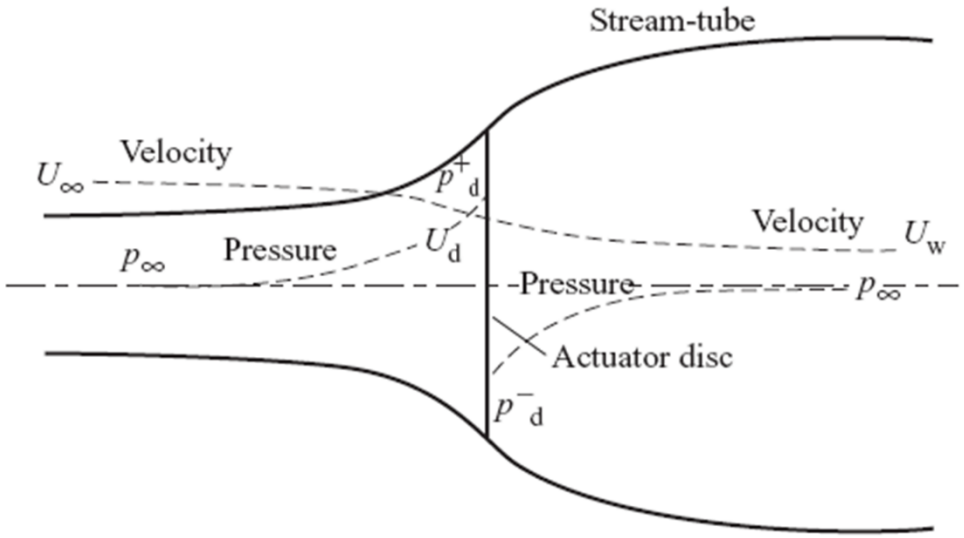

Figure 2.2: Wake effect model using the actuator disk [1].

The energy extracted by the rotor can also be expressed using the actuator disk momentum theory and is defined by Equation 2.3.

$$E = \frac{1}{2} m(U_\infty^2 - U_w^2) \tag{2.3}$$

Using the conservation of mass, momentum, and energy equations, the expressions for the power (P), power coefficient (C_p), and thrust coefficient (C_T) can be derived [18]. Equations 2.4, 2.5, and 2.6 show the final relations obtained using the actuator disk theory.

$$P = \frac{1}{2} \dot{m}(U_\infty^2 - U_w^2) \tag{2.4}$$

$$C_p = \frac{\frac{1}{2}(U_\infty + U_w)(U_\infty^2 - U_w^2)}{U_\infty^3} \tag{2.5}$$

$$C_T = \frac{T}{\frac{1}{2}\rho U_\infty^2 A_d} \tag{2.6}$$

As the velocity behind the turbine decreases, the wind velocity in the far wake can be shown to be less than the wind velocity that interacts with the disk. This creates a relationship between the cross-sectional area at the far wake, which is larger than the cross-sectional area at the disk. The larger the C_T value, the larger the cross-sectional area downstream [66].

In practice, the momentum theory model shown above is a major simplification, and viscous effects and turbulent mixing are critical processes that affect the wake behavior and recovery. The low velocity wake flow and the higher velocity freestream flow outside of the wake create a shear layer in which the flows mix. This shear layer continues to grow, causing the wake to recover as it progresses downstream, and is characterized by non-uniform turbulence and eddies [66]. Wake evolution depends on

turbulence levels in the atmosphere, wind shear effects, surface constraints, and topographic effects [79]. Ambient turbulence for offshore wind farms is often lower than onshore due to less friction with the surface layer [13]. Lower ambient turbulence typically leads to longer distances over which the wake recovers and larger wake velocity deficits [66]. Figure 2.3 shows a schematic designed by the EPFL Wind Engineering and Renewable Energy Laboratory [7] in which a large eddy simulation (LES) is incorporated with a scale-dependent dynamic model. The simulation shows the effects a rotor can have on the ambient flow downstream: decrease in wind velocity, large increase in turbulence intensity near the upper part of the turbine, and interaction between the free-stream velocity and waked flow, which eventually dissipates the effects.

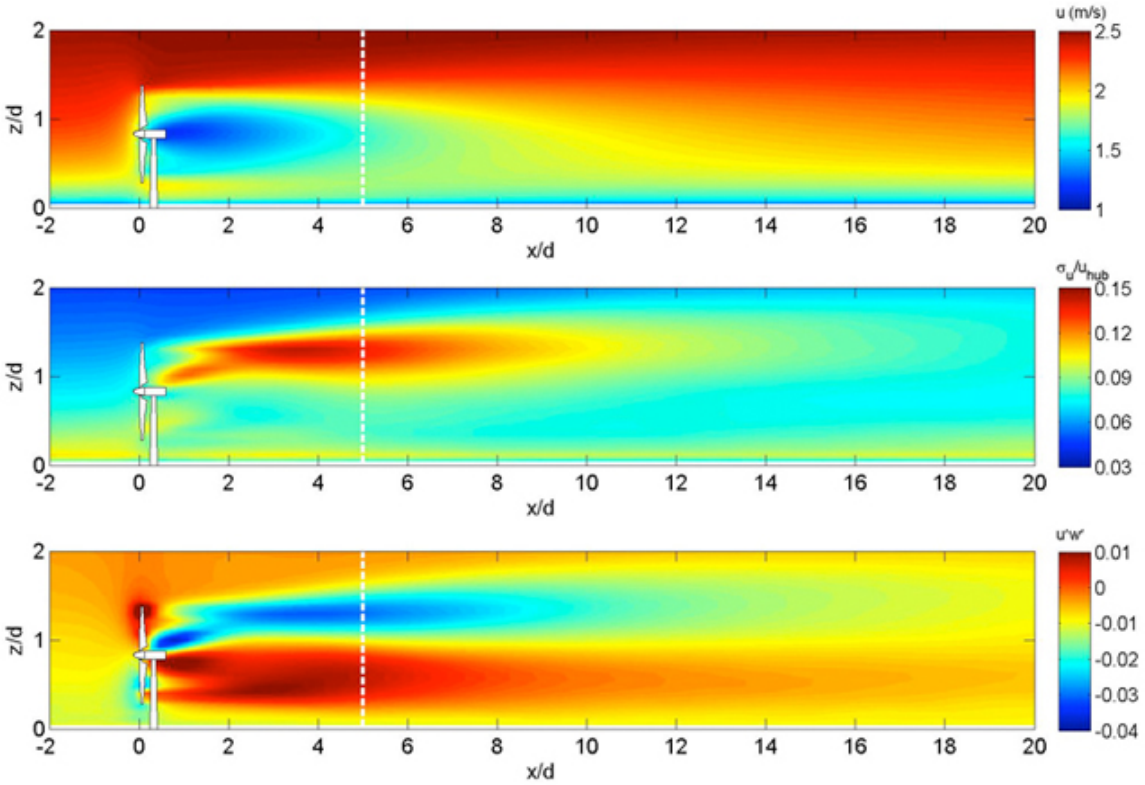

Figure 2.3: Simulation using LES with a scale-dependent dynamic model: averaged velocity (top), turbulence intensity (middle), kinematic shear stress (bottom) [7].

2.2.1 Wake Meandering

As the mixing region continues to grow, the incoming turbulence and large eddies in the atmosphere move the wake laterally and vertically [48]. This oscillation is known as wake meandering and characterizes the movement of the entire wake behind an upstream turbine (Figure 2.4). Due to its stochastic nature, the wake effects on a downstream turbine can be intermittent, including periods of undisturbed wind conditions.

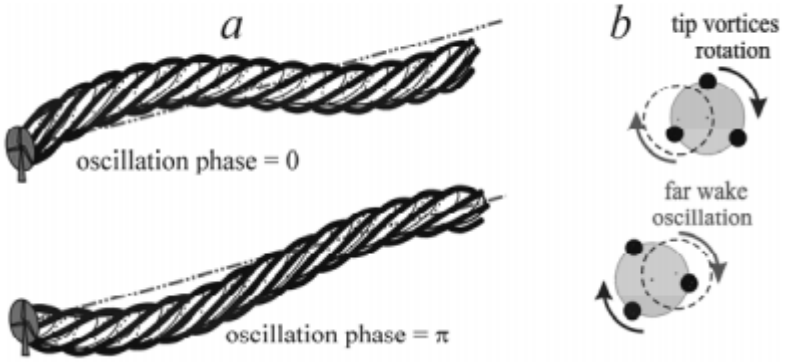

Figure 2.4: Wake meandering in space and in the Trefftz plane [49].

2.2.2 Power Loss due to wakes

Wakes cause a decrease in the power output of downstream turbines, with the most pronounced effect occurring between the first and second turbine in line. As the ambient wind is mixed into the wake region behind the second turbine, the turbulence increases and the wake recovers more quickly [66]. This may result in a similar or even higher wind speed for the third turbine and potentially a higher power output (Figure 2.6). From the third to the nth turbine in the row, the rotor power generally reaches an almost constant state, with variation depending on the atmospheric conditions, wind direction,

and equilibrium value of the turbulence. Figure 2.5 is taken from the work of Barthelmie et al., (2006) [14] where the analytical model derived by Frandsen et al., (2006) [32] is used to show the power loss for the Horns Rev offshore wind farm. Figure 2.6 from Hao et al., (2016) [40] illustrates the power at the North Hoyle wind farm from the Dynamic Wake Meandering Model (DWM) and OpenFOAM LES [51].

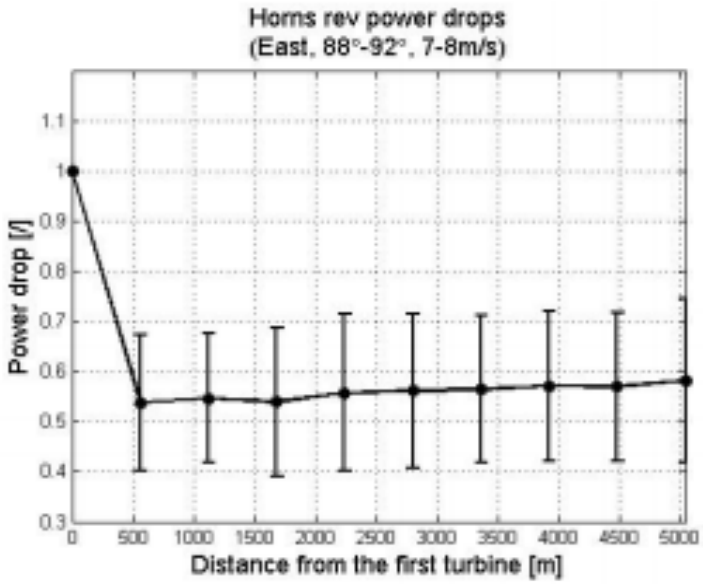

Figure 2.5: Power loss at the Horns Rev offshore wind farm [14].

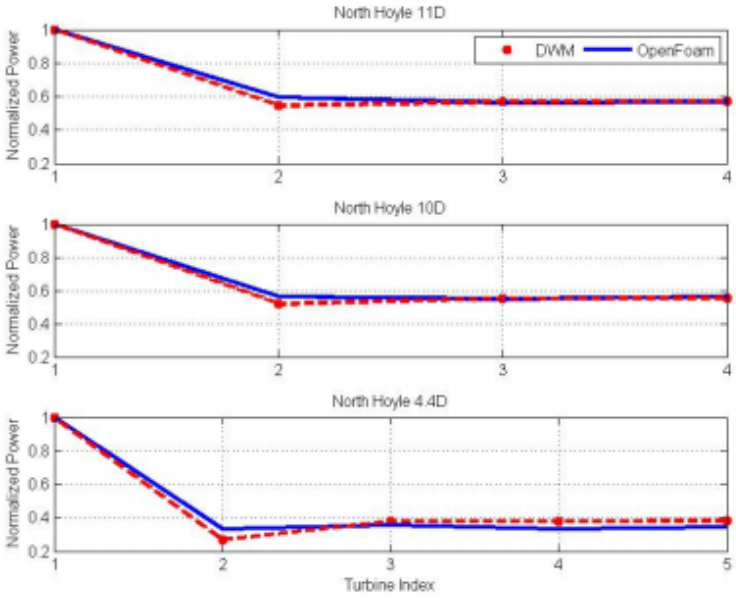

Figure 2.6: Power loss at the North Hoyle wind farm [40].

2.2.3 Wake Models

To account for the power loss that is observed in wind farms, wake models have been created to accurately predict the effects on wind turbine performance. Various models have been produced that range in fidelity and computational intensity.

2.2.3.1 Low-Fidelity Models

Low-fidelity models are characterized by reasonable accuracy and minimal computational time. Among these, the Katic model [45], is one of the most widely used. The wake in this model has a linearly expanding diameter with an initial value equal to that of the rotor. Due to a simplified velocity profile, the Katic wake model is only valid for the far wake (Figure 2.7), which is greater than four rotor diameters in length [25].

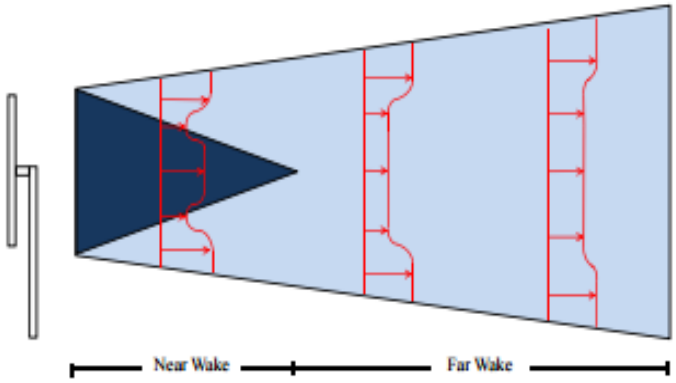

Figure 2.7: Relationship between the wind turbine and the near and far wakes [12].

If the wind turbine is operating in a free-stream velocity U_∞, the relative velocity deficit at a given location downstream can be defined as:

$$1 - \frac{U_\infty}{U_w} = \frac{(1 - \sqrt{1 - C_T})}{\left(1 + 2k\frac{X}{D}\right)^2} \tag{2.7}$$

Where U_∞ and U_w are the free-stream and down-stream velocities, C_T is the thrust coefficient, X is a given position downstream, D is the turbine diameter, and k is the non-

dimensional decay constant that describes how the wake breaks down (wake grows) as it travels downstream [74].

Also noted is the wake width, b (Equation 2.8), which is affected by the non-dimensional decay constant, k.

$$b = D + 2kX \tag{2.8}$$

Per Duckworth and Barthelmie, 2008 [25], k can be estimated to be 0.075 for onshore and 0.04-0.05 for offshore sites.

The Katic model can be computed in seconds, and is used to calculate the power production and velocity deficit of a turbine array. It also assumes that the kinetic energy deficit of interacting wakes is equal to the sum of the energy deficit of the individual wakes [40]. However, the model cannot determine turbulence or structural loads of the turbines and is mostly helpful in determining wake interaction, not realistic wind farm results [12].

In addition to the Katic wake model, there are other low-fidelity models including the WAsP (Wind Atlas Analysis and Application Program) [60], Frandsen [33], and Larsen models [50].

2.2.3.2 Medium-Fidelity Models

Medium-fidelity models are based on the Navier-Stokes equations. These models assume axisymmetric, fully turbulent wakes, zero circumferential velocities, and stationary waked flow fields over time [25]. With these assumptions, the models numerically solve simplified Navier-Stokes equations based on thin boundary-layer

approximation and zero pressure gradients between the waked flow and freestream flow [12].

Ainslie, 1988 [11] proposed a wake model that uses the Navier-Stokes equations and defined the thin shear layer approximation as:

$$U\frac{\partial U}{\partial x} + V\frac{\partial U}{\partial r} = -\left(\frac{1}{r}\right)\frac{\partial(\overline{ru'v'})}{\partial r} \tag{2.9}$$

The right-hand side of Equation 2.9 can be described in terms of turbulent viscosity, ϵ:

$$-\overline{u'v'} = \epsilon\frac{\partial U}{\partial r} \tag{2.10}$$

Where u' and v' are the fluctuating velocity components in the axial and radial directions and $\overline{u'v'}$ is the Reynolds stress [12].

Ainslie models the evolution of the wake using the wake width, b, which is calculated by the conservation of momentum:

$$b = \left[\frac{3.56C_T}{\left(8D_m(1-0.5D_m)\right)}\right]^{\frac{1}{2}} \tag{2.11}$$

Where D_m is the initial relative centerline velocity deficit that is further defined in Ainslie, 1988 [11].

The wake decay rate and the velocity deficit have been derived as Equations 2.12 and 2.13.

$$1 - \frac{U}{U_0} = D_m \exp\left(-3.56\left(\frac{r}{b}\right)^2\right) \tag{2.12}$$

$$\hat{d} = d_0\left[1 + 7.12\left(\frac{\sigma_\theta x}{b}\right)^2\right]^{-\frac{1}{2}} \tag{2.13}$$

Medium-fidelity models may also represent the rotor as an actuator disk [57], which is used to investigate far-wake regions. Other studies have researched free wake models based on vortex segments, that model the vortex structure of the wake and find the inviscid flow field using the Biot-Savart integral [68]. Lastly, the Dynamic Wake Meandering Model [49], which was used in this study, is a medium-fidelity model that is based on the Navier-Stokes equations. It uses the frozen turbulence hypothesis by Taylor and will be further defined in Chapter 3.

2.2.3.3 High-Fidelity Models

Large Eddy Simulations (LES) [58] and Reynolds Averaged Navier-Stokes (RANS) are two high-fidelity models that are currently in use. These techniques can integrate spatially filtered equations of motion that describe three-dimensional turbulence with high levels of detail and few assumptions [58]. Unlike the lower fidelity models that have been described, high-fidelity simulations require extensive calculation time and are mostly interested in the near-wake and initial interactions between the waked and ambient flows.

An example of a high-fidelity model is LES using an actuator line concept [67]. This approach overcomes limitations of the axisymmetric actuator disk model by combining a three dimensional Navier-Stokes solver that allows for distributed body forces along the rotor blades [67]. The dynamics of the wake and tip vortices can be studied to help understand the induced velocities that are present in the rotor plane.

The National Renewable Energy Laboratory (NREL) has also developed a high-fidelity model called SOWFA [22] that incorporates the aeroelastic wind turbine model

FAST [44], the Weather Research and Forecasting Model (WRF) [6], and the OpenFOAM [51] dynamics solver. This model allows for turbine interaction with atmospheric conditions and accurate measurements of turbine performance. Figure 2.8 shows a modeled wind farm obtained through the work of Fleming et al. (2013) [30] using the SOWFA model.

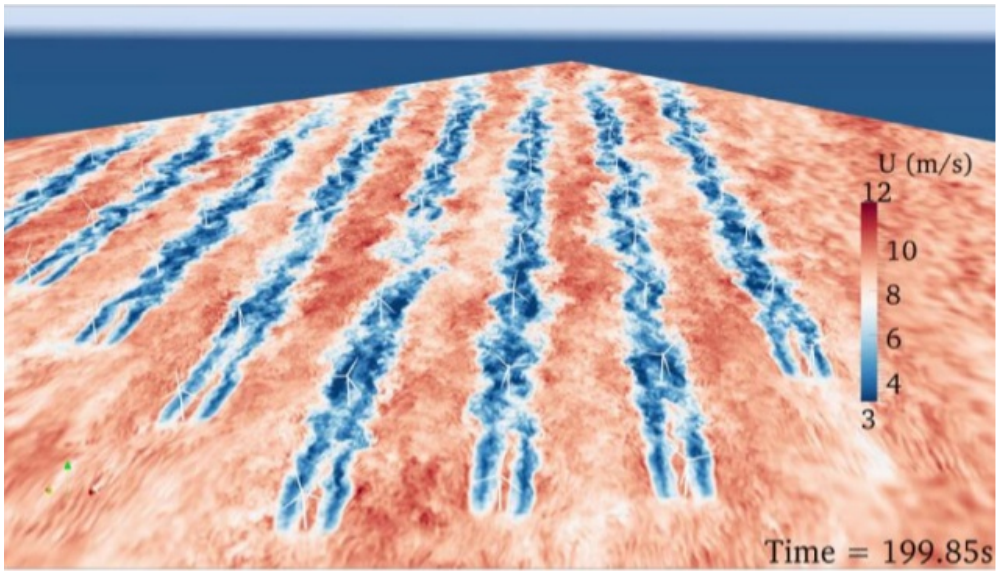

Figure 2.8: Wind farm modeling using the SOWFA model [30].

2.2.3.4 Wake Model Comparison

The previous sections have outlined some of the wake models that have been used and are currently being used in the wind energy field of study. Low-fidelity models cannot account for turbulence structures or near-wake interactions, but allow for reasonable accuracy and low computational costs. Medium-fidelity models are based on the Navier-Stokes equations and are mostly interested in the far-wake calculations. These models produce reasonably accurate results with medium computational effort. High-fidelity simulations are mostly interested in near-wake interactions and require a substantial amount of calculation time, but are the most advanced and accurate models

that have been designed thus far. Figure 2.9 shows the relationship between the fidelity of wake models. Clearly, to reproduce atmospheric effects in the downstream wake most accurately and realistically, the high-fidelity models should be used.

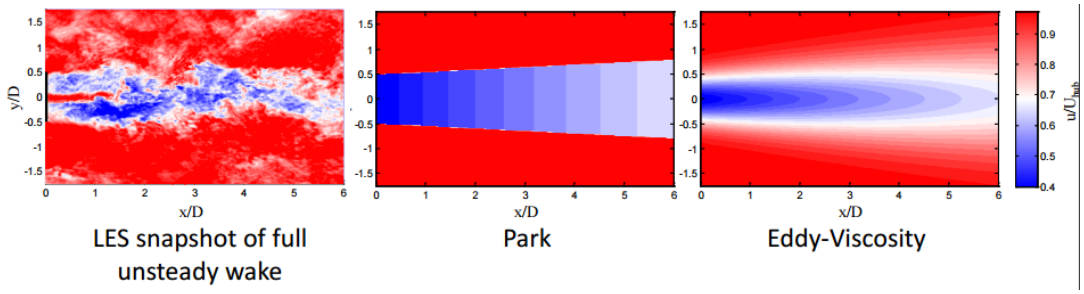

Figure 2.9: Comparison between wake models: left (high-fidelity), middle (low-fidelity), right (medium-fidelity) [23].

2.2.4 Important Meteorology Parameters and Wake Effect Impacts

Wind speed is the primary driver of electrical power production for a wind turbine. However, as mentioned in section 2.1, turbulence and the mixing state of the atmosphere in the surface layer (atmospheric stability) can have important impacts on wake effects and loads on downstream turbines.

2.2.4.1 Turbulence Intensity

The turbulence intensity (TI) level in the incoming flow can have a strong effect on the rate of the wake recovery [79]. With higher levels of turbulence, the wake recovers faster and enhances the output of downwind turbines in large wind farms [65] [73] [20]. Per Manwell et al. 2010 [53], TI is calculated by Equation 2.14 for each wind direction:

$$TI_u = \frac{\sigma}{\bar{u}} \tag{2.14}$$

Where $\bar{u}$ is the magnitude of the average wind velocity and σ is the standard deviation of the wind velocity in the average wind direction.

From the observed data at the Horns Rev wind farm, TI typically decreases between the cut-in and rated wind speeds, but then increases offshore at higher speeds due to mechanical generation and increased surface roughness due to waves [15]. Figure 2.10 shows the Horns Rev observed TI and the data binned in 1 m/s bins around the mean.

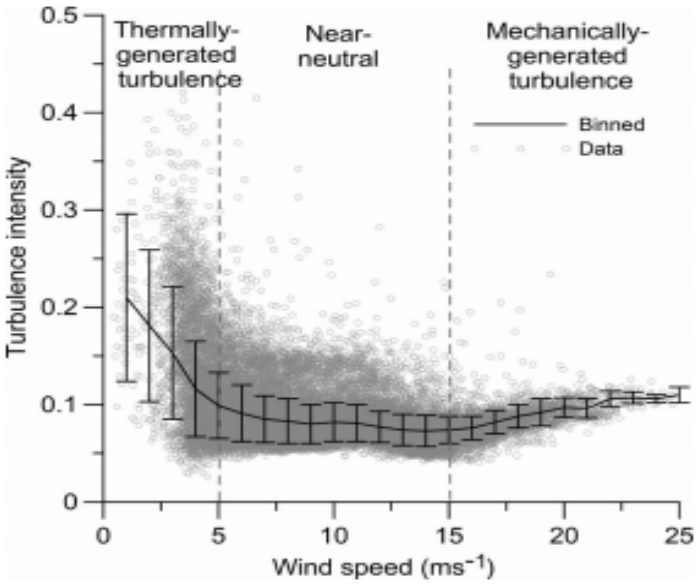

Figure 2.10: TI and wind speed relation at the Horns Rev wind farm. Data has been binned to show the mean value (solid line) [15].

2.2.4.2 Atmospheric Stability

Atmospheric stability is the mixing state of the atmosphere in the surface layer. It is measured using the Monin-Obukhov length (L) and is the height at which buoyancy begins to dominate over TI [70]. This length scale is defined as:

$$L = \frac{-u_*^3}{\left(\kappa\left(\frac{g}{\overline{\theta_v}}\right)\left(\overline{w'\theta'_v}\right)\right)} \tag{2.15}$$

Where g = acceleration due to gravity, $w'\,\theta'_v$ = virtual kinematic heat flux, u_*= friction velocity, θ_v = virtual potential temperature, and the overbar indicates a time average.

Atmospheric stability is commonly grouped into three classifications: stable, unstable, and neutral. However, Hansen et al. 2012 [39] characterizes stability into 7 classes as shown in Table 2.1.

Table 2.1: Atmospheric Stability Classes per the Obukhov Length [39].

Class (cL)	Obukhov length (m)	Atmospheric stability class
−3	−100 ≤ L ≤ −50	Very unstable (vu)
−2	−200 ≤ L ≤ −100	Unstable (u)
−1	−500 ≤ L ≤ −200	Near unstable (nu)
0	| L | > 500	Neutral (n)
1	200 ≤ L ≤ 500	Near stable (ns)
2	50 ≤ L ≤ 200	Stable (s)
3	10 ≤ L ≤ 50	Very stable (vs)

In relation to turbulence intensity, higher levels of TI typically occur in unstable conditions and lower levels in stable conditions. When the atmosphere is more unstable, mixing increases and aids in the recovery of the wake and the wind farm efficiency (total power production is increased). This relationship is not exclusive and low turbulence can still be found at higher wind speeds [16].

2.2.5 Deep Array Effect

In large wind farms the proximity of turbines can also create regions of merging wakes. This phenomenon occurs when two turbines in parallel rows have an interacting wake downstream. Due to the decrease in momentum of the air surrounding the wake, the

recovery is limited and creates an area of continuously decreasing power production in the middle of the wind farm, called the “deep array effect” [40] [15] [33]. Figure 2.11 shows the Horns Rev wind farm and how the wakes not only affect the immediate downwind turbines, but merge with other wakes and impact turbines that are further downstream.

Figure 2.11: Wake merging in the Horns Rev wind farm [4].

2.3 Methodologies for the Micrositing of Wind Farms

Wind farm micrositing has been an important topic of research in wind energy for some time. Many studies have been conducted to locate wind turbines within a wind farm to achieve an optimal result. Lackner et al. (2007) [47] expanded on the Offshore Wind Farm Layout Optimization (OWFLO) project of Elkinton et al. (2006) [26], which sought to minimize the Cost of Energy (COE). Lackner et al. converted this cost of energy into a function solely based on turbine position. The use of the PARK wake model by the OWFLO project and the Jensen model by Lackner et al. enabled these projects to illustrate wake effects and optimize turbine layouts [45] [42]. Chowdhury et al. (2012)

[21] introduced the Unrestricted Wind Farm Layout Optimization (UMFLO) project. This project optimized wind farms based upon layout and appropriate selection of turbines dependent upon their rotor diameters. Chowdhury et al. implemented a standard analytical wake model and successfully used constrained Particle Swarm Optimization (PSO), which is an optimization technique that solves the problem by iteratively trying to improve a solution in regards to a given measure of quality [5]. Additional algorithm-oriented approaches include those of Mosetti et al. (1994) [61], Grady et al. (2005) [38], and Riso Farm Model [17] research studies.

Marden et al. (2012) [54] introduced an optimization approach that used game theory and cooperative control. This demonstrated that Safe Experimentation Dynamics could be used to maximize energy output without directly modeling the aerodynamic interactions among turbines. An integer coded evolutionary algorithm (one based on restricting variables to be integers) was implemented by Gonzalez et al. (2010) [37]. This algorithm-based design uses the net present value to minimize the wind farm initial investment and has the capability of dealing with wake decay and areas of non-uniform load-bearing capacity soil.

Additionally, numerous programs have been developed to assess the placement of wind turbines based upon the wind resource. The most popular of these is the WAsP program [60], which uses the wind climate observation at a nearby meteorological station. This program estimates the wind resource over the terrain under study by microscale flow analysis and incorporates roughness change, sheltering obstacles, wind turbine wakes, and atmospheric stability models within it. Another similar software is Meteodyn [24], which optimizes wind farms based on the wind resource using

computational fluid dynamics (CFD). These computations allow a more accurate result in complex terrains. Meteodyn also considers the Katic model [45] for wake effects when simulating the energy produced by the wind farm. WindSim [75] also assesses wind farm optimization by means of the local wind resource. This program, like Meteodyn, uses CFD modeling to combine advanced numerical processing with a 3D Reynolds-averaged Navier-Stokes solver. By using CFD, WindSim can better capture terrain effects and wind conditions, so that the wind farm is in the best location in terms of the wind resource. Additional wind resource software includes WindPRO [72] and Fluidyn [31].

2.3.1 Objective Functions

In wind farm micrositing and optimization, an objective function is chosen, which allows the optimizer to minimize or maximize some factor. Several different objective functions have been used in wind farm micrositing. Mosetti et al. (1994) [61] created an objective function to produce the highest amount of energy at minimum cost:

$$Objective = \frac{1}{P_{tot}} w_1 + \frac{cost_{tot}}{P_{tot}} w_2 \tag{2.16}$$

Where P_{tot} is the total energy produced in one year, w_1 and w_2 are arbitrarily chosen weights, N_t is the number of turbines installed, and $cost_{tot}$ is the cost/year of the entire wind farm, which is defined as:

$$cost_{tot} = N_t \left(\frac{2}{3} + \frac{1}{3} e^{-0.00174 N_t^2} \right) \tag{2.17}$$

Lackner et al. (2007) [47] took a different approach and minimized the levelized production cost (LPC). Where the LPC is defined as:

$$LPC = \frac{I_{tot}}{a_f P_{tot}} + \frac{C_{O\&M}}{P_{tot}} \tag{2.18}$$

Where I_{tot} is the initial investment of the entire wind farm, a_f is the annuity factor, and $C_{O\&M}$ is the costs of operation and maintenance.

A genetic algorithm approach by Grady et al. (2005) [38] sought to maximize the production capacity while limiting the number of turbines and acreage of land, where the optimization is based upon the objective function:

$$Objective = \frac{cost_{tot}}{P_{tot}} \tag{2.19}$$

Where P_{tot} and $cost_{tot}$ are the same as described in Equation 2.16.

Messec et al. (2012) [55] introduced a study in which the uncertainty of the wind behavior was researched using three different case studies (same rotor diameters, differing rotor diameters, and same rotor diameters, but with adaptation to wind conditions). This methodology determined the optimum wind farm layout and number of turbines that would maximize the net power production. He modeled this behavior by proposing and minimizing the following objective function:

$$Objective = \frac{\sigma_{COE}}{COE} \tag{2.20}$$

In which COE is defined as:

$$COE = \frac{Cost_{farm}}{P_{tot}} \tag{2.21}$$

σ_{COE} is the standard deviation of the COE, $Cost_{farm}$ is the annual cost of the wind farm in dollars per kW, and P_{tot} is the same as Equation 2.16.

In general, most micrositing optimization studies have focused on annual energy production (AEP) or COE [46].

2.3.2 Modeling of the Wind Resource

For micrositing purposes, the behavior of the wind is typically modeled using statistical averages of wind speed and wind direction. These approaches attempt to capture the expected long-term representative characteristics of the wind resource at a specific site. This statistical data can then be used in optimization programs to locate the turbines and optimize energy production. For instance, if a site has a strong prevailing wind direction averaged over a long period, it would generally be logical to increase the spacing or turbine rows in the prevailing wind direction, and decrease the inter-turbine spacing within a row. Likewise, it would be logical to have a wind farm with fewer rows but more turbines per row. Both choices are likely to result in increased energy production. Figure 2.12 shows an LES simulation performed by Meyers et al. (2012) [56]. This wind farm layout has fewer rows, but more turbines per row, to maximize captured kinetic energy.

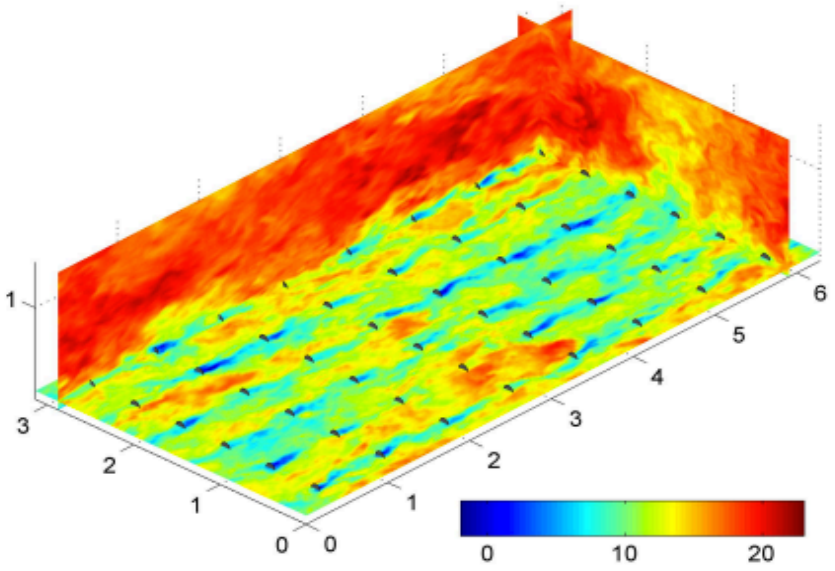

Figure 2.12: LES simulation with a wind farm layout that has fewer rows, but more turbines per row [56].

Clearly, there are constraints that must be considered such as the allowable extent of the wind farm, water depth changes, excluded areas, etc., but nonetheless the statistical representation of the wind resource is critical in determining the optimal wind farm layout.

To characterize the wind resource statistically, numerous studies have described the joint probability of both wind speed and wind direction using a "wind rose" [34] [76]. The most common wind rose used is separated into thirty-six direction sectors [28]. However, other studies have separated the wind rose into twenty-four, sixteen, and eight [36]. Ozturk (2004) [64] even used a unidirectional wind to define his model. Figure 2.13 shows wind roses with differing sector numbers that studies have used to analyze the wind resource.

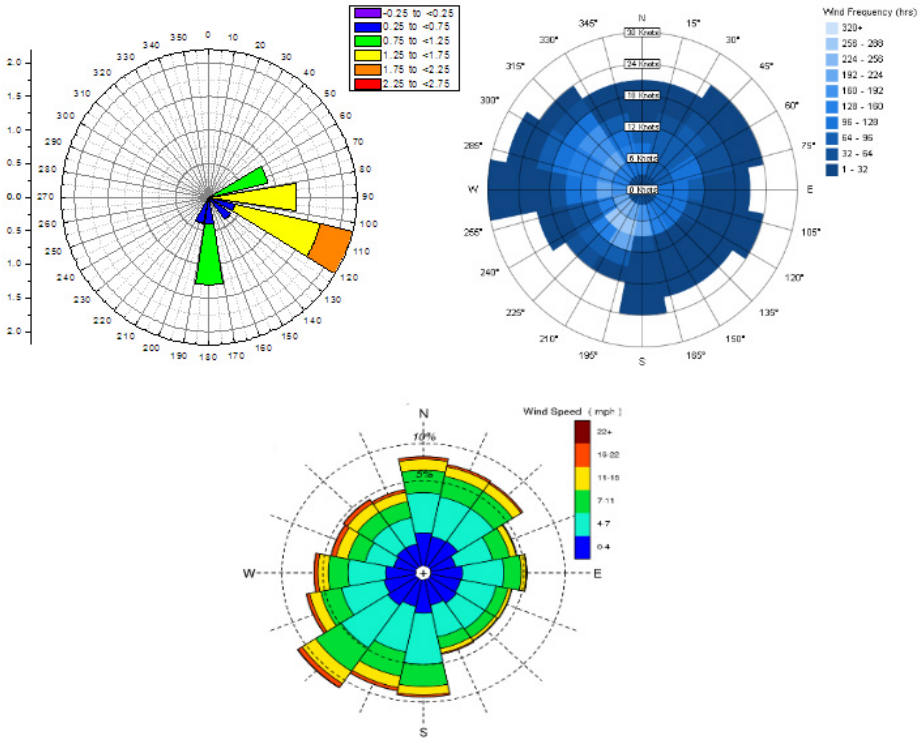

Figure 2.13: Wind rose with differing sector numbers [8] [9] [10].

Another approach in estimating the behavior of the wind is the use of the wind speed probability density function. This method is often modeled with the Weibull distribution [78], which uses the scale parameter, c and the shape parameter, k (Equations 2.22 and 2.23). The scale parameter shows on average how windy it is at a location over a given time-period, and the shape parameter affects the shape of the distribution. When $1 \leq k < 10$, a good approximation for k and c are:

$$k = \left(\frac{\sigma_U}{\overline{U}}\right)^{-1.086} \tag{2.22}$$

Where σ_U is the standard deviation of the wind speed and $\overline{U}$ is the mean wind speed.

$$c = \frac{\overline{U}}{\Gamma\left(1 + \frac{1}{k}\right)} \tag{2.23}$$

Where Γ is:

$$\Gamma(\mathrm{x}) = \int_0^\infty e^{-t} t^{x-1} dt \tag{2.24}$$

Manwell et al. (2010) [53] defines the Weibull Distribution as:

$$p(U) = \left(\frac{k}{c}\right)\left(\frac{U}{c}\right)^{k-1} exp\left[-\left(\frac{U}{c}\right)^{k}\right] \tag{2.25}$$

where c and k are the scale and shape parameters respectfully and U is the wind speed.

Figure 2.14 shows a Weibull distribution with different shape factors for a mean wind speed of 6 m/s. It can be noted that as the shape factor increases, the probability of wind speeds clustered around the average value increases.

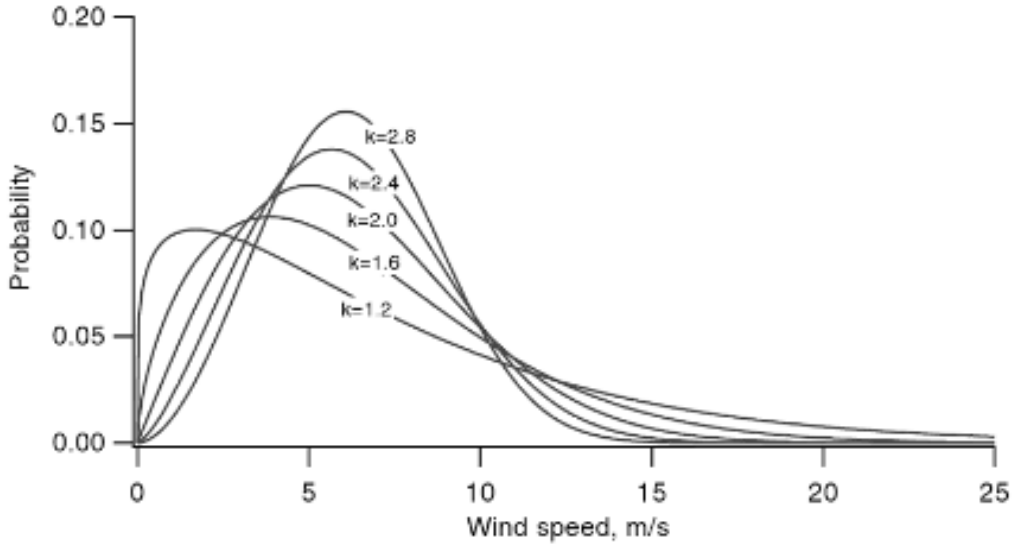

Figure 2.14: Weibull distribution for a wind speed of 6 m/s [53].

CHAPTER 3

METHODOLOGY

Unlike previous approaches to micrositing, which have used statistical averages of the wind resource, this study focused on the micrositing of wind turbines based on concurrent time-series of wind and electrical price data. The underlying justification for this approach was the potential for temporal correlation between the wind resource (both speed and direction) and electricity prices. These variables are driven by the demand for electricity and largely affected by diurnal weather patterns and the changing of seasons. For example, in New England, summer days have high temperatures that lead to substantial air conditioning loads. This in turn causes overall electricity demand and price to be high, which puts pressure on the electrical grid and increases revenue for the electrical suppliers. Similarly, the wind resource has distinct diurnal and seasonal patterns. New England winters tend to have the highest mean wind speed, and with proximity to the coast, diurnal sea breezes as well. Clearly, both the electricity price and the wind resource also have stochastic variations in their signals, and given the prevalence of these patterns, it was interesting to consider if they could be utilized to inform the micrositing process. If during the high demand summer afternoons, the prevailing wind direction were to differ significantly from the annual average prevailing wind direction, it may be beneficial to exploit this information by positioning the turbines in a wind farm to be more productive at high demand times of the year. This methodology assumed that the wind farm revenue depends on the instantaneous price of electricity, rather than receiving a constant price per unit of energy produced. It also

contrasts with standard approaches that attempt to maximize production based on statistical averages over long periods of time. By taking averages over extensive periods (years), diurnal and seasonal effects are disregarded.

The overall approach used to investigate this issue is summarized as follows:

1. Concurrent time series data of electrical price, wind speed, and wind direction was collected for an offshore site in New England (Sections 3.4 and 3.5). Each are hourly time-series that have been recorded over a 5-year period.
2. Candidate wind farm layouts were created that have representative spacing between turbines, as described in Section 3.3
3. Using the Dynamic Wake Meandering Model (Section 3.2), the total expected power produced by the candidate wind farms was calculated for a range of wind speeds and wind directions, and stored in a table.
4. Using simple interpolation of the tables created in Step 3, the time-series of wind speed and direction were used to produce a time-series of power output for every hour for a candidate wind farm. By multiplying the power output by the concurrent electricity price, a time-series of revenue was calculated as well.
5. Next, while the spacing between turbines for a given candidate wind farm remains unchanged, its entire orientation may be rotated to evaluate a different candidate wind farm. This is accomplished by simply shifting the wind direction time-series by the rotation angle to simulate rotation of the wind farm. Steps 4 and 5 were then repeated.

6. Each candidate wind farm was then evaluated for the total production and revenue.

Note that this approach did not attempt to optimize the location of individual wind turbines. Instead, it used representative wind farm layouts (characterized by the regular spacing between turbines), and then rotated the wind farm to assess the influence of wind direction on output and revenue.

To better understand the process a flow chart has been created to illustrate the 6-step procedure (Figure 3.1). Step 1 consists of identifying the location and concurrent time-series of electrical, wind speed, and wind direction data. Step 2 determines the candidate wind farm layouts and parameters that were used in the study (wind speeds, wind directions, and turbulence intensities). In Step 3 the input files for the DWM are modified, DWM is run, and power tables are created that show the average power and total power per wind direction and speed for the wind farm. This step is repeated for each layout. Step 4 evaluates the time-varying wind and electrical power and price data and produces the time-series of the hourly power output and revenue. Step 5 orients the farms by shifting the wind directions to evaluate new candidate layouts. Steps 4 and 5 should be repeated for each orientation and each layout. Step 6 evaluates the wind farm orientations and determines the total AEP and revenue for each farm. Conclusions can then be drawn about the significance of orienting wind farms to maximize total revenue.

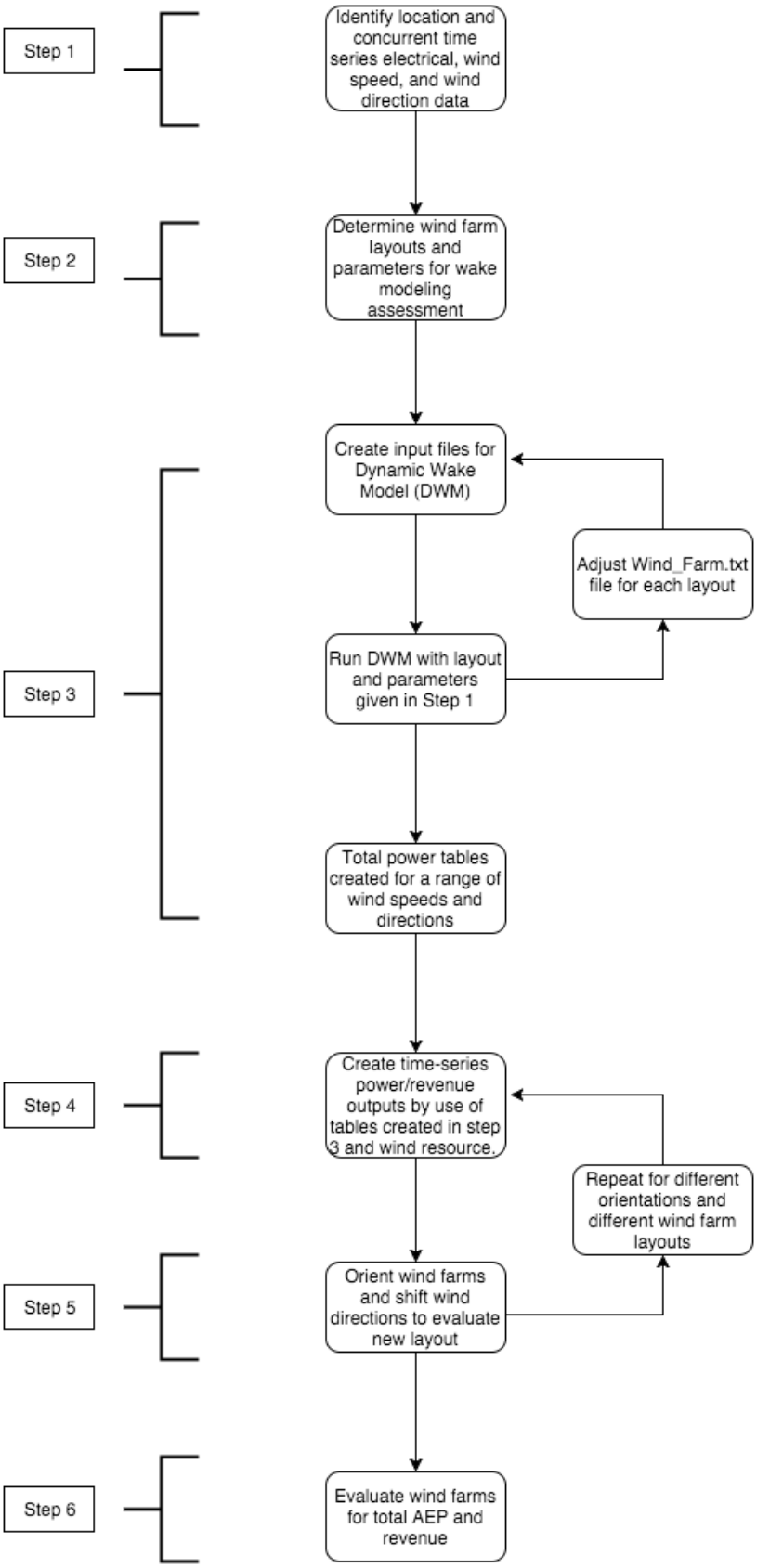

Figure 3.1: Flow chart of the micrositing process.

3.1 Objective Function

The objective function of this study was based on maximizing revenue, which in turn, will create a more profitable wind farm. Specifically, the objective function was defined as the summation of the price multiplied by the power at each hour (t) through the 5-year period or 34,744 hours (T).

$$Decision\ Variable = P_f \tag{3.1}$$

Where P_f if the placement of wind farm f.

$$Objective = \max \sum_{t=1}^{T} price_t \ x \ power_t \tag{3.2}$$

Where $price_t$ is the electrical price at hour t and $power_t$ is defined as:

$$power_t = \sum_{i=1}^{N} W_i \tag{3.3}$$

Where W_i is the average power output for turbine i and N is the total number of turbines in the wind farm (36).

By taking the power time-series and relating it to the electrical price, a time-series of revenue was created. This revenue time-series allowed for an in-depth evaluation of the summation of total revenue for each wind farm over the 5-year period.

Section 3.2 defines the candidate wind farms that were modeled in the Dynamic Wake Meandering Model and evaluated with the use of the objective function. Section 3.3 presents the simulation tools that were used to model the wake effects and provide the power outputs for the power tables ($power_t$). Section 3.4 shows the metocean data set that contains the wind characteristics at the location and the raw data that were used in correlation with the power tables to provide a power time-series. Section 3.5 provides the

ISO New England power data ($price_t$). This data was multiplied by the power time-series obtained from Section 3.4 to create a revenue time-series.

3.2 Wind Farm Layouts

To inform the micrositing process and compare wind farms based on time-varying data with conventional approaches, six example layouts were created for simulation with the DWM software. The examples are not exhaustive of all possible wind farm layouts, but they highlight the important aspects and trends of this study. The properties of the examples are as follows:

- Six different wind farm layouts: 6X6 square with 6D spacing, 9X4 rectangle with 6D spacing, 9X4 rectangle with 4D and 8D spacing, 6X6 square with 8D spacing, 9X4 rectangle with 8D spacing, and a 9X4 rectangle with 6D and 10D spacing (Figures 3.2, 3.3, 3.4, 3.5, 3.6, and 3.7).
- 36 NREL 5MW turbines in each layout.
- Hub-height of 90m with a 63m-rotor radius.
- Meteorological parameters used in the simulations consist of a range of wind speed, wind directions, and turbulence intensities (Table 3.1). The wind direction was only simulated from 0 to 90 degrees because of symmetry, and so the output for any wind direction was calculated using the results from the given directions.
- The orientation of the wind farms can be rotated as well. Rotation angles from 0 to 180 degrees in 1 degree increments were used (Figure 3.8).

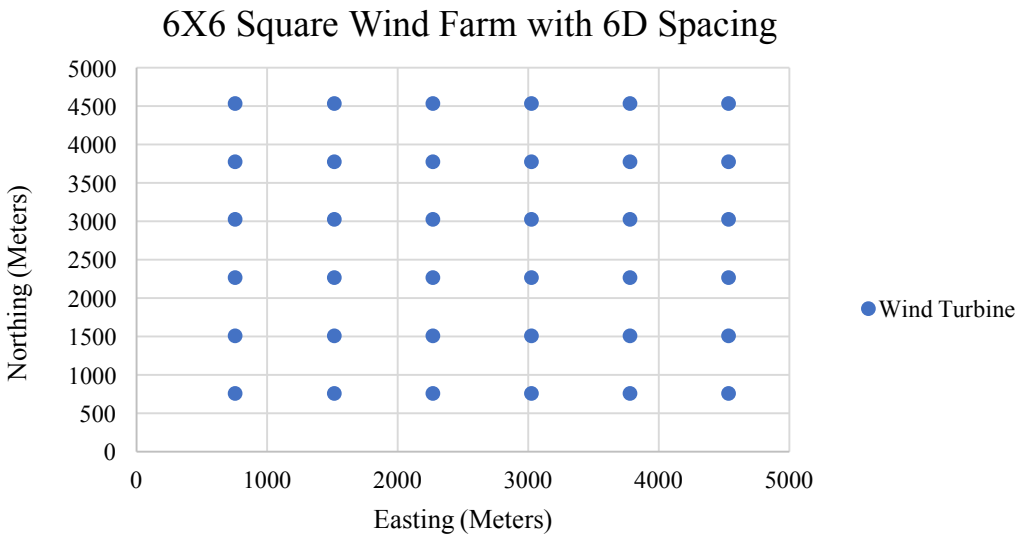

Figure 3.2: 6X6 square wind farm with 6D spacing.

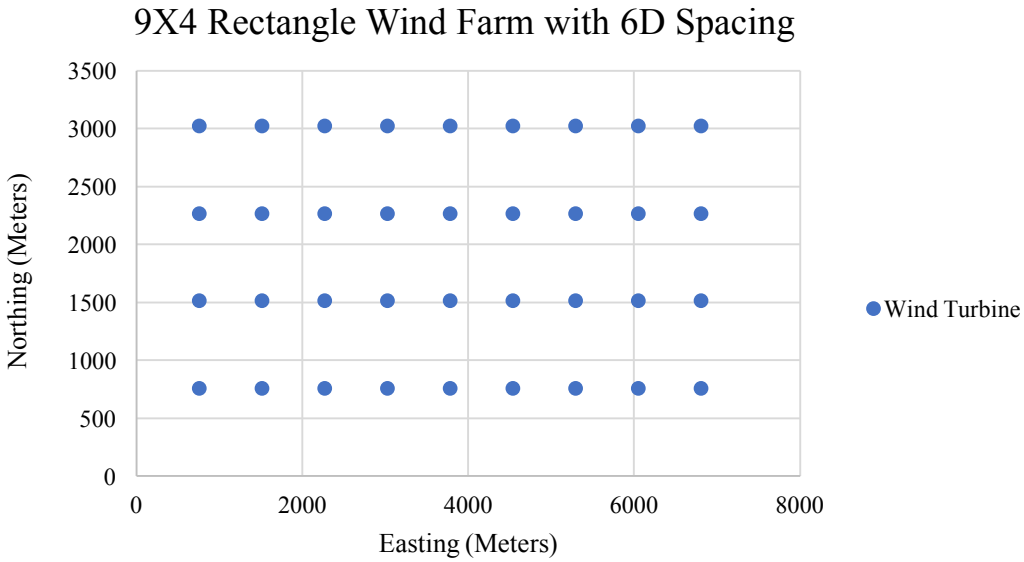

Figure 3.3: 9X4 rectangular wind farm with 6D spacing.

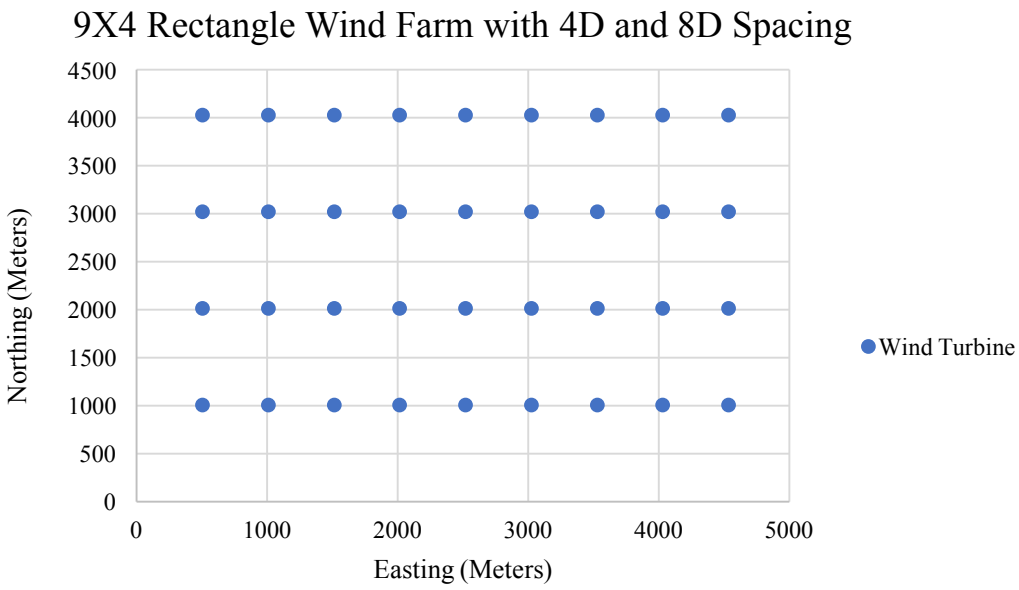

Figure 3.4: 9X4 rectangular with farm with 4D and 8D spacing.

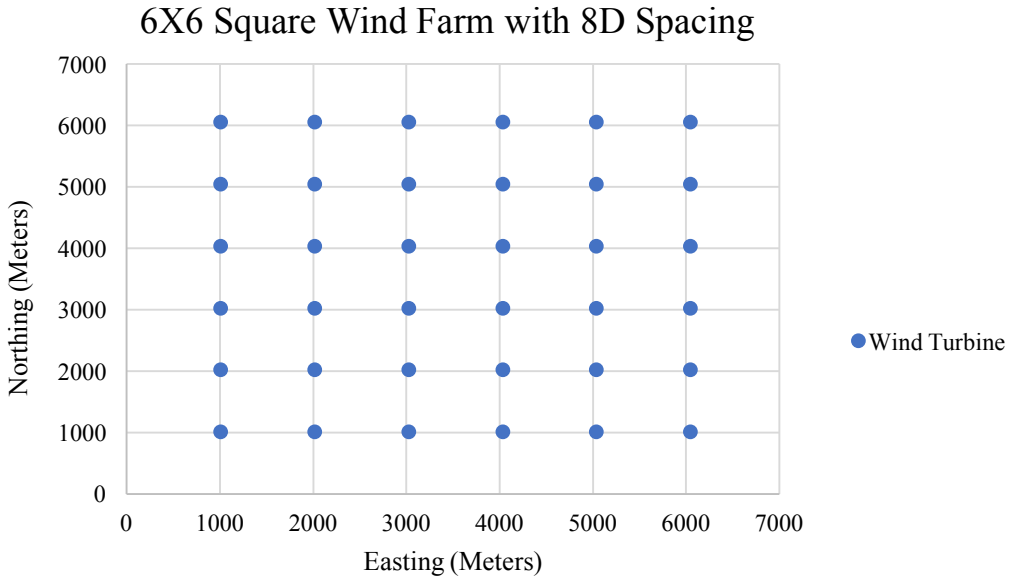

Figure 3.5: 6X6 Square wind farm with 8D spacing.

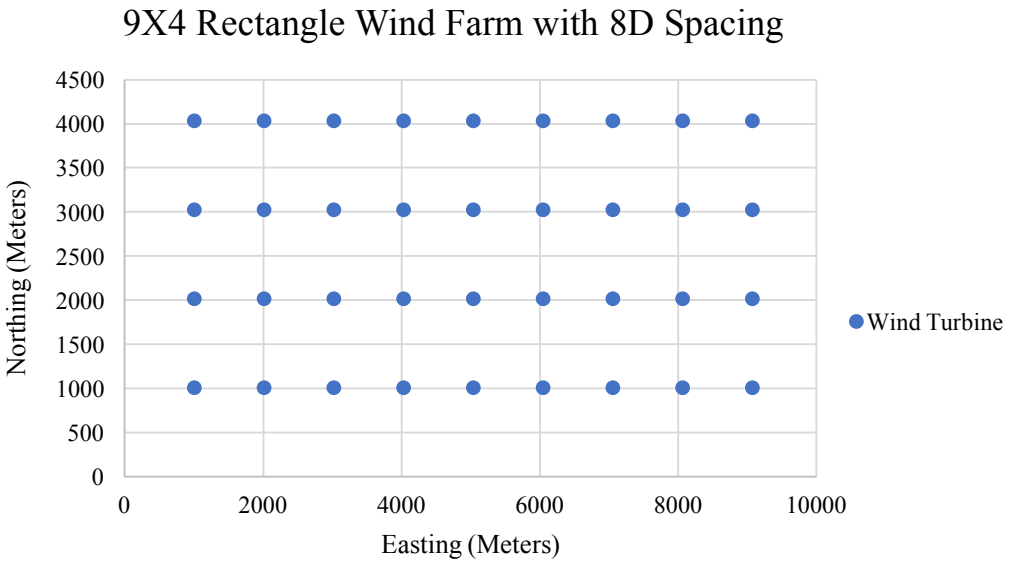

Figure 3.6: 9X4 rectangular wind farm with 8D spacing.

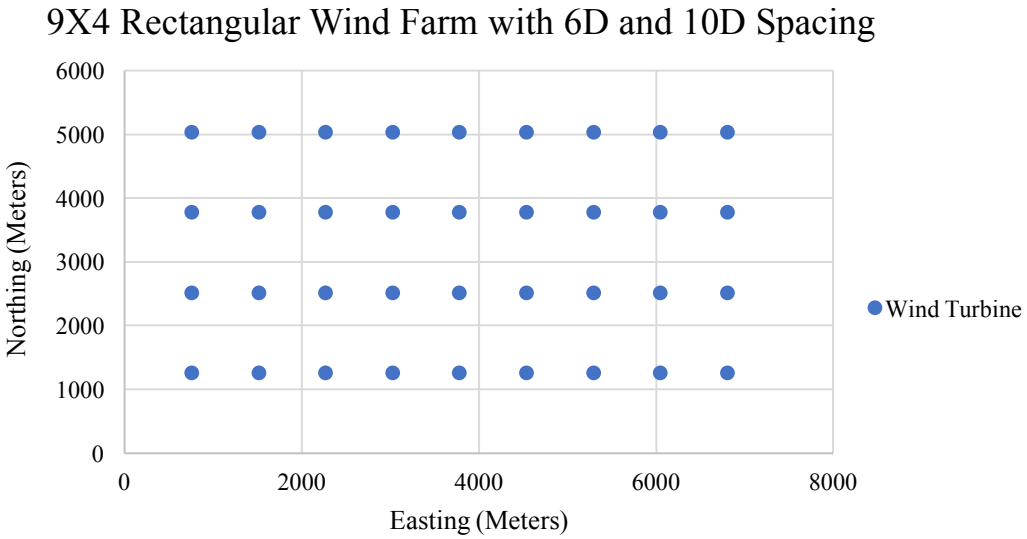

Figure 3.7: 9X4 rectangular wind farm with 6D and 10D spacing.

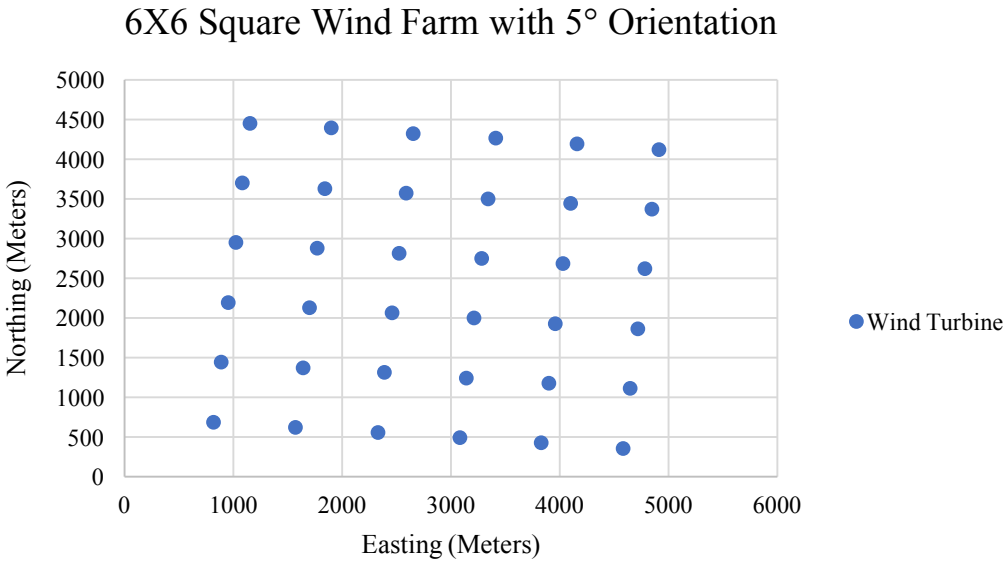

Figure 3.8: 6X6 square wind farm with 5° orientation.

Table 3.1: Wind Speed, Wind Direction, and Turbulence Intensity Parameters.

Wind Direction (Degrees)	Wind Speeds (m/s)	Turbulence Intensities (%)
0	4	14
10	6	13
20	8	12
30	10	11
40	12	10
50	14	9
60	16	8
70	18	7
80	20	6
90	22	6
~	24	5

Note that for each wind farm, the 11 mean wind speed values with corresponding TI values, were simulated for each of the 10 wind directions, resulting in 110 simulations for an individual wind farm. Different wind farm orientations do not need to be simulated separately. Instead, the time series of wind direction data can be shifted uniformly by the orientation angle to mimic the rotation of the wind farm orientation.

In this study the turbulence intensity was estimated based on the work by Hao et al. (2016) [40] and the study by Wang et al. (2014) [77], which shows the relationship between the Normal turbulence model (NTM), real observations, and the ONT90 (Figure 3.9). Due to this estimation, the turbulence intensities used for this project may be lower than actual measurements in a real wind farm.

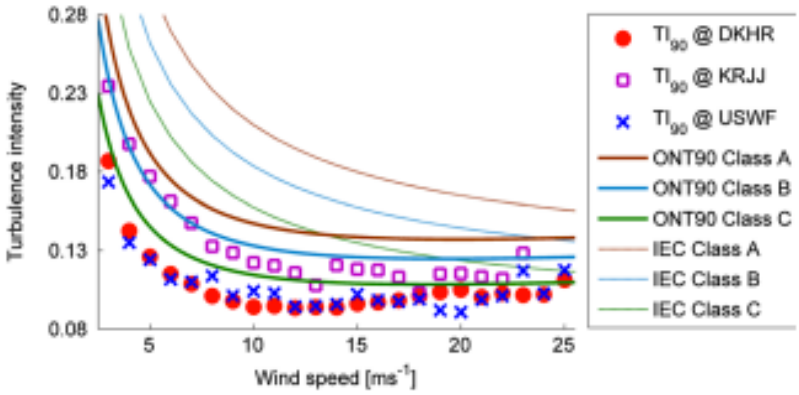

Figure 3.9: Relationship between turbulence intensity and wind speed for real observations, NTM, and ONT90 [77].

3.3 Simulation Tools

During this research, a wind farm simulation tool developed by Hao et al. (2016) [40], also known as the Dynamic Wake Meandering Model (DWM), was used to calculate the power production of the wind turbines within a given wind farm layout. This program utilizes several software tools developed by the National Renewable Energy Laboratory (NREL), including TurbSim, AeroDyn, and FAST. These models allow for the aero-elastic simulation of each turbine within the wind farm, subjected to both stochastic turbulence (generated by TurbSim) and the increased turbulence and reduced wind speed from upstream wakes (modeled using the DWM). The turbines are each simulated sequentially, from upstream to downstream, so that wake effects

propagate through the wind farm (Figure 3.10). The energy production of each turbine and the wind farm can then be calculated from the simulation outputs.

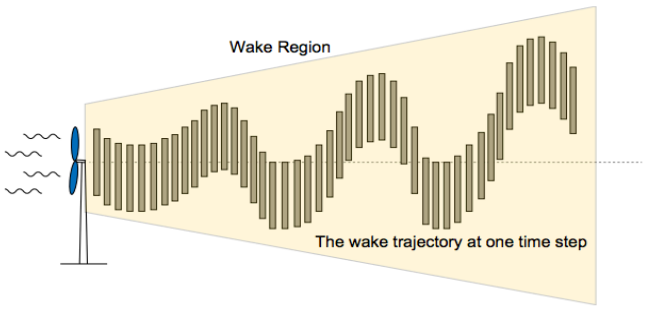

Figure 3.10: Wake meandering simulation modeled by the DWM [40].

3.3.1 TurbSim

TurbSim is a software tool that is used to generate a full-field stochastic wind file with a given mean wind speed and turbulence intensity. It efficiently simulates the time series of three-component wind-speed vectors at points in a two-dimensional vertical rectangular grid that is fixed in space [43]. TurbSim uses a spectrum of velocity components and spatial coherence in the frequency domain. The output of TurbSim is used in the input files for FAST [44].

3.3.2 FAST and AeroDyn

FAST (Fatigue, Aerodynamics, Structures, and Turbulence) is NREL's primary code for simulating the coupled dynamic response of horizontal-axis wind turbines. This model enables coupled nonlinear aero-hydro-servo-elastic simulation in the time domain [44]. It is based on advanced engineering models that are derived from fundamental laws and is Fortran based. FAST uses the AeroDyn module to calculate the aerodynamic performance of a wind turbine. This model uses blade-element momentum (BEM) theory

to calculate blade loads and aerodynamic performance under the influence of the wind field.

3.3.3 DWM

The Dynamic Wake Meandering Model (DWM) is used to model turbine wakes. The downstream velocity deficit is calculated in time and space, which can then be used to estimate the performance of downwind waked turbines. This model is based on the work by Larsen et al. (2008) [48] and consists of two sub-models that estimate the quasi-steady wake deficit and the downstream wake meandering process [40]. The DWM uses the mean field turbulence intensity and the turbulence structure to calculate the downstream velocity deficit. It also can capture time-dependent physics present in turbine wakes and can predict turbine loads and power production at the same time. Figure 3.11 shows a flow chart of the DWM and the three essential processes that provide the output.

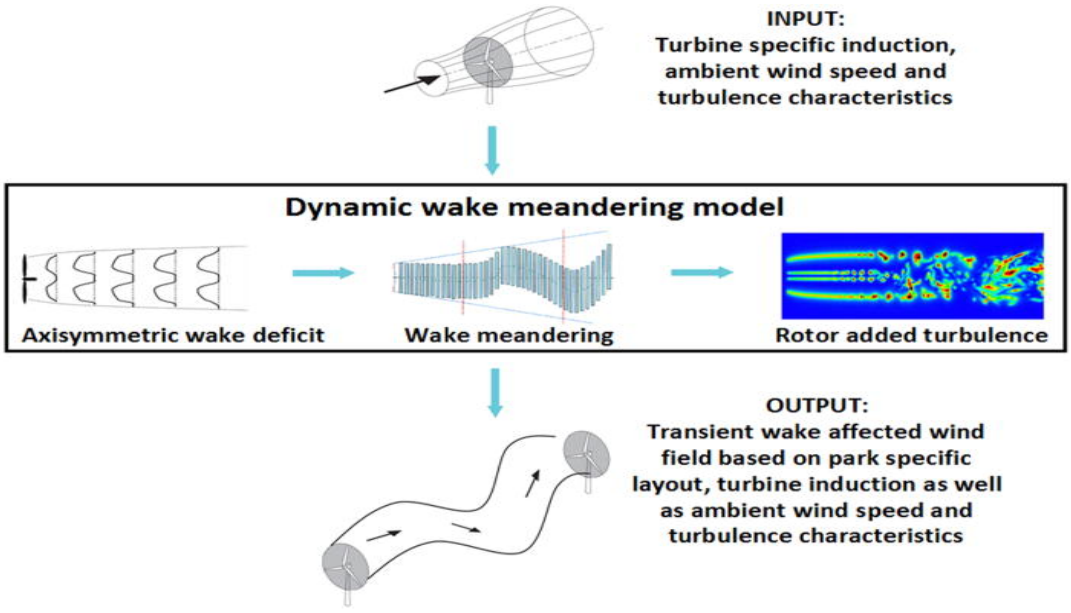

Figure 3.11: Flow chart of the DWM [40].

3.3.3.1 Quasi-Steady Wake Deficit and Wake Meandering

The first process in the DWM is the quasi-steady wake deficit calculation. Using the two-dimensional eddy viscosity model, the wake deficit is calculated in the meandering frame of reference [48]. This process includes the wake expansion as a function of downstream transportation time, which is caused by turbulent diffusion and the rotor pressure field. Wake meandering describes the stochastic transport of the wakes laterally and vertically at a given downstream location, which stems from the large-scale turbulence structures in the atmospheric boundary layer.

3.3.3.2 Turbulence Effects

Upon calculation of the wake deficit and meandering, the DWM considers the turbulence effects caused by an upstream turbine. The model concerns small-scale turbulence and time-dependent physics that are present in the wakes. The added wake turbulence includes wake shear turbulence and blade bound vorticity, which consists mainly of tip and root vortices [48]. This turbulence exhibits non-stationary (develops with downstream transportation time) and inhomogeneous (varying across wake) properties, which are not characterized by conventional atmospheric turbulence. The DWM models the inhomogeneous turbulence based on a homogeneous Mann turbulence field [52].

3.3.3.3 DWM Output

Once the asymmetric wake deficit, wake meandering, and turbulence effects have been considered, the DWM outputs a 3-D transient wake-affected wind field behind the

upstream turbines under consideration. A time-series of the meandering wake position behind each upstream turbine and the added turbulence intensity and wake meandering on downwind turbines due to the wake formations is detailed. This also includes a FAST output file where a time-series of generator power is given.

3.4 Metocean Data Set for Offshore Wind

Meteorological and ocean conditions are used in the siting and analysis of offshore wind farms. The metocean database was created to aid in this process, providing data for 23 ocean sites around the United States. The data collected during the project was obtained from the National Data Buoy Center and includes the variables of interest for offshore wind energy design such as wind and wave conditions [70].

This case study focused on the SE Nantucket buoy location (buoy 44008), as seen in Figure 3.9. With over 5 years of data available (Figure 3.12), there was an adequate amount of information to enable the time-series based analysis for the micrositing of a wind farm at this location. The two most important parameters that were used are the wind speed and direction, which are averaged over an 8-minute period and reported hourly [69]. To ensure accurate wind speed at a typical offshore wind turbine (OWT) hub height (90 m), post-processing of the data was calculated during the metocean study using the log and power laws (Equations 3.5 and 3.6).

$$U(z) = U(z_r)\frac{\ln(z) - \ln(z_0)}{\ln(z_r) - \ln(z_0)} \tag{3.5}$$

$$U(z) = U(z_r)(\frac{z}{z_r})^{\alpha} \tag{3.6}$$

Where U(z) is the wind speed at height z, $U(z_r)$ is the reference wind speed at height z_r, z_0 is the surface roughness and α is the power law exponent.

Figure 3.12: Metocean database buoy locations [70].

Figure 3.13 shows the wind speed and direction measurements from the Nantucket buoy from March 2007-December 2012, scaled to a 90-m hub height. The gaps indicate times when the buoy was having technical difficulties or had to be shut off for an unknown reason.

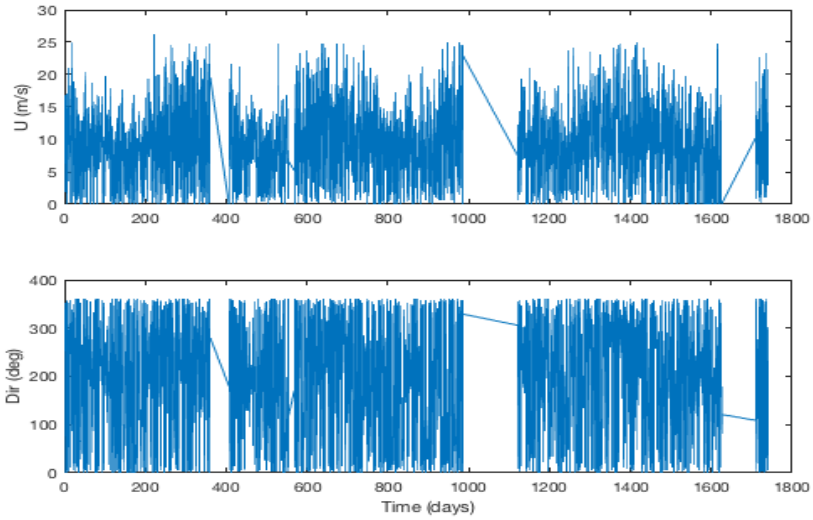

Figure 3.13: Metocean wind data from the Nantucket buoy location over 5-years.

Figure 3.14 is a histogram of the 90-m hub height wind speed data at the Nantucket buoy location. The data has been normalized based on 5-year observations and indicates that the most frequent wind speeds occur between 7 and 10 m/s, with a mean wind speed of 9.12m/s. The data has also been fitted with a Weibull curve where the shape factor k has a value of 1.78.

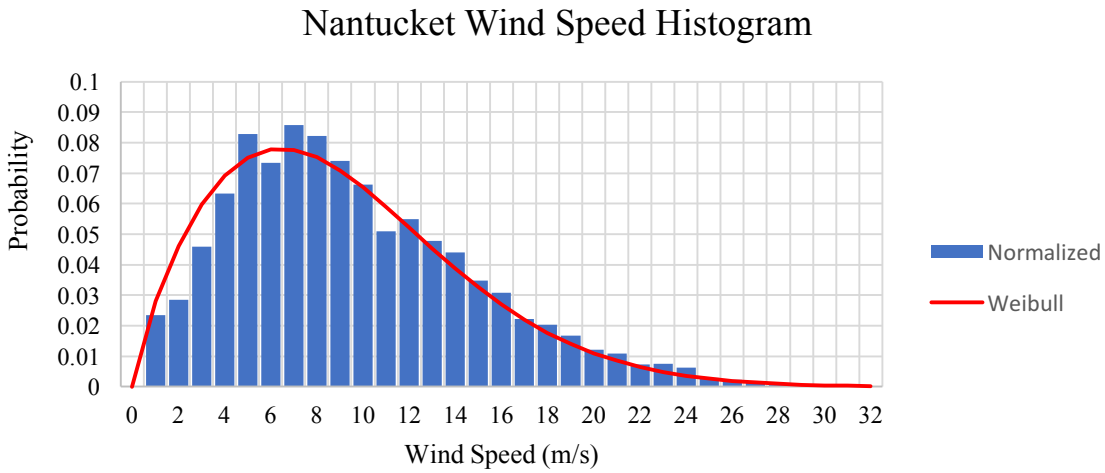

Figure 3.14: Histogram of the normalized 90m hub height wind speed at the Nantucket buoy location.

The wind rose for the Nantucket location over the 5-year period is shown in Figure 3.15. The winds come from the southwest 16.6% of the time during the year and least frequently from the east and southeast at around 8%.

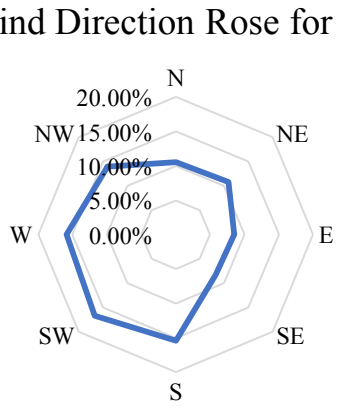

Figure 3.15: 5-year wind rose for the Nantucket location.

3.5 ISO New England Power Data

Power consumption and demand in New England is divided into three regions: NEMASSBOST, WCMASS, and SEMASS (Figure 3.16). Each area has data for the 5 years, provided by ISO New England [29], which parallels the time-series data obtained from the metocean data set study [70].

Figure 3.16: ISO New England wholesale power regions in Massachusetts [29].

The hourly time-series electrical price and demand data for SE Massachusetts are shown in Figure 3.17. This wholesale region is chosen because this case study was interested in the SE Nantucket location. The demand and price fluctuations are dependent on the seasons, where high electrical demand and price are correlated with the warm summers and cold winters. The time-series graphs for the other two regions in Massachusetts are in Appendix A.

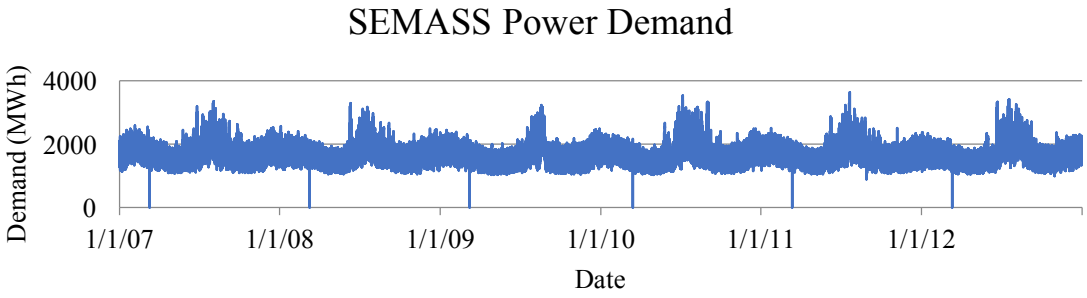

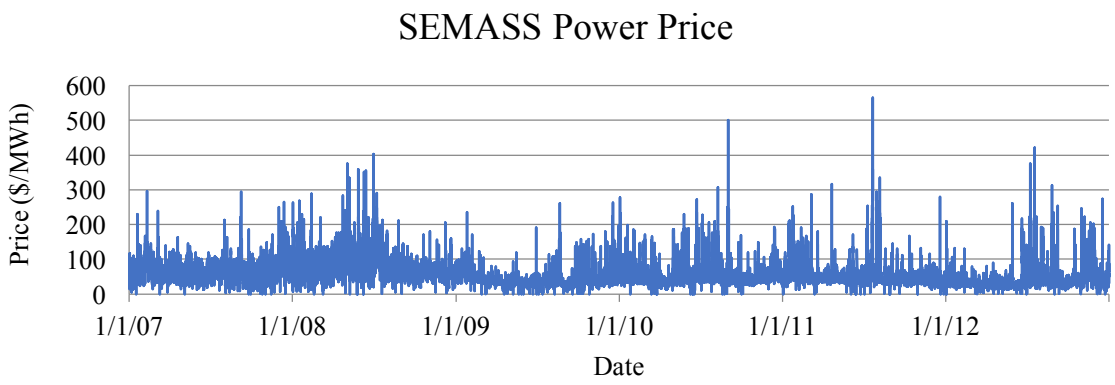

Figure 3.17: 5-year time-series price and power data from Southeastern Massachusetts, including Nantucket.

Figure 3.18 shows a histogram of the normalized electrical price data from March 2007-December 2012. Prices between 40 and 80 $/MWh were the most frequent, although, prices exceeded 100 $/MWh, including a price of 561 $/MWh. Appendix A shows the histograms of the electrical price data for the WCMASS and NEMASSBOST areas.

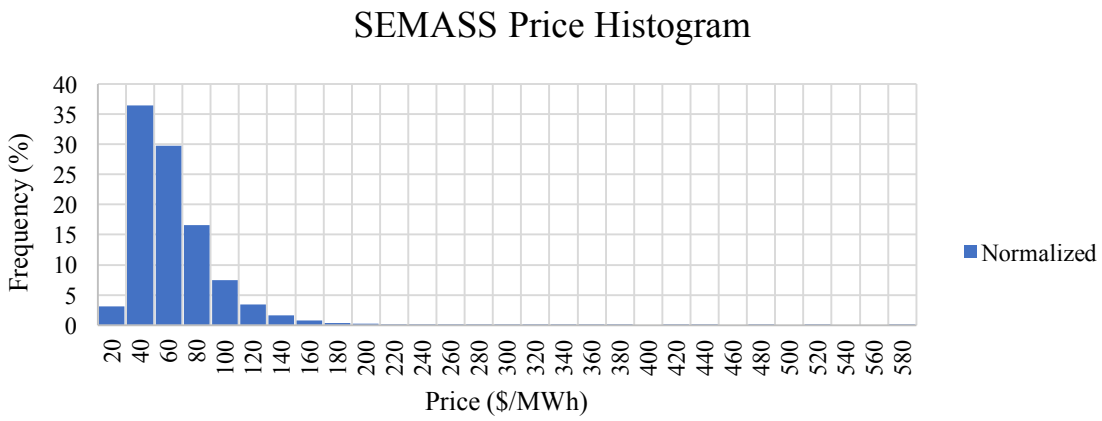

Figure 3.18: Histogram of the electrical price data for the Southeastern Massachusetts area.

The histogram for the power demand in the SEMASS area is shown in Figure 3.19. Over the 5-year period, the hourly average is around 1,733 MWh, but values can be as low as 150 MWh and as high as 3,750 MWh, which are most likely attributed to

seasonal conditions. Appendix A shows the demand histograms for the WCMASS and SEMASS areas.

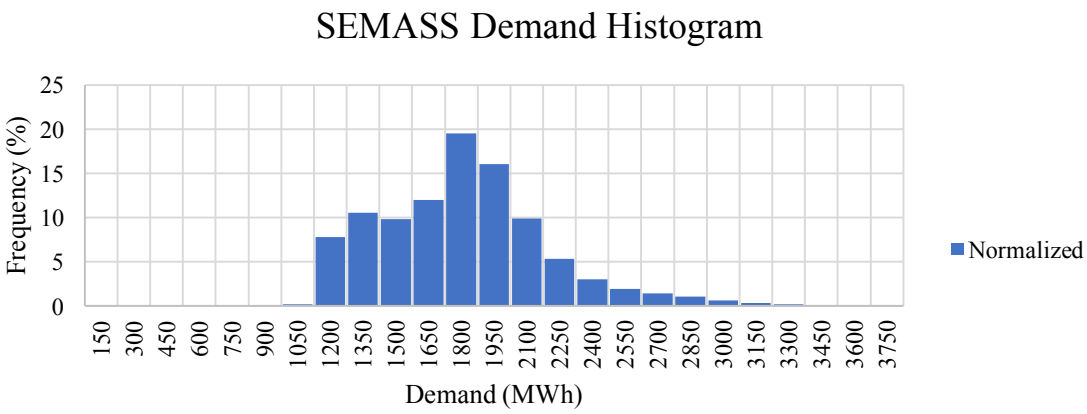

Figure 3.19: Histogram of the 5-year electrical demand data for the Southeastern Massachusetts area.

CHAPTER 4

RESULTS AND DISCUSSION

Section 4.1 discusses the candidate wind farm layouts and the resulting power production based on wind direction, turbulence intensity, and wind speed. Section 4.2 uses these results, coupled with the wind resource data, and evaluates the wind farms based on their relative orientations by creating a power time-series. Section 4.3 uses the power time-series and electrical price data to create a revenue time-series for each wind farm layout. Then, each relative wind farm is oriented in increments from 0° to 180° to obtain new power and revenue time-series for different wind farms.

4.1 Wind Farm Power Tables

This section highlights the wind farm power outputs after simulation with the DWM. Each layout consists of 36 turbines and is simulated with the same wind speed, wind direction, and turbulence intensity parameters that are listed in Table 3.1.

4.1.1 6X6 Square Wind Farm with 6D Spacing

The first wind farm case is a 6X6 square layout (Figure 3.2). Each NREL 5MW turbine is spaced by 6D and is simulated at a hub height of 90m.

After 110 simulations, the results are post-processed and displayed in the power output tables (Tables 4.1 and 4.2). The 6X6 square wind farm has maximum power output for wind direction angles of 20° and 70° for wind speed between 4 and 12 m/s. However, for wind speed between 14 and 24 m/s, rated power is produced for all directions except 0° and 90°. For these directions, the wake effects are most pronounced,

causing a significant impact on downstream turbines and less power production until higher wind speed. Table 4.1 shows the average power of all 36 turbines using their individual averaged power over 650 seconds. Table 4.2 shows the summation of the averaged power for each turbine. To reduce error from initial transients, the first 50 seconds of data are removed before the average power values are calculated.

For each wind speed bin, the probability of the wind being in that bin is calculated with the scale and shape factors (c = 10.2 and k = 1.87). This gives the expected value of power for each wind direction and can also be used to find the capacity factor (CF).

Table 4.1: Average Total Power for all 36 Turbines in the 6X6 Farm with 6D Spacing (MW).

	0°	**10°**	**20°**	**30°**	**40°**	**50°**	**60°**	**70°**	**80°**	**90°**	**Free Stream Avg.**
4 m/s	0.10	0.16	0.17	0.16	0.15	0.15	0.16	0.17	0.16	0.10	0.32
6 m/s	0.47	0.75	0.78	0.73	0.70	0.69	0.73	0.78	0.75	0.47	0.94
8 m/s	1.02	1.66	1.72	1.61	1.51	1.53	1.60	1.72	1.65	1.02	1.89
10 m/s	1.96	3.18	3.31	3.09	2.95	2.93	3.10	3.31	3.19	1.96	3.50
12 m/s	3.00	4.60	4.69	4.52	4.36	4.38	4.50	4.69	4.59	3.06	4.88
14 m/s	4.50	5.00	5.00	5.00	5.00	5.00	5.00	5.00	5.00	4.51	5.00
16 m/s	5.00	5.00	5.00	5.00	5.00	5.00	5.00	5.00	5.00	5.00	5.00
18 m/s	5.00	5.00	5.00	5.00	5.00	5.00	5.00	5.00	5.00	5.00	5.00
20 m/s	5.00	5.00	5.00	5.00	5.00	5.00	5.00	5.00	5.00	5.00	5.00
22 m/s	5.00	5.00	5.00	5.00	5.00	5.00	5.00	5.00	5.00	5.00	5.00
24 m/s	5.00	5.00	5.00	5.00	5.00	5.00	5.00	5.00	5.00	5.00	5.00
Expec. Value	1.81	2.32	2.36	2.29	2.23	2.23	2.29	2.36	2.32	1.81	2.48
CF	0.36	0.46	0.47	0.46	0.45	0.45	0.46	0.47	0.46	0.36	0.50

Table 4.2: Summation of the Average Total Power for all 36 Turbines in the 6X6 Farm with 6D Spacing (MW).

	0°	10°	20°	30°	40°	50°	60°	70°	80°	90°	Free Steam Avg.
4 m/s	3.69	5.86	6.06	5.74	5.35	5.46	5.67	6.08	5.81	3.69	11.52
6 m/s	16.87	27.04	28.19	26.32	25.03	24.94	26.43	28.16	27.09	16.87	33.84
8 m/s	36.77	59.73	61.93	58.05	54.52	55.05	57.59	62.05	59.41	36.77	68.04
10 m/s	70.58	114.63	119.24	111.21	106.17	105.66	111.73	119.18	114.80	70.58	126.00
12 m/s	108.35	165.56	168.83	162.70	156.85	157.78	162.08	168.93	165.23	110.25	175.68
14 m/s	162.21	179.81	179.81	179.61	179.69	179.46	179.73	179.79	179.77	162.21	180.00
16 m/s	179.72	180.00	180.00	180.00	180.00	180.00	180.00	180.00	180.00	179.73	180.00
18 m/s	180.00	180.00	180.00	180.00	180.00	180.00	180.00	180.00	180.00	180.00	180.00
20 m/s	180.00	180.00	180.00	180.00	180.00	180.00	180.00	180.00	180.00	180.00	180.00
22 m/s	180.00	180.00	180.00	180.00	180.00	180.00	180.00	180.00	180.00	180.00	180.00
24 m/s	180.00	180.00	180.00	180.00	180.00	180.00	180.00	180.00	180.00	180.00	180.00
Expec. Value	65.07	83.49	84.97	82.35	80.30	80.40	82.30	84.99	83.43	65.27	89.13
CF	0.36	0.46	0.47	0.46	0.45	0.45	0.46	0.47	0.46	0.36	0.50

4.1.2 9X4 Rectangular Wind Farm with 6D Spacing

The second case study is a 9X4 rectangular wind farm (Figure 3.3). Each turbine is spaced with 6D and is simulated with the wind speed, wind direction, and turbulence intensity parameters at a hub height of 90m. The rectangle was selected to see how the powers differed, if at all, from the square wind farm.

The rectangular wind farm exhibits power output similarly to the square wind farm, with optimal directions of 20° and 70° for wind speed between 4 and 12 m/s and rated power outputs for speed higher than 14 m/s. Figure 3.3 illustrates that when the wind is coming from 20° or 70°, upstream wind turbines directly impact fewer turbines downstream and thus more power is generated. Due to increased wake effects, directions of 0° and 90° for 14 m/s and 16 m/s produce less than rated power outputs. Tables 4.3

and 4.4 show the average power per turbine and the summation of the averages from each direction.

Table 4.3: Average Total Power for all 36 Turbines in the 9X4 Farm with 6D Spacing (MW).

	0°	10°	20°	30°	40°	50°	60°	70°	80°	90°	Free Stream Avg.
4 m/s	0.11	0.16	0.17	0.16	0.15	0.15	0.16	0.17	0.16	0.10	0.32
6 m/s	0.50	0.76	0.78	0.74	0.70	0.70	0.73	0.78	0.75	0.45	0.94
8 m/s	1.09	1.67	1.72	1.64	1.52	1.54	1.59	1.72	1.64	0.98	1.89
10 m/s	2.08	3.20	3.32	3.14	2.96	2.95	3.09	3.31	3.18	1.89	3.50
12 m/s	3.18	4.61	4.70	4.56	4.37	4.40	4.49	4.69	4.58	2.89	4.88
14 m/s	4.66	5.00	5.00	5.00	5.00	5.00	5.00	5.00	5.00	4.51	5.00
16 m/s	5.00	5.00	5.00	5.00	5.00	5.00	5.00	5.00	5.00	4.98	5.00
18 m/s	5.00	5.00	5.00	5.00	5.00	5.00	5.00	5.00	5.00	5.00	5.00
20 m/s	5.00	5.00	5.00	5.00	5.00	5.00	5.00	5.00	5.00	5.00	5.00
22 m/s	5.00	5.00	5.00	5.00	5.00	5.00	5.00	5.00	5.00	5.00	5.00
24 m/s	5.00	5.00	5.00	5.00	5.00	5.00	5.00	5.00	5.00	5.00	5.00
Expec. Value	1.87	2.33	2.36	2.30	2.24	2.24	2.28	2.36	2.31	1.78	2.48
CF	0.37	0.47	0.47	0.46	0.45	0.45	0.46	0.47	0.46	0.36	0.50

Table 4.4: Summation of the Average Total Power for all 36 Turbines in the 9X4 Farm with 6D Spacing (MW).

	0°	10°	20°	30°	40°	50°	60°	70°	80°	90°	Free Stream Avg.
4 m/s	3.92	5.89	6.08	5.81	5.38	5.48	5.64	6.08	5.78	3.55	11.52
6 m/s	17.97	27.18	28.26	26.76	25.17	25.08	26.33	28.14	26.99	16.16	33.84
8 m/s	39.13	60.02	62.10	58.96	54.84	55.35	57.34	62.01	59.19	35.30	68.04
10 m/s	74.92	115.23	119.48	113.01	106.73	106.21	111.31	119.12	114.34	67.91	126.00
12 m/s	114.61	166.06	169.14	164.31	157.44	158.33	161.65	168.87	164.85	104.21	175.68
14 m/s	167.60	179.82	179.83	179.70	179.73	179.53	179.75	179.83	179.81	160.87	180.00
16 m/s	179.93	180.00	180.00	180.00	180.00	180.00	180.00	180.00	180.00	179.29	180.00
18 m/s	180.00	180.00	180.00	180.00	180.00	180.00	180.00	180.00	180.00	180.00	180.00
20 m/s	180.00	180.00	180.00	180.00	180.00	180.00	180.00	180.00	180.00	180.00	180.00
22 m/s	180.00	180.00	180.00	180.00	180.00	180.00	180.00	180.00	180.00	180.00	180.00
24 m/s	180.00	180.00	180.00	180.00	180.00	180.00	180.00	180.00	180.00	180.00	180.00
Expec. Value	67.27	83.69	85.07	82.97	80.51	80.60	82.14	84.97	83.28	63.81	89.13
CF	0.37	0.47	0.47	0.46	0.45	0.45	0.46	0.47	0.46	0.36	0.50

In comparison with the square wind farm, the rectangular farm produces slightly more power at 0° and slightly less at 90°. This suggests that there are increased wake effects of 9 turbines compared to 6 in the 90° direction and 4 turbines compared to 6 turbines in the 0° direction. These effects are most apparent due to the shape of the wind farms and how the upstream wind turbine wakes affect the entire row and reduce the power outputs for all downstream turbines. With greater spacing in the prevailing wind direction, wakes have more time to recover and the power outputs are higher.

4.1.3 9X4 Rectangular Wind Farm with 4D and 8D Spacing

The third candidate wind farm is the 9X4 rectangular layout with 4D and 8D spacing (Figure 3.4). Each wind direction is simulated at a hub height of 90m.

The 9X4 farm exhibits optimum wind directions of 10° and 70° for wind speed between 4 and 14 m/s. Once wind speed exceeds 16 m/s, rated power was reached for all directions except 90°. This is because of the 9 turbines in succession and the 4D spacing between each turbine. In comparison with the 9X4 rectangular wind farm with 6D spacing, the 9X4 with 4D and 8D sees an increase in power production for wind directions where the spacing of turbines is increased (from 6D to 8D). However, for turbines that see a reduction in spacing (from 6D to 4D), less power is produced. Tables 4.5 and 4.6 show the average power per turbine and the summation of the averages from each direction.

Table 4.5: Average Total Power for all 36 Turbines in the 9X4 Farm with 4D and 8D Spacing (MW).

	0°	10°	20°	30°	40°	50°	60°	70°	80°	90°	Free Stream Avg.
4 m/s	0.12	0.17	0.16	0.14	0.16	0.16	0.16	0.17	0.14	0.08	0.32
6 m/s	0.55	0.78	0.75	0.66	0.75	0.75	0.75	0.79	0.63	0.37	0.94
8 m/s	1.20	1.72	1.64	1.44	1.64	1.65	1.65	1.74	1.40	0.84	1.89
10 m/s	2.29	3.31	3.18	2.76	3.17	3.17	3.17	3.33	2.71	1.61	3.50
12 m/s	3.55	4.70	4.72	4.65	4.57	4.58	4.61	4.71	4.69	3.33	4.88
14 m/s	4.85	5.00	5.00	4.99	4.99	4.99	4.99	5.00	5.00	4.74	5.00
16 m/s	5.00	5.00	5.00	5.00	5.00	5.00	5.00	5.00	5.00	4.78	5.00
18 m/s	5.00	5.00	5.00	5.00	5.00	5.00	5.00	5.00	5.00	4.98	5.00
20 m/s	5.00	5.00	5.00	5.00	5.00	5.00	5.00	5.00	5.00	5.00	5.00
22 m/s	5.00	5.00	5.00	5.00	5.00	5.00	5.00	5.00	5.00	5.00	5.00
24 m/s	5.00	5.00	5.00	5.00	5.00	5.00	5.00	5.00	5.00	5.00	5.00
Expec. Value	1.98	2.36	2.33	2.22	2.32	2.31	2.32	2.37	2.21	1.76	2.48
CF	0.40	0.47	0.47	0.44	0.46	0.46	0.46	0.47	0.44	0.35	0.50

Table 4.6: Summation of the Average Total Power for all 36 Turbines in the 9X4 Farm with 4D and 8D Spacing (MW).

	0°	10°	20°	30°	40°	50°	60°	70°	80°	90°	Free Stream Avg.
4 m/s	4.31	6.01	5.78	5.18	5.78	5.85	5.87	6.14	4.94	3.03	11.52
6 m/s	19.86	28.17	26.98	23.59	26.96	26.90	26.97	28.40	22.76	13.46	33.84
8 m/s	43.06	62.04	59.08	52.00	59.01	59.36	59.48	62.48	50.38	30.12	68.04
10 m/s	82.43	119.20	114.45	99.28	114.25	114.02	114.17	120.03	97.74	57.86	126.00
12 m/s	127.86	169.20	169.92	167.48	164.58	164.95	166.00	169.72	168.83	119.96	175.68
14 m/s	174.47	179.83	179.85	179.79	179.80	179.75	179.80	179.86	179.84	170.80	180.00
16 m/s	180.00	180.00	180.00	180.00	180.00	180.00	180.00	180.00	180.00	172.12	180.00
18 m/s	180.00	180.00	180.00	180.00	180.00	180.00	180.00	180.00	180.00	179.44	180.00
20 m/s	180.00	180.00	180.00	180.00	180.00	180.00	180.00	180.00	180.00	180.00	180.00
22 m/s	180.00	180.00	180.00	180.00	180.00	180.00	180.00	180.00	180.00	180.00	180.00
24 m/s	180.00	180.00	180.00	180.00	180.00	180.00	180.00	180.00	180.00	180.00	180.00
Expec. Value	71.11	85.01	83.81	79.89	83.21	83.26	83.43	85.30	79.43	63.23	89.13
CF	0.40	0.47	0.47	0.44	0.46	0.46	0.46	0.47	0.44	0.35	0.50

4.1.4 6X6 Square Wind Farm with 8D Spacing

The fourth candidate wind farm is a 6X6 square wind farm with 8D spacing (Figure 3.5). This wind farm is simulated through the DWM with the wind speed and turbulence intensity parameter at a hub height of 90m. The 8D spacing between turbines is chosen to see how it differs from the 6D and if higher power totals could be produced.

The wind farm has optimal wind directions of 20° and 70° until rated power is reached (14m/s). In comparison with the 6X6 square wind farm with 6D spacing, the power outputs for the 8D farm have higher values, especially for wind directions that experience increased wake effects (0°, 40°, 90°). Tables 4.7 and 4.8 show the average power per turbine and the summation of the averages from each direction.

Table 4.7: Average Total Power for all 36 Turbines in the 6X6 Farm with 8D Spacing (MW).

	0°	**10°**	**20°**	**30°**	**40°**	**50°**	**60°**	**70°**	**80°**	**90°**	**Free Stream Avg.**
4 m/s	0.11	0.17	0.17	0.16	0.16	0.16	0.16	0.17	0.17	0.11	0.32
6 m/s	0.53	0.78	0.79	0.76	0.74	0.74	0.76	0.79	0.78	0.53	0.94
8 m/s	1.14	1.72	1.73	1.67	1.62	1.63	1.66	1.73	1.72	1.14	1.89
10 m/s	2.18	3.31	3.33	3.20	3.14	3.13	3.21	3.33	3.31	2.18	3.50
12 m/s	3.38	4.68	4.70	4.61	4.55	4.56	4.60	4.70	4.68	3.38	4.88
14 m/s	4.79	5.00	5.00	4.99	4.99	4.99	4.99	5.00	5.00	4.79	5.00
16 m/s	5.00	5.00	5.00	5.00	5.00	5.00	5.00	5.00	5.00	5.00	5.00
18 m/s	5.00	5.00	5.00	5.00	5.00	5.00	5.00	5.00	5.00	5.00	5.00
20 m/s	5.00	5.00	5.00	5.00	5.00	5.00	5.00	5.00	5.00	5.00	5.00
22 m/s	5.00	5.00	5.00	5.00	5.00	5.00	5.00	5.00	5.00	5.00	5.00
24 m/s	5.00	5.00	5.00	5.00	5.00	5.00	5.00	5.00	5.00	5.00	5.00
Expec. Value	1.93	2.36	2.37	2.32	2.30	2.30	2.32	2.37	2.36	1.93	2.48
CF	0.39	0.47	0.47	0.47	0.46	0.46	0.47	0.47	0.47	0.39	0.50

Table 4.8: Summation of the Average Total Power for all 36 Turbines in the 6X6 Farm with 8D Spacing (MW).

	0°	10°	20°	30°	40°	50°	60°	70°	80°	90°	Free Stream Avg.
4 m/s	4.12	6.08	6.12	5.92	5.71	5.79	5.86	6.13	6.05	4.12	11.52
6 m/s	18.93	28.13	28.37	27.26	26.66	26.59	27.33	28.36	28.16	18.93	33.84
8 m/s	40.96	61.97	62.33	60.10	58.32	58.73	59.78	62.39	61.86	40.96	68.04
10 m/s	78.42	119.03	119.91	115.30	113.14	112.78	115.64	119.88	119.14	78.42	126.00
12 m/s	121.78	168.57	169.29	166.10	163.65	164.05	165.66	169.33	168.49	121.79	175.68
14 m/s	172.55	179.83	179.85	179.76	179.78	179.74	179.79	179.84	179.82	172.55	180.00
16 m/s	180.00	180.00	180.00	180.00	180.00	180.00	180.00	180.00	180.00	180.00	180.00
18 m/s	180.00	180.00	180.00	180.00	180.00	180.00	180.00	180.00	180.00	180.00	180.00
20 m/s	180.00	180.00	180.00	180.00	180.00	180.00	180.00	180.00	180.00	180.00	180.00
22 m/s	180.00	180.00	180.00	180.00	180.00	180.00	180.00	180.00	180.00	180.00	180.00
24 m/s	180.00	180.00	180.00	180.00	180.00	180.00	180.00	180.00	180.00	180.00	180.00
Expec. Value	69.32	84.92	85.21	83.73	82.80	82.86	83.68	85.21	84.91	69.32	89.13
CF	0.39	0.47	0.47	0.47	0.46	0.46	0.47	0.47	0.47	0.39	0.50

4.1.5 9X4 Rectangular Wind Farm with 8D Spacing

The fifth candidate wind farm is a 9X4 rectangular farm with 8D spacing (Figure 3.6). The wind farm is simulated through the DWM with the wind and turbulence intensity parameters at a hub height of 90m for 650 seconds. Like the square wind farm, the 8D spacing is studied to demonstrate power differences from the 6D and if more power could be produced with increased distance between turbines.

After simulation, the rectangular farm exhibits optimum wind directions of 20° and 70° up until rated power is reached. This wind farm differs from the rectangular with 6D spacing because it produces more power in all directions, in particular, wind directions where the turbines have increased wake effects. Similar to the rectangle with

6D spacing, the farm produces more power in the 0° direction compared with that of the 90° direction due to less turbines in succession. Tables 4.9 and 4.10 show the average power per turbine and the summation of the averages from each direction.

Table 4.9: Average Total Power for all 36 Turbines in the 9X4 Farm with 8D Spacing (MW).

	0°	10°	20°	30°	40°	50°	60°	70°	80°	90°	Free Stream Avg.
4 m/s	0.12	0.17	0.17	0.17	0.16	0.16	0.16	0.17	0.17	0.11	0.32
6 m/s	0.55	0.78	0.79	0.76	0.74	0.74	0.76	0.79	0.78	0.51	0.94
8 m/s	1.20	1.72	1.73	1.68	1.62	1.64	1.66	1.73	1.72	1.10	1.89
10 m/s	2.29	3.31	3.33	3.23	3.15	3.14	3.21	3.33	3.31	2.10	3.50
12 m/s	3.32	4.57	4.59	4.50	4.42	4.40	4.47	4.58	4.56	3.08	4.88
14 m/s	4.74	4.99	4.99	4.99	4.99	4.99	4.99	4.99	4.99	4.56	5.00
16 m/s	5.00	5.00	5.00	5.00	5.00	5.00	5.00	5.00	5.00	5.00	5.00
18 m/s	5.00	5.00	5.00	5.00	5.00	5.00	5.00	5.00	5.00	5.00	5.00
20 m/s	5.00	5.00	5.00	5.00	5.00	5.00	5.00	5.00	5.00	5.00	5.00
22 m/s	5.00	5.00	5.00	5.00	5.00	5.00	5.00	5.00	5.00	5.00	5.00
24 m/s	5.00	5.00	5.00	5.00	5.00	5.00	5.00	5.00	5.00	5.00	5.00
Expec. Value	1.94	2.35	2.35	2.32	2.29	2.29	2.31	2.35	2.35	1.86	2.48
CF	0.39	0.47	0.47	0.46	0.46	0.46	0.46	0.47	0.47	0.37	0.50

Table 4.10: Summation of the Average Total Power for all 36 Turbines in the 9X4 Farm with 8D Spacing (MW).

	0°	10°	20°	30°	40°	50°	60°	70°	80°	90°	Free Stream Avg.
4 m/s	4.31	6.09	6.13	5.98	5.73	5.81	5.85	6.13	6.04	3.99	11.52
6 m/s	19.86	28.17	28.41	27.51	26.74	26.67	27.27	28.35	28.13	18.31	33.84
8 m/s	43.05	62.04	62.42	60.60	58.49	58.89	59.63	62.38	61.80	39.55	68.04
10 m/s	82.41	119.19	120.01	116.29	113.43	113.08	115.41	119.86	119.04	75.77	126.00
12 m/s	119.59	164.37	165.40	161.99	158.96	158.54	160.80	165.05	164.05	110.90	175.68
14 m/s	170.79	179.72	179.74	179.67	179.72	179.62	179.72	179.74	179.72	164.85	180.00
16 m/s	180.00	180.00	180.00	180.00	180.00	180.00	180.00	180.00	180.00	179.97	180.00
18 m/s	180.00	180.00	180.00	180.00	180.00	180.00	180.00	180.00	180.00	180.00	180.00
20 m/s	180.00	180.00	180.00	180.00	180.00	180.00	180.00	180.00	180.00	180.00	180.00
22 m/s	180.00	180.00	180.00	180.00	180.00	180.00	180.00	180.00	180.00	180.00	180.00
24 m/s	180.00	180.00	180.00	180.00	180.00	180.00	180.00	180.00	180.00	180.00	180.00
Expec. Value	69.96	84.51	84.83	83.54	82.39	82.35	83.11	84.75	84.41	66.91	89.13
CF	0.39	0.47	0.47	0.46	0.46	0.46	0.46	0.47	0.47	0.37	0.50

4.1.6 9X4 Rectangular Wind Farm with 6D and 10D Spacing

The last candidate wind farm is a 9X4 rectangle with 6D and 10D spacing (Figure 3.7). The farm is simulated with the wind speed and turbulence intensity parameters for each direction at a hub height of 90m.

For this configuration, the maximum power output occurs at wind directions of 10° and 40°. This differs from previous candidate wind farms, in that 40° has never been an optimal direction. The is due to increased spacing between rows and columns and reduced wake effects. On the other hand, the 30° direction produces low amounts of power and shows that wake effects still do influence the downstream turbines even with increased spacing. Tables 4.11 and 4.12 show the average power per turbine and the summation of the averages from each direction.

Table 4.11: Average Total Power for all 36 Turbines in the 9X4 Farm with 6D and 10D Spacing (MW).

	0°	10°	20°	30°	40°	50°	60°	70°	80°	90°	Free Stream Avg.
4 m/s	0.13	0.17	0.17	0.14	0.17	0.15	0.16	0.17	0.16	0.10	0.32
6 m/s	0.59	0.79	0.77	0.64	0.79	0.69	0.74	0.77	0.75	0.45	0.94
8 m/s	1.28	1.73	1.70	1.39	1.73	1.50	1.60	1.70	1.64	0.98	1.89
10 m/s	2.45	3.33	3.25	2.68	3.33	2.88	3.08	3.26	3.18	1.89	3.50
12 m/s	3.76	4.71	4.66	4.03	4.70	4.26	4.47	4.66	4.58	2.89	4.88
14 m/s	4.92	5.00	4.99	4.97	4.99	4.98	4.99	4.99	4.99	4.47	5.00
16 m/s	5.00	5.00	5.00	5.00	5.00	5.00	5.00	5.00	5.00	4.98	5.00
18 m/s	5.00	5.00	5.00	5.00	5.00	5.00	5.00	5.00	5.00	5.00	5.00
20 m/s	5.00	5.00	5.00	5.00	5.00	5.00	5.00	5.00	5.00	5.00	5.00
22 m/s	5.00	5.00	5.00	5.00	5.00	5.00	5.00	5.00	5.00	5.00	5.00
24 m/s	5.00	5.00	5.00	5.00	5.00	5.00	5.00	5.00	5.00	5.00	5.00
Expec. Value	2.04	2.37	2.34	2.13	2.37	2.21	2.28	2.35	2.31	1.77	2.48
CF	0.41	0.47	0.47	0.43	0.47	0.44	0.46	0.47	0.46	0.36	0.50

Table 4.12: Summation of the Average Total Power for all 36 Turbines in the 9X4 Farm with 6D and 10D Spacing (MW).

	0°	10°	20°	30°	40°	50°	60°	70°	80°	90°	Free Stream Avg.
4 m/s	4.61	6.13	6.00	4.97	6.14	5.38	5.72	6.02	5.78	3.55	11.52
6 m/s	21.24	28.39	27.71	23.08	28.39	24.82	26.48	27.80	26.99	16.15	33.84
8 m/s	46.08	62.44	61.09	50.02	62.46	53.94	57.58	61.20	59.19	35.29	68.04
10 m/s	88.31	119.91	117.18	96.46	119.94	103.50	110.74	117.39	114.33	67.88	126.00
12 m/s	135.24	169.62	167.61	145.04	169.24	153.49	161.00	167.72	164.85	104.16	175.68
14 m/s	177.03	179.84	179.78	178.77	179.80	179.30	179.72	179.78	179.78	160.82	180.00
16 m/s	180.00	180.00	180.00	180.00	180.00	180.00	180.00	180.00	180.00	179.28	180.00
18 m/s	180.00	180.00	180.00	180.00	180.00	180.00	180.00	180.00	180.00	180.00	180.00
20 m/s	180.00	180.00	180.00	180.00	180.00	180.00	180.00	180.00	180.00	180.00	180.00
22 m/s	180.00	180.00	180.00	180.00	180.00	180.00	180.00	180.00	180.00	180.00	180.00
24 m/s	180.00	180.00	180.00	180.00	180.00	180.00	180.00	180.00	180.00	180.00	180.00
Expec. Value	73.55	85.26	84.36	76.70	85.23	79.46	82.07	84.43	83.27	63.80	89.13
CF	0.41	0.47	0.47	0.43	0.47	0.44	0.46	0.47	0.46	0.35	0.50

4.1.7 Power Drop for the 9X4 Rectangular Farms with 6D and 8D Spacing

The power drop behind the upstream turbine can be illustrated by normalizing the power of the downstream turbines with that of the freestream. Figures 4.1 and 4.2 show the normalized power for the 9X4 rectangular wind farm at 90° and 80° for 6D and 8D spacing. Due to wake effects, the power does drop significantly from the first to the second turbine in line, especially for the 90° case. Also, the 6D spacing between turbines causes less power to be produced compared to that of the 8D.

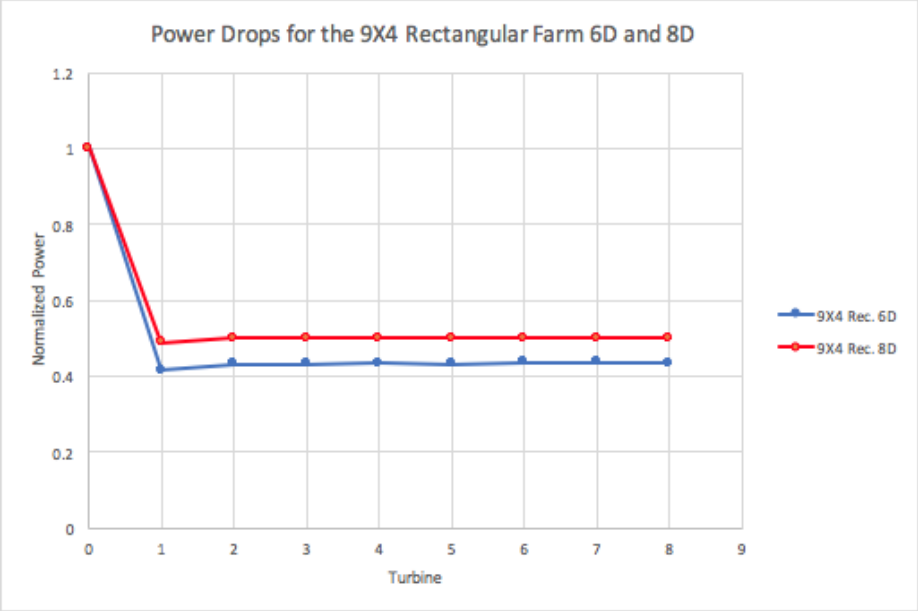

Figure 4.1: Power drop for the 9X4 rectangular farm with 6D and 8D spacing at 90°.

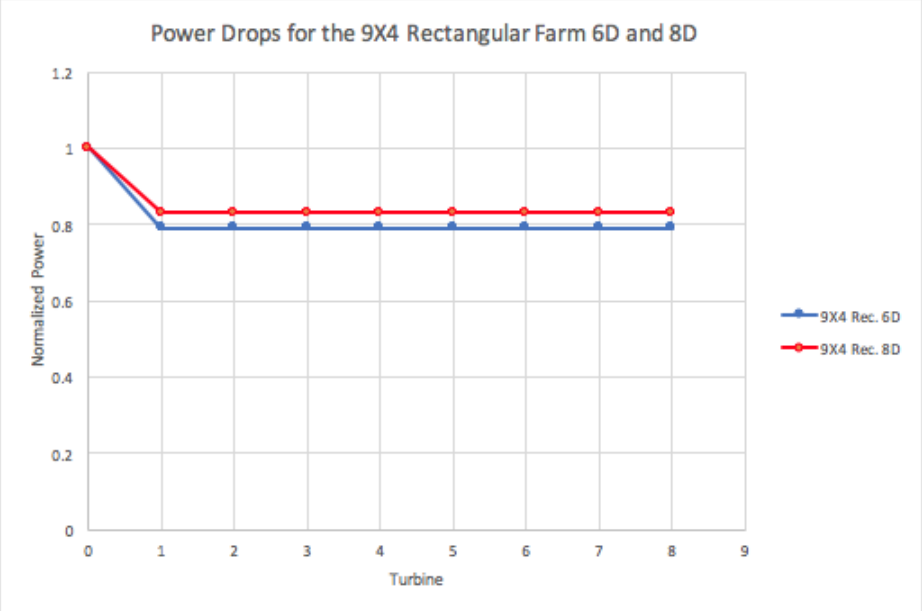

Figure 4.2: Power drop for the 9X4 rectangular farm with 6D and 8D spacing at 80°.

4.2 Metocean Buoy Data Analysis for Nantucket

Using the metocean buoy data, the climatology for the Nantucket, Massachusetts location was analyzed. This data consists of 5 years' worth of wind speed and wind

direction measurements and was interpolated with the power output tables (Section 4.1) to create a time-series of power for every hour over the 5-year period.

4.2.1 Climatology for the Nantucket Buoy Location

The wind resource for this study was characterized by astronomical seasonal variations. Weather patterns change due to differing temperatures, jet stream patterns, and the earth's proximity to the sun. These changes in the weather patterns have been classified as seasons. By analyzing the seasonal variations in the wind resource, insight into an optimal season based on power production, electricity price, and revenue could be attained.

The average seasonal wind speed and direction for years between 2007-2011 are calculated in Figure 4.3. Figure 4.4 shows the overall 5-year seasonal averages.

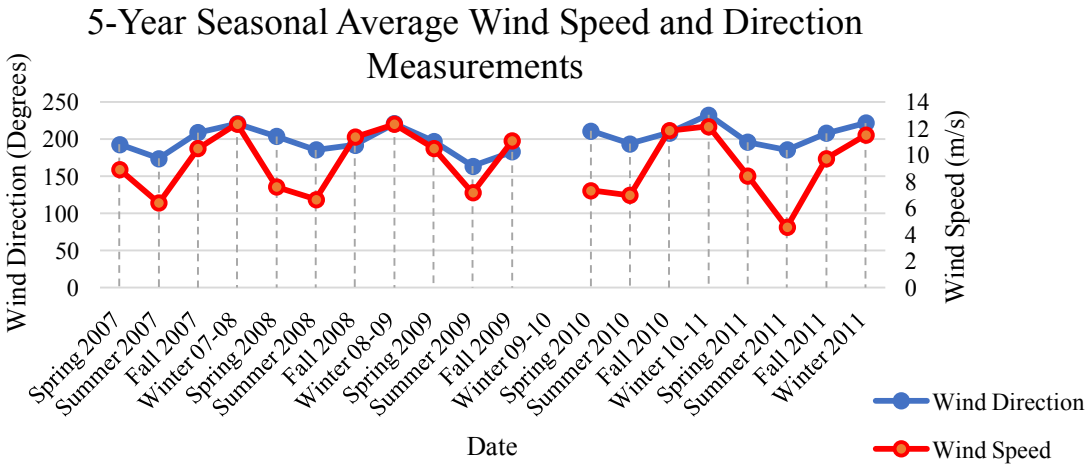

Figure 4.3: Wind speed and direction averages for each season over the 5-year period.

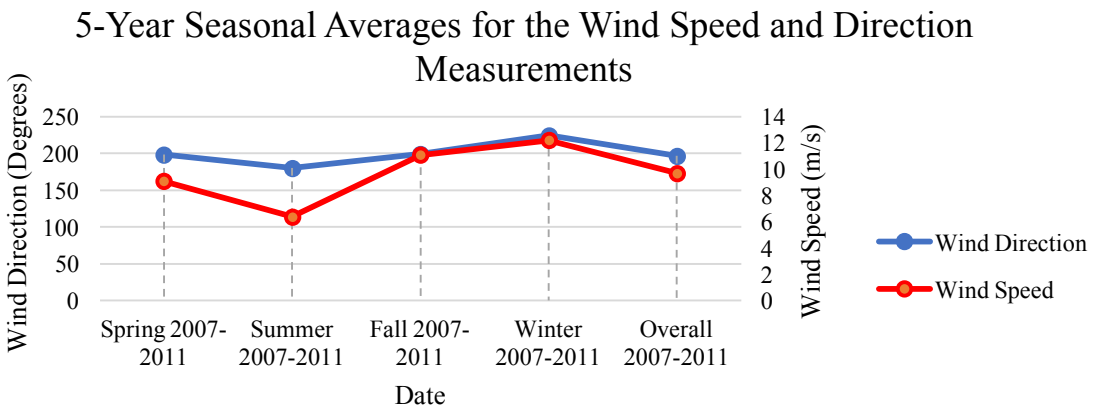

Figure 4.4: 5-year seasonal averages at the SE Nantucket buoy location.

On average, the wind speed is greatest during the winter season. Spring and fall have wind speed that is somewhat reduced, while summer has the slowest wind speed with an average of 6.38 m/s.

This data can also be represented by use of histograms and wind roses. Figures 4.5 and 4.6 show the 5-year data for the spring wind conditions. From the histogram, the wind speed occurred most frequently between 7 and 8 m/s with an average of 9.08 m/s. The wind directions occurred between the south and west with an average of 198.11°.

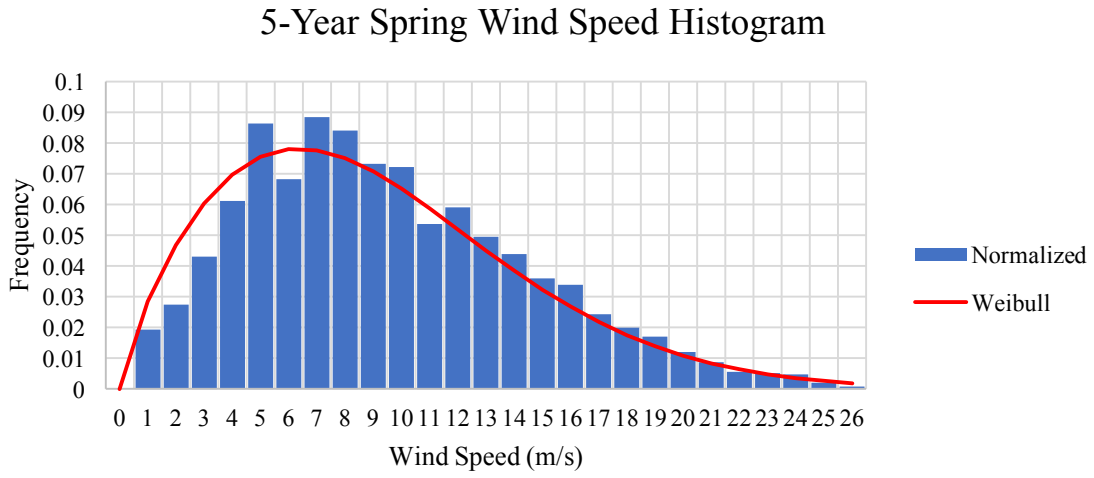

Figure 4.5: Histogram of the spring wind speed for the 5-year period.

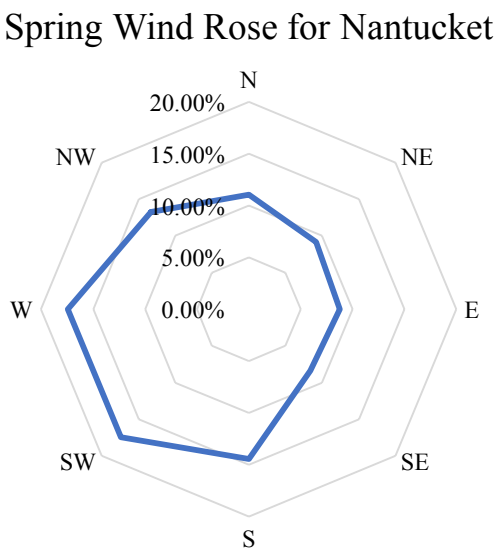

Figure 4.6: Wind rose for the 5-year spring months at Nantucket.

Figures 4.7 and 4.8 show the 5-year wind conditions for the summer season. The histogram illustrates that the highest occurrence of wind speed occurred between 5 and 7 m/s with an average of 6.38 m/s. From the wind rose, the wind directions occurred from the south and southwest more than 20% of the time with an average wind direction of 180.02°.

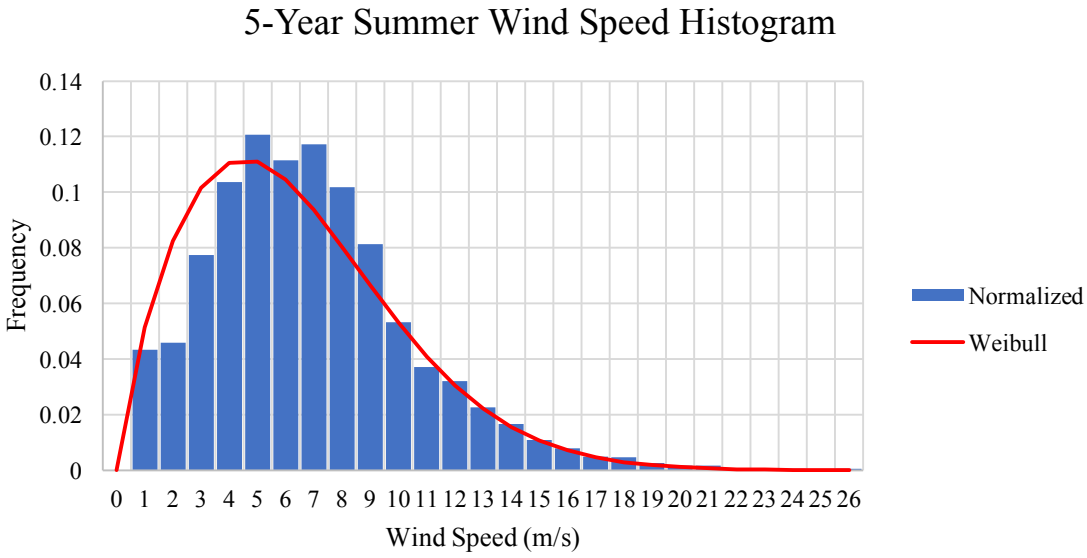

Figure 4.7: Histogram of the summer wind speed for the 5-year period.

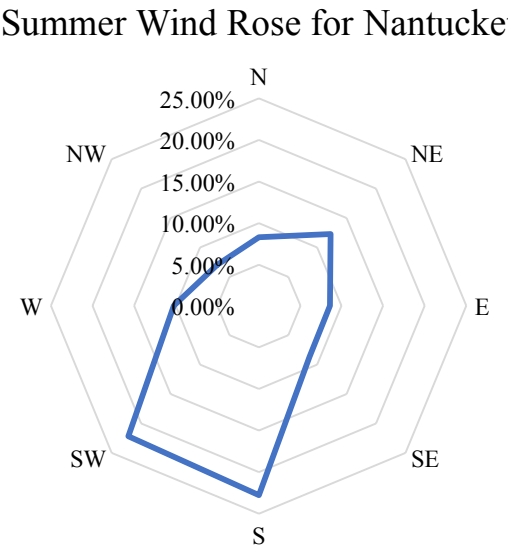

Figure 4.8: Wind rose for the 5-year summer months at Nantucket.

Figures 4.9 and 4.10 are the 5-year wind conditions for the fall season. From the histogram, the wind occurred at higher speeds during the fall with most between 9 and 12 m/s and an average of 11.09 m/s. The directions occurred from the west and northwest around 18% of the time and have an average of 199.05°.

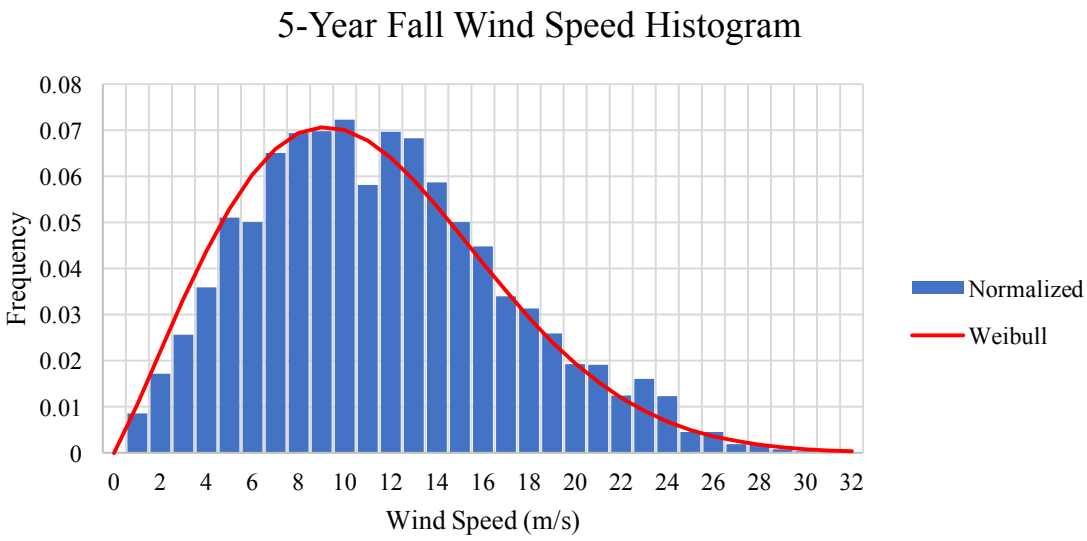

Figure 4.9: Histogram of the fall wind speed for the 5-year period.

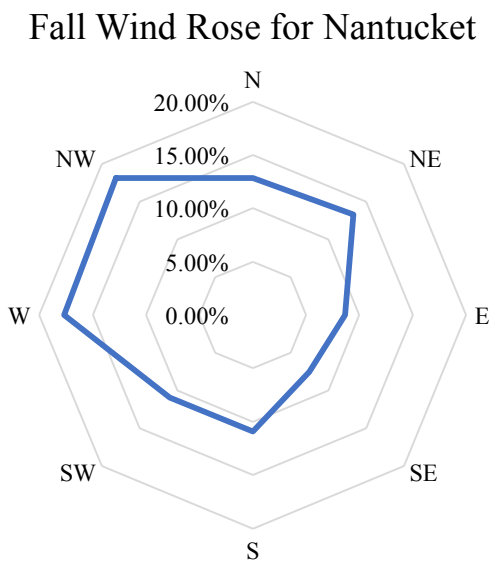

Figure 4.10: Wind rose for the 5-year fall months at Nantucket.

Lastly, figures 4.11 and 4.12 show the wind conditions for the 5-year winter season in Nantucket. From the histogram, the wind speed was strongest during the winter where variations occurred most frequently between 10 and 14 m/s. During these months, the wind speed averaged 12.19 m/s, which was the highest of any of the seasons. The wind rose shows the wind direction occurred 25% of the time from the northwest, but an average of 224.24°.

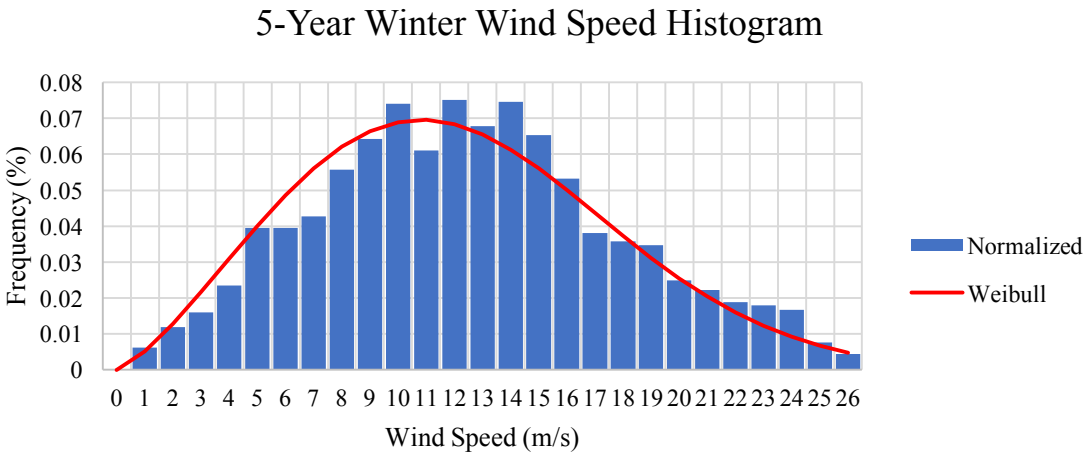

Figure 4.11: Histogram of the winter wind speed for the 5-year period.

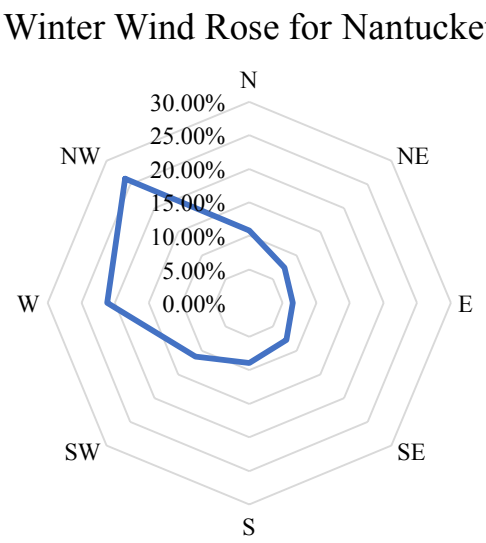

Figure 4.12: Wind rose for the 5-year winter months at Nantucket.

4.2.2 Power Time-Series

Through interpolation of the power output tables (selection of a power from the table per the wind speed and direction at each hour) in section 4.1, a power time-series was created for each candidate wind farm using the wind data from the Southeastern Nantucket buoy location. Figure 4.13 shows the power time-series for the 6X6 square wind farm with 6D spacing.

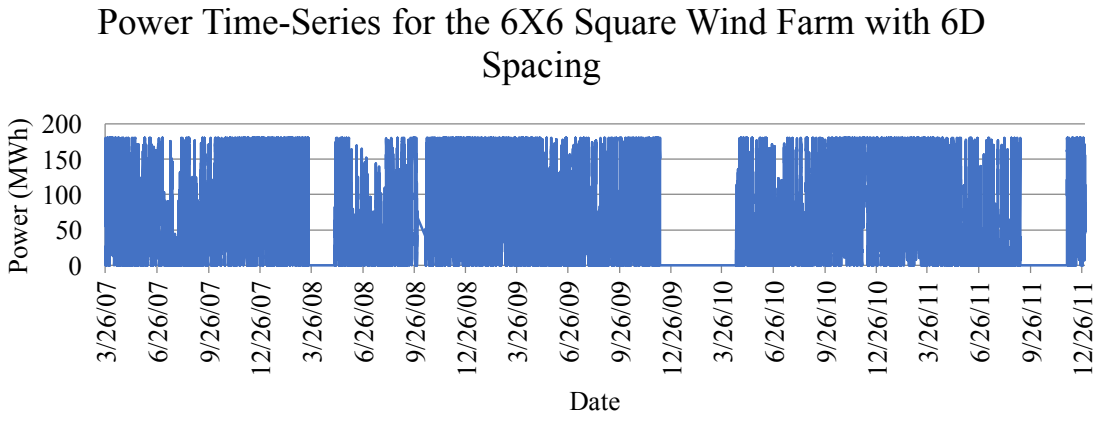

Figure 4.13: Power time-series for the 6X6 square wind farm, 6D spacing, with a 0° orientation.

The other candidate wind farm power time-series data are similar in appearance to the 6X6 square wind farm and are in Appendix B.

The mean power outputs for each farm over the 5-years was obtained from the power time-series and is indicated in Figure 4.14. The square wind farm with 8D spacing sees the most power production due to increased spacing between turbines and minimized wake effects throughout the farm. The least amount of total power production is observed from the 9X4 rectangular farm with 4D and 8D spacing. Due to the small amount of distance between certain turbines, wake effects are maximized and power output is limited.

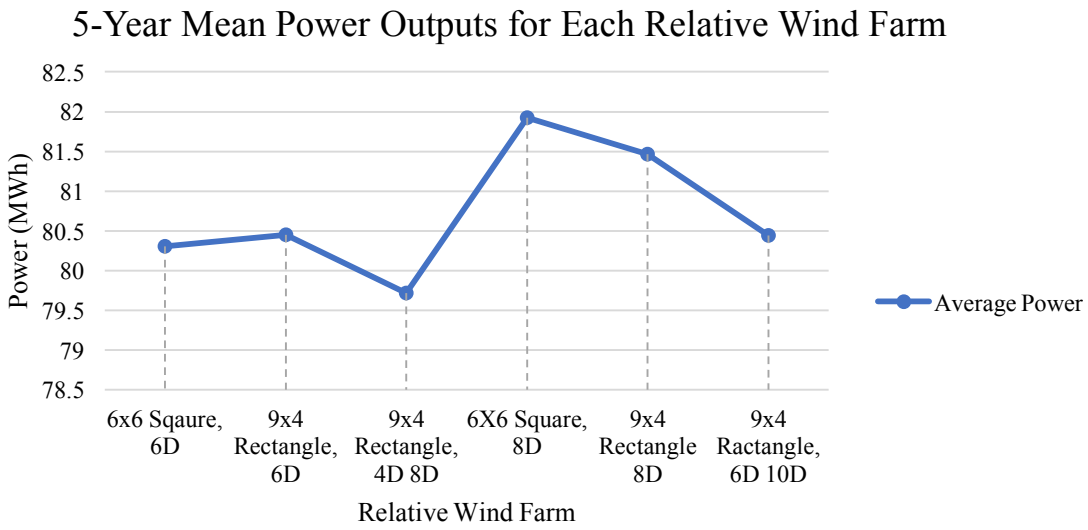

Figure 4.14: 5-year mean power outputs for all relative wind farms.

Through interpolation of the power time-series and electricity price data, a revenue time-series was created for each candidate wind farm.

4.3 Wind Farm Revenue

This section highlights the revenue time-series, maximum and minimum wind farm orientations, and total revenue of the candidate wind farms. Comparisons between the maximum and minimum power orientations are also detailed.

4.3.1 SE ISO New England Electricity Data

The electrical data obtained from ISO New England is used in parallel with the power time-series (Section 4.2) to create a revenue time-series. Figures 4.15 and 4.16 show the 5-year average power price and demand measurements as well as the total average for each season during the 5-year period.

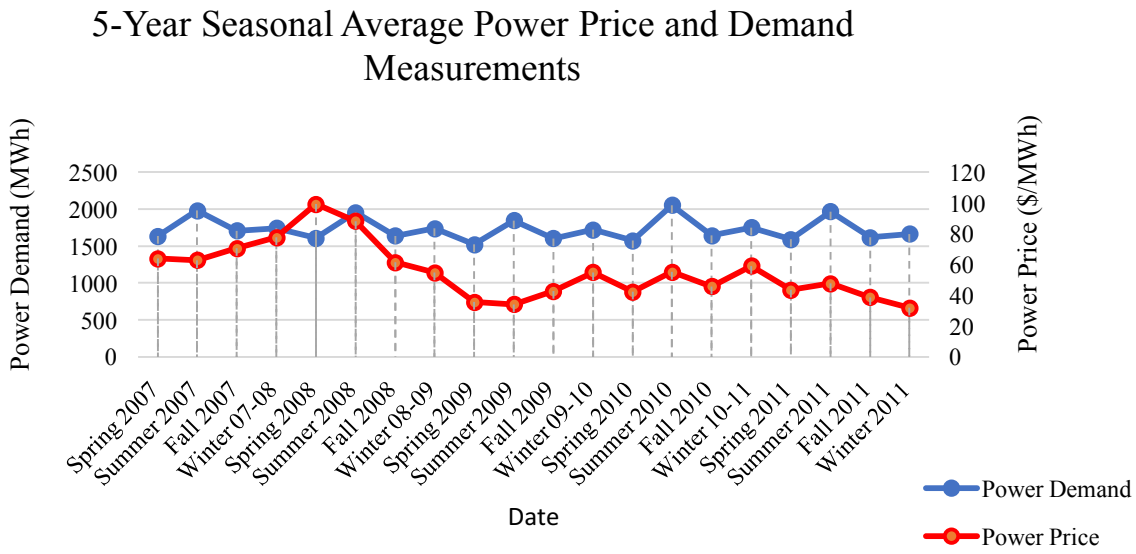

Figure 4.15: 5-year seasonal average power price and demand measurements from Southeastern New England.

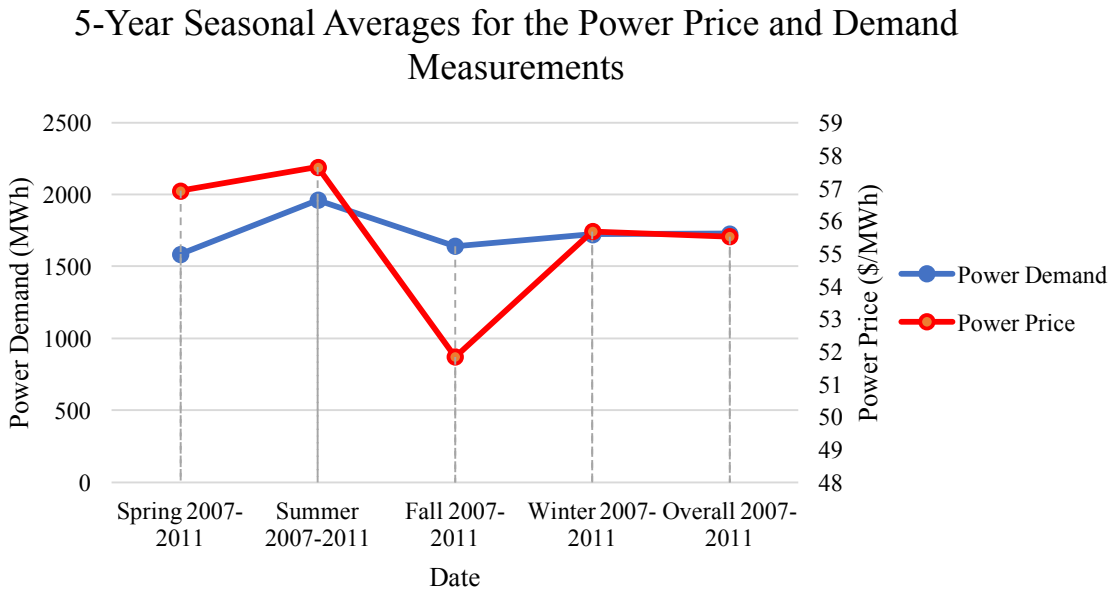

Figure: 4.16: 5-year seasonal averages for the power price and demand in Southeastern New England.

From the figures, electricity prices are highest during the summer and spring. However, the high spring average is due to a price anomaly that occurred during the year 2008. The winter season also sees high electricity price values and is comparable to the summer during select years. These results are consistent with extreme temperatures and the need for balance within households, buildings, etc. at certain times during the year.

The relationship between the overall electricity price and wind speed is also interesting to consider. This data was arranged by rank ordering the electricity prices and associating each price with a wind speed. Then, the mean of the electricity price and wind speed was calculated for each price percentile (percent of time such that the price is above some value) (Figure 4.17). As electricity prices increase, wind speed also tends to increase. However, occasionally, a reduction in speed is observed. This could be due to fluctuation in the electricity prices that are related to low wind speed events (high electricity prices, but lower wind speed in the summer). Once the top 95th percentile is

reached, the electricity prices have the highest observed average value and the wind speed has a significant increase from the value observed at 90%.

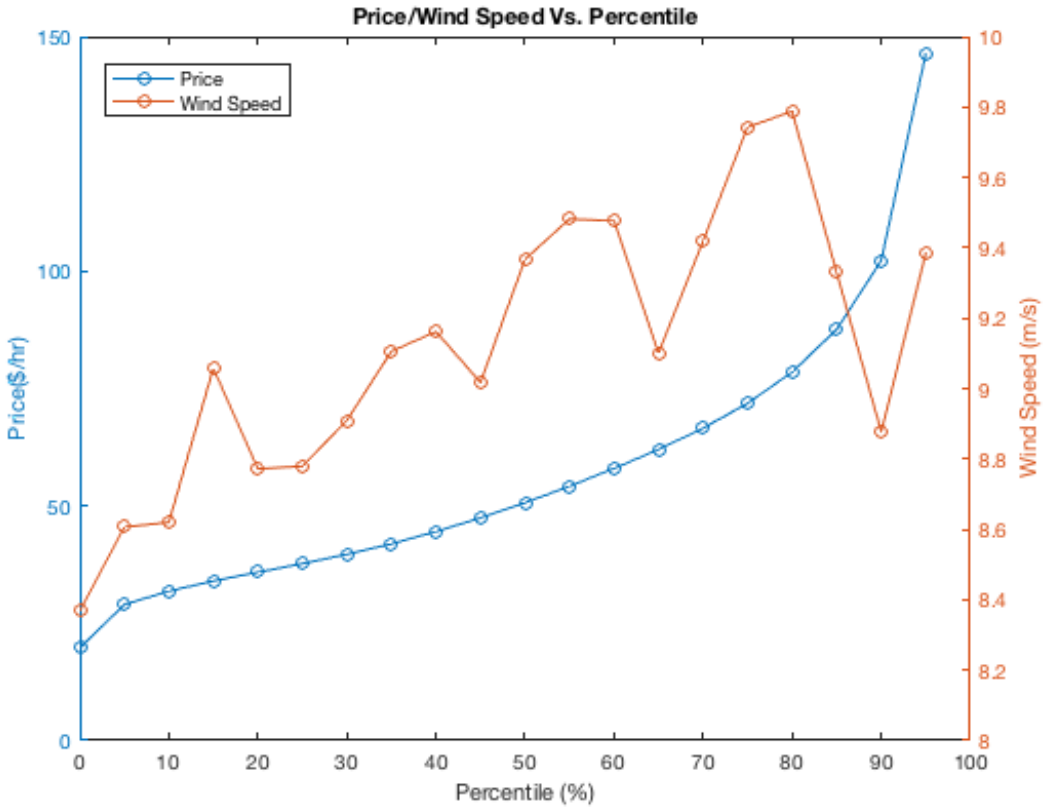

Figure 4.17: Wind speed and price versus price percentile.

4.3.2 Revenue for the 6X6 Square Wind Farm with 6D Spacing

After interpolation of the power and electrical price time-series', a revenue time-series was created for the 6X6 square wind farm with 6D spacing at a 0° orientation (Figure 4.18).

The figure shows the raw revenue time-series data for the entire 5-year period. Due to missing data within the metocean study, revenue values for those time frames were disregarded and are indicated in the figure as linear lines. Figure 4.19 shows the average revenue per season.

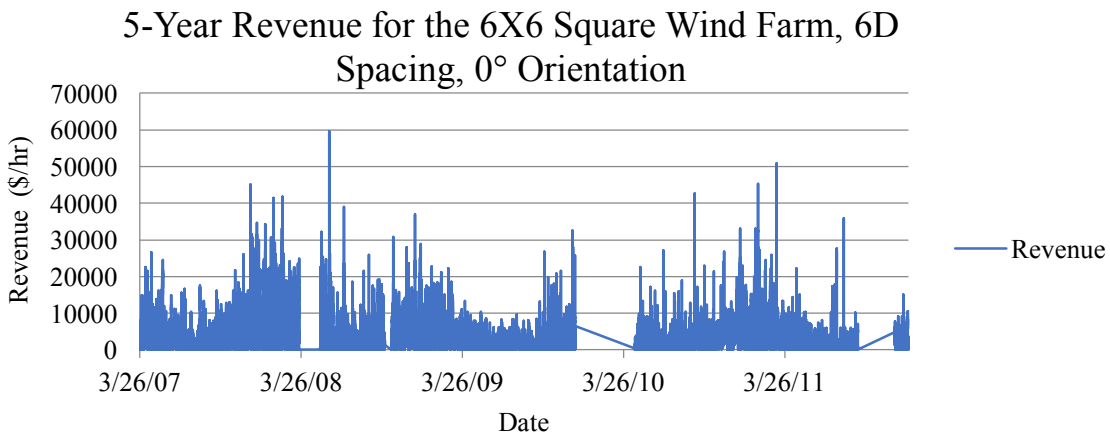

Figure 4.18: Revenue time-series for the 6X6 square wind farm, 6D spacing, at a 0° orientation.

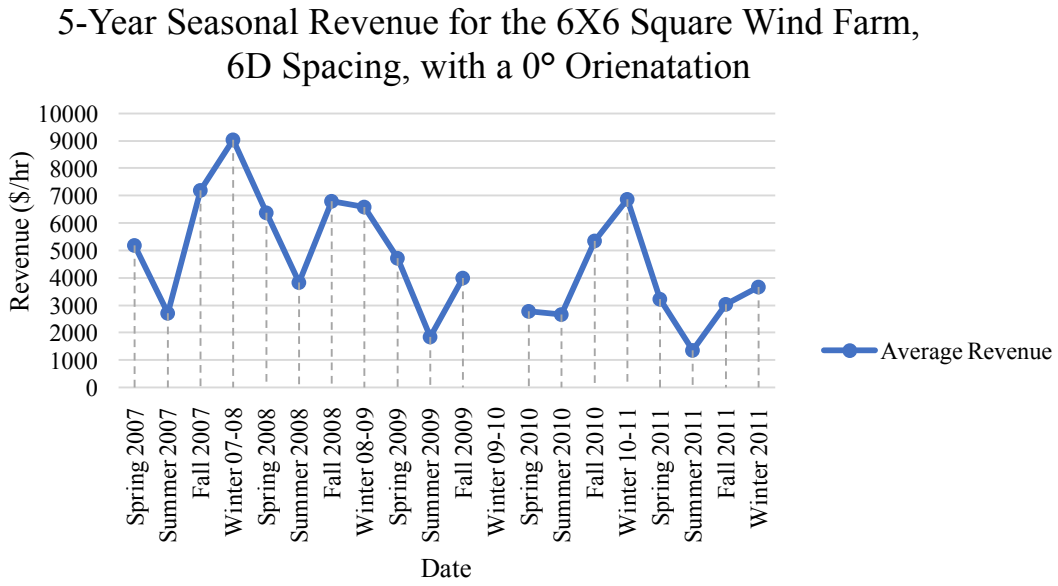

Figure 4.19: 5-year seasonal average revenues and total revenue for the 0° orientation of the 6X6 square wind farm with 6D spacing.

When the wind farm is oriented in a 0° direction, we see the highest average revenue during the winter months. During this season, there are high electricity demands and price, in addition to the highest winds and the most power production potential in SE Nantucket.

4.3.2.1 Revenue for the Orientations of the 6X6 Square Wind Farm with 6D Spacing

By model changing the wind farm orientation, the layout was rotated from 0° to 180° to evaluate and assess new wind farms. For this case study, the wind farm was oriented in 1° increments by interpolation of the 10° results from the DWM, which allowed total revenue values to be calculated at each orientation (Figure 4.20). From the figure, the total revenue for all 5 years for the wind farm at 0° is $159,060,000. When the wind farm is oriented approximately 5° to 6°, total revenue values peaks at around $159,180,000. Due to symmetry of the wind farm, orientations of 95° to 96° also produce the highest total values. These orientations see the highest revenue due to decreased amount of wake effects/more power production and corresponding high electrical prices and wind speed.

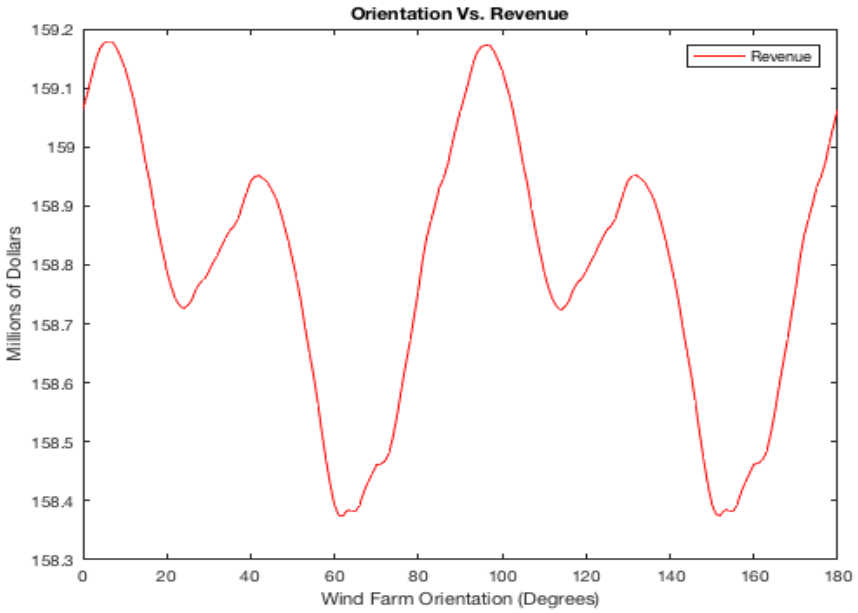

Figure 4.20: Revenue for the 6X6 square wind farm with 6D spacing.

Figure 4.21 shows the relationship between the total revenue and total power for all orientations of the wind farm, normalized by the maximum value. The graphs indicate that a correlation exists between the orientations for the maximum/minimum power and

revenue. The highest total power and revenue are obtained when the wind farm is oriented between 5° and 9°. The lowest values for revenue and power are obtained when the farm is oriented between 60° and 65°.

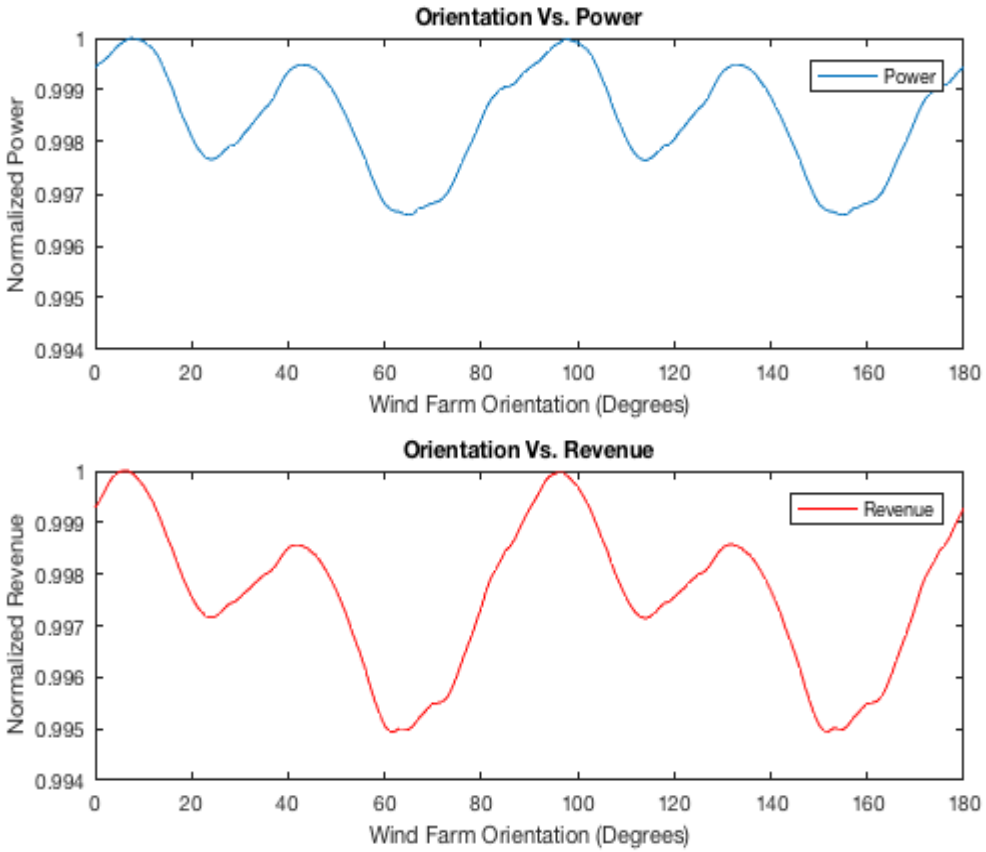

Figure 4.21: Relationship between the total revenues and total powers for the 6X6 square wind farm with 6D spacing.

The relationship between AEP and revenue can also be illustrated with the use of a scatter plot (Figure 4.22). As the AEP increases, the revenue increases. This indicates that higher revenue values occur when the wind speed is high and the wake effects are minimized (high power production) for this location.

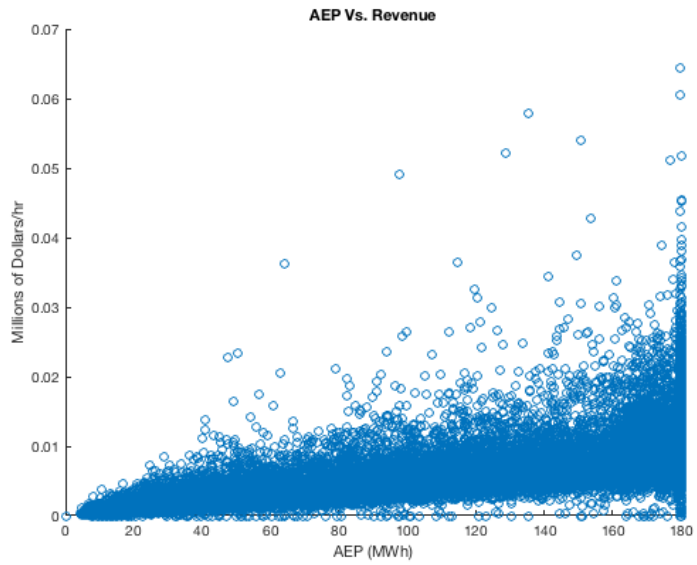

Figure 4.22: AEP versus revenue for the 6X6 square wind farm with 6D spacing.

Figures 4.23 and 4.24 illustrate the 5° orientation and the prevailing wind direction. This relation produces the most power because it minimizes wake effects and therefore maximizes the total power production. The wind rose indicates that this wind farm maximizes revenue and power by orienting in the average prevailing directions observed during the spring and fall. During these seasons, the wind speed is relatively high and the electrical prices are expensive during select spring years.

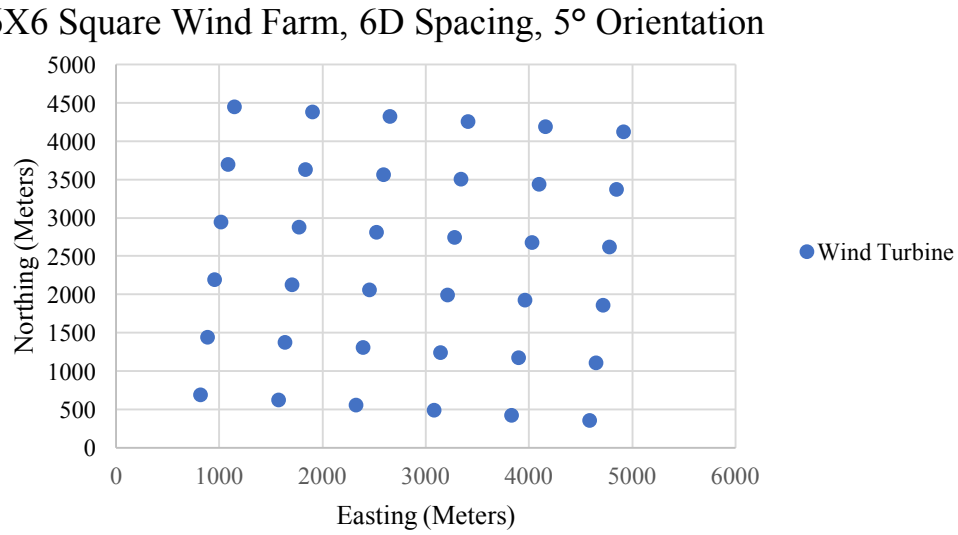

Figure 4.23: 6X6 square wind farm with a 5° orientation.

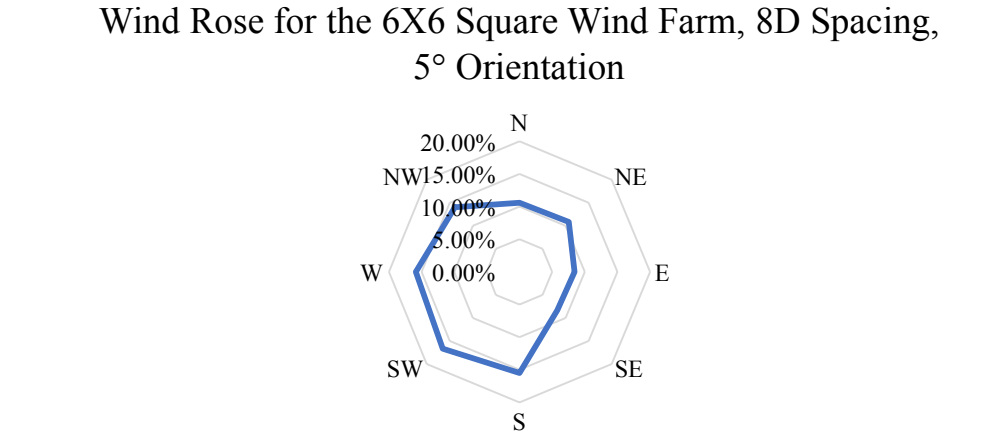

Figure 4.24: Wind rose for the 6X6 square wind farm, 6D spacing, with a 5° orientation.

The lowest total revenue and power occur when the wind farm was oriented between 60° and 65°. Based on the orientation and wind rose (Figures 4.25 and 4.26), the wind farm minimizes power due to increased wake effects, which also corresponds to decreased revenue totals. If the wind is blowing from the southwest on average, the turbines downstream experience the wake effects of all upstream turbines, directly. The observed average prevailing wind direction is comparable to the ones seen during the spring and fall seasons. This indicates that if the wake effects are maximized during these seasons, the wind farm produces low yearly revenue and power totals because of minimized power output when the wind speed is high during a year.

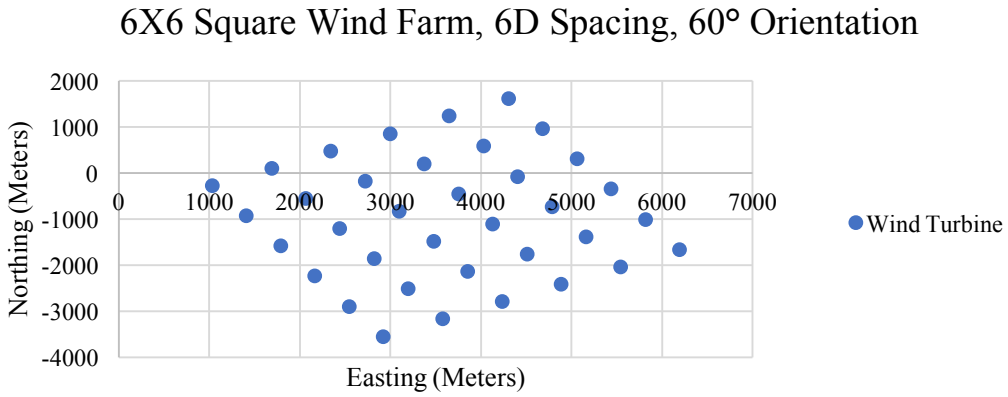

Figure 4.25: 6X6 square wind farm, 6D spacing, with a 60° orientation.

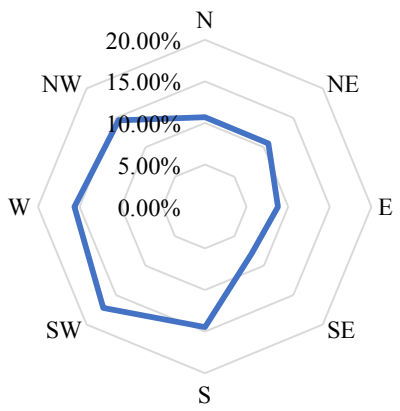

Figure 4.26: Wind rose for the 6X6 square wind farm, 6D spacing, with a 60° orientation.

4.3.3 Summary of the Various Wind Farms and their Orientations

The remaining relative wind farms showed similar characteristics to the 6X6 square wind farm with 6D spacing. The maximum and minimum revenue orientations shared the same values as the powers. This indicates that the maximum revenue is attained when the wake effects are minimized and power outputs are maximized. The conclusions for each wind farm in terms of maximum revenue/power orientation, minimum revenue/power orientation, as well as the maximum revenue/power, and minimum revenue/power are illustrated within Tables 4.13 and 4.14.

The results tables indicate that all the relative wind farms do share a relationship between the maximum and minimum powers and revenues. In example, the 6X6 square wind farm with 8D spacing produced the most revenue, but at the same orientation that saw the max power. This is due to high wind speed and decreased amounts of wake effects. The lowest power and revenue is produced from the 9X4 rectangular wind farm with 4D and 8D spacing. This wind farm also sees the maximum and minimum revenues

at the same orientation as the maximum and minimum powers. Here too, the average wind directions are coupled with the highest wind speed to produce decreased amount of wake effects, high power, and revenue outputs.

Also noted is the total revenue values for each wind farm over the entire 5-year span (Figure 4.27). The maximum was observed from the 6X6 square wind farm with 8D spacing ($162,320,000), but is still a very low value. This is due to missing wind data within the metocean database and below average electrical prices. The wind data accounted for in this study is around 80% of the 5-year total and the average electrical

Table 4.13: Conclusions for the Total Revenue and Orientation of Each Wind Farm.

Layout	**Maximum Revenue Orientation**	**Minimum Revenue Orientation**	**Maximum Revenue**	**Minimum Revenue** **Max/Min Ratio**
6X6 Square Wind Farm with 6D Spacing	5°/95°	60°/151°	~$159,180,000	~$158,370,000 1.005
9X4 Rectangular Wind Farm with 6D Spacing	95°	61°	~$159,480,000	~$158,580,000 1.006
9X4 Rectangular Wind Farm with 4D and 8D Spacing	98°	62°	~$158,530,000	~$156,710,000 1.012
6X6 Square Wind Farm with 8D Spacing	9°/97°	60°/151°	~$162,320,000	~$161,610,000 1.004
9X4 Rectangular Wind Farm with 8D Spacing	99°	60°	~$161,470,000	~$160,650,000 1.005
9X4 Rectangular Wind Farm with 6D and 10D Spacing	98°	62°	~$159,590,000	~$158,670,000 1.006

Table 4.14: Conclusions for the Total Power and Orientation of Each Wind Farm.

Layout	Maximum Power Orientation	Minimum Power Orientation	Maximum Power (MW)	Minimum Power (MW) Max/Min Ratio
6X6 Square Wind Farm with 6D Spacing	7°/98°	65°/155°	~2,791,600	~2,782,100 1.003
9X4 Rectangular Wind Farm with 6D Spacing	98°	64°	~2,797,400	~2,786,100 1.004
9X4 Rectangular Wind Farm with 4D and 8D Spacing	100°	62°	~2,779,100	~2,755,500 1.009
6X6 Square Wind Farm with 8D Spacing	8°/99°	64°/152°	~2,848,100	~2,839,900 1.003
9X4 Rectangular Wind Farm with 8D Spacing	98°	61°	~2,832,700	~2,822,900 1.003
9X4 Rectangular Wind Farm with 6D and 10D Spacing	102°	61°	~2,800,200	~2,787,300 1.005

price is $57/MWh, which is much less than the PPAs typical COE cost of $150/MWh for offshore wind. A back of the envelope calculation shows that 36 5MW turbines with a capacity factor of 0.47 should be producing around $200 million in revenue.

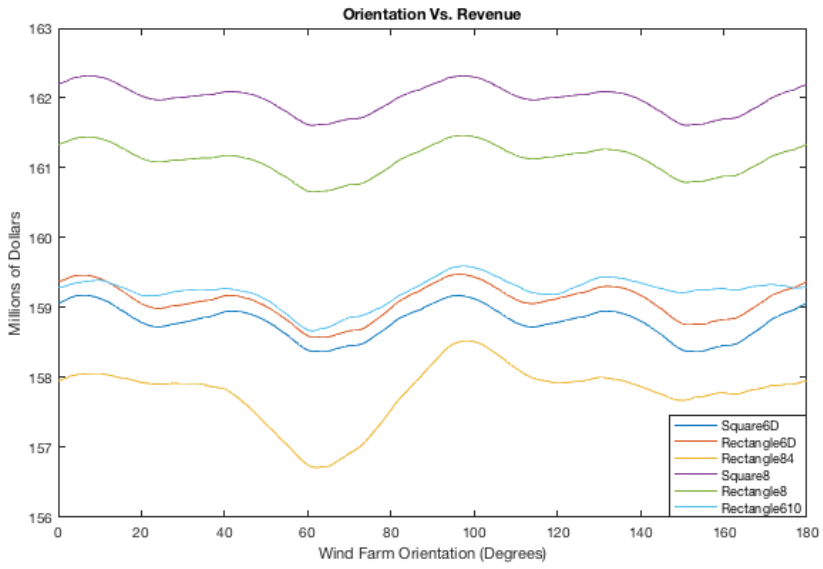

Figure 4.27: Revenue totals for each orientation of the candidate wind farms.

All other figures illustrating the remaining candidate wind farms are in Appendix C.

CHAPTER 5

CONCLUSIONS

Seasonal variation in the electricity price and wind resource was evident for the Nantucket, MA case study location. After evaluating the data set, the winter season on average was when the electricity prices were high and when the wind speed was highest between the years 2008 and 2011. During this season and the fall, the high wind speed also tends to come from the same relative direction. It is because of this relationship between high wind speed and direction that a wind farm microsited to maximize revenue will have the same orientation as a wind farm microsited to maximize power. The high electricity prices in the winter could also be reasoning for the observed small ratios. Additionally, a similar relationship is observed between the minimum values for power and revenue. All the wind farms experience maximized wake effects in the average prevailing wind directions observed when the wind speed is high. This indicates that to avoid lower power and revenue, the wind farms must be oriented to reduce wake effects in the directions that see the highest wind speed. However, overall, this location sees low revenue and power totals and thus, the orientation of the wind farms does not have a significant effect. Therefore, they should be microsited for other criteria (i.e. installation, environmental concerns, etc.). This result coincides with the results observed in the NREL Massachusetts BOEM research study. Orientation had negligible effects on the wind farm efficiency and the candidate wind farms experienced significant wake effects [62].

Furthermore, the power tables obtained within this research study can be used for other locations. However, research and validation into the accuracy of the power values and the wake losses may be needed.

The hypothesis of this study sought to examine the time-series of wind and electrical data at a location to determine how correlation between these two variables impacts optimal wind farm orientation in terms of power and revenue. For Nantucket, Massachusetts, the conclusions indicate that the optimal revenue orientation for all the candidate wind farms is the same orientation that maximizes AEP. The power production, minimized wake effects, and low electricity averages in certain orientations make this location power dominant with electricity prices and revenue having little effect on the optimal orientation. However, since power levels are low, the farms should not be oriented to maximize revenue or power. Nonetheless, other locations could exhibit different behavior if there were two seasons that had equivalent high wind speed values, but opposite average wind directions (i.e. winter and summer have equivalent wind speed, but the average wind direction during the winter is from the east and during the summer it is from the west) and wind farms with greater spacing between turbines. By having two wind directions that produce equivalent wind speed and power outputs, the higher electricity prices will have more of an impact on orientations that seek to maximize revenue rather than power.

Future research should aim to optimize locations where known contrasts occur between the seasonal wind data. As a template, Nantucket, Massachusetts indicates that locations that have lower electricity prices and a dominate wind direction with the highest observed yearly wind speed, should be avoided. Locations that have high electricity

prices and high wind speed in differing wind directions should be considered. Also, simulations with greater spacing between turbines (15D to 20D) to evaluate farms with greater power production and smaller wake effects. This would allow more in-depth research into this micrositing technique and if wind farms seeking to maximize revenue should orient differently from orientations that maximize power.

APPENDIX A

TIME-SERIES ELECTRICAL DATA FOR ISO NEW ENGLAND REGIONS OTHER THAN SEMASS

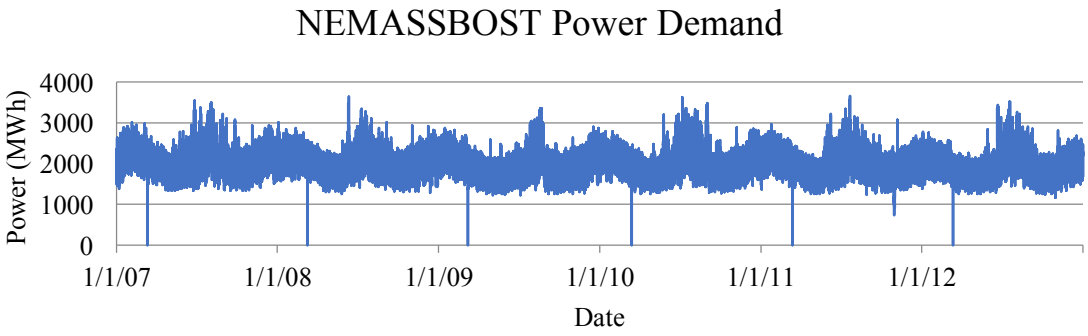

Figure A.1: Time-series of the electrical power demand in Northeastern Massachusetts.

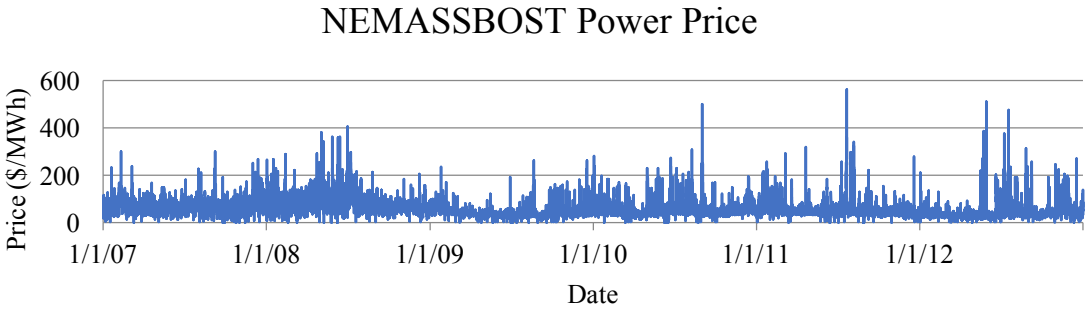

Figure A.2: Time-series of the electrical price in Northeastern Massachusetts.

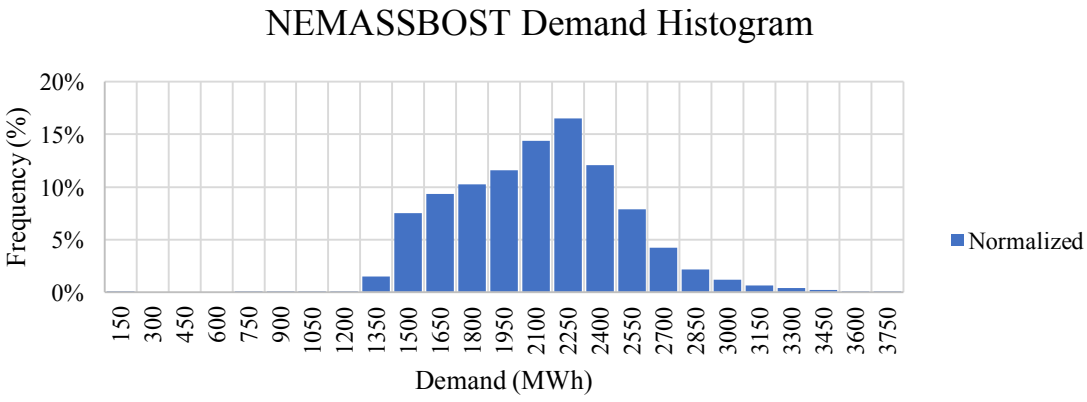

Figure A.3: Histogram of the electrical demand in Northeastern Massachusetts.

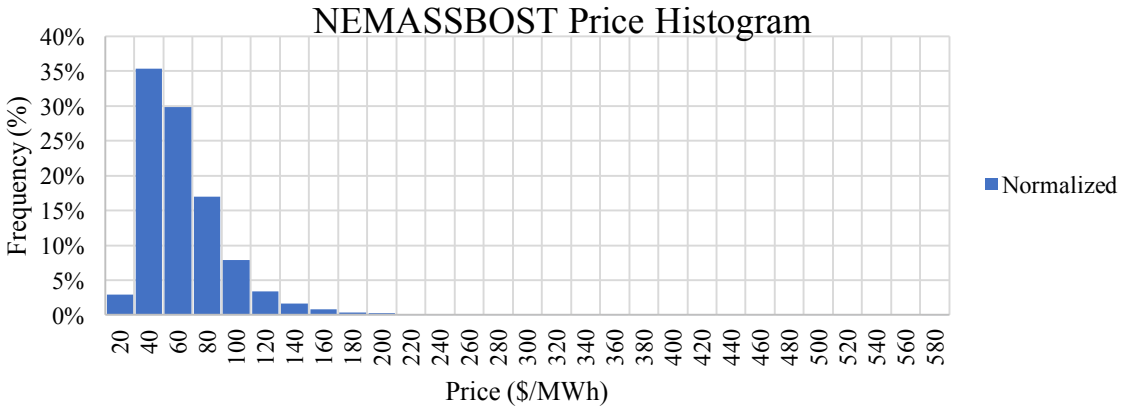

Figure A.4: Histogram of the electrical price in Northeastern Massachusetts.

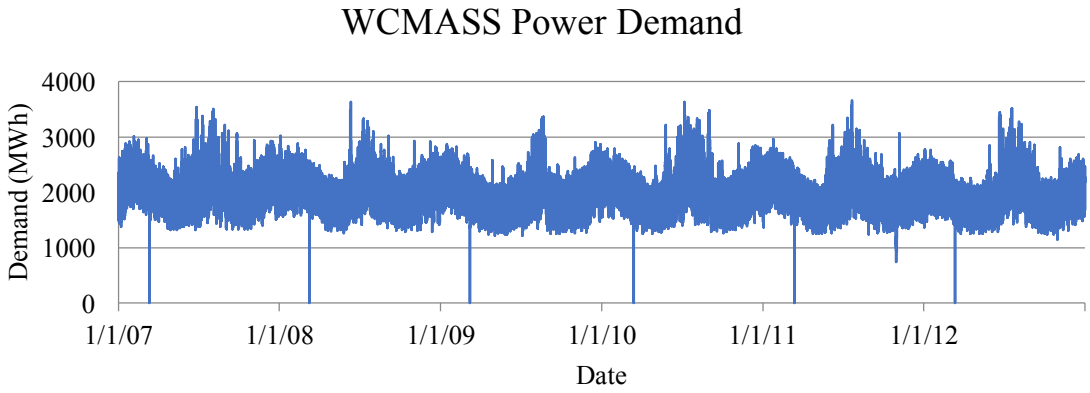

Figure A.5: Time-series of the electrical demand for Western Massachusetts.

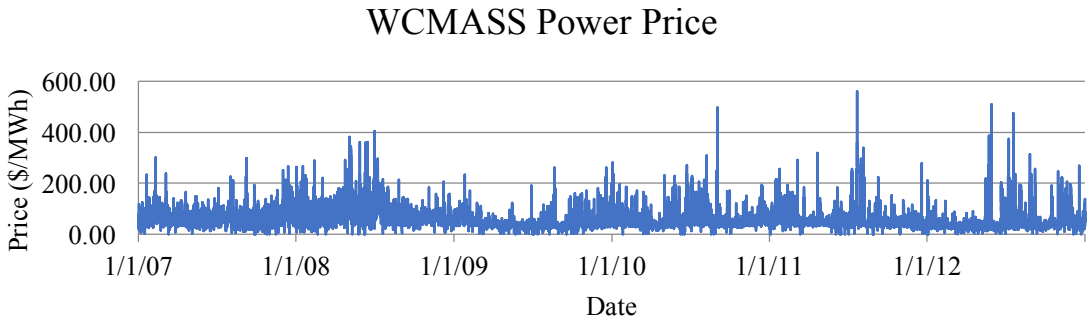

Figure A.6: Time-series of the electrical price for Western Massachusetts.

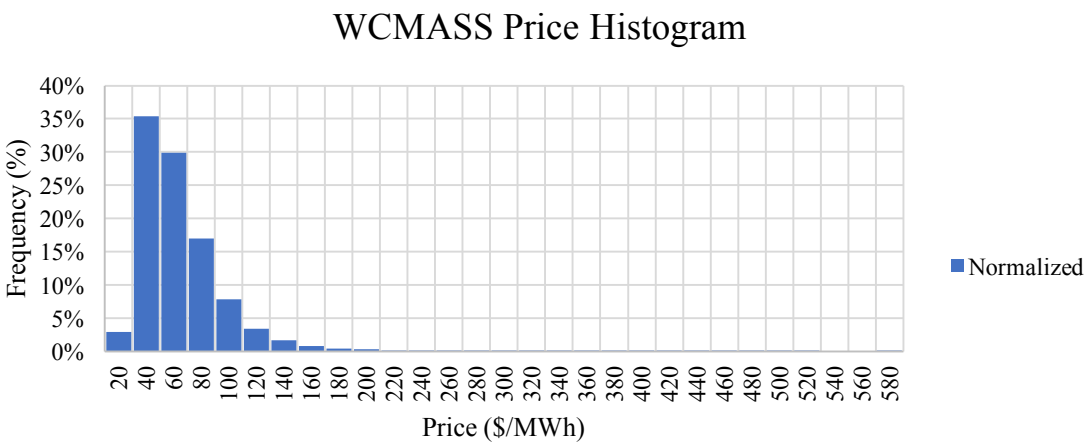

Figure A.7: Histogram of the electrical price in Western Massachusetts.

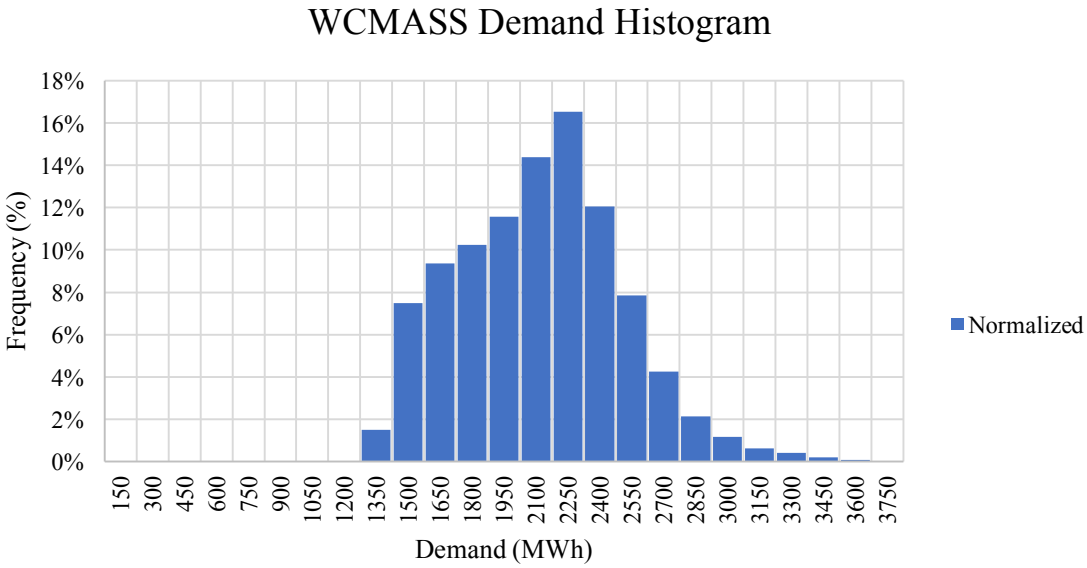

Figure A.8: Histogram of the electrical demand for Western Massachusetts.

APPENDIX B

POWER TIME-SERIES FOR THE CANDIDATE WIND FARMS

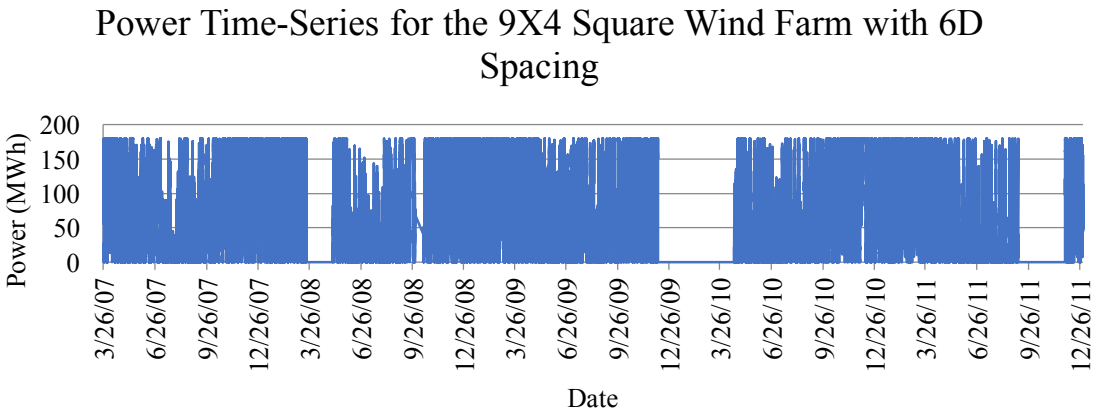

Figure B.1: Power time-series for the 9X4 rectangular wind farm with 6D spacing.

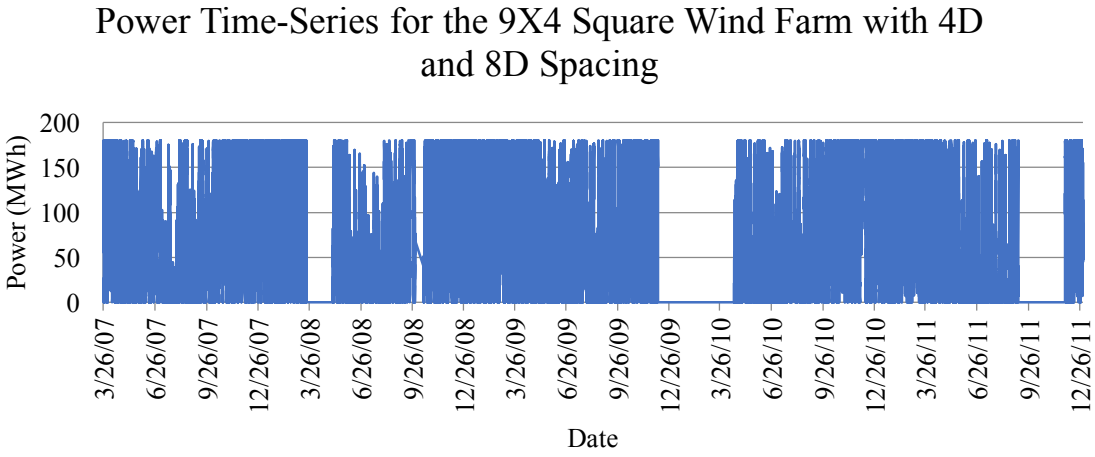

Figure B.2: Power time-series for the 9X4 rectangular wind farm with 4D and 8D spacing.

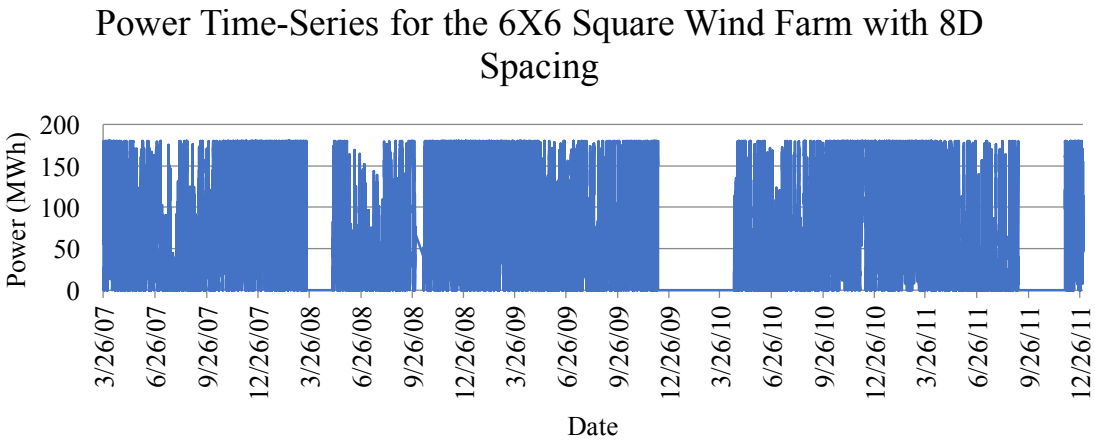

Figure B.3: Power time-series for the 6X6 square wind farm with 8D spacing.

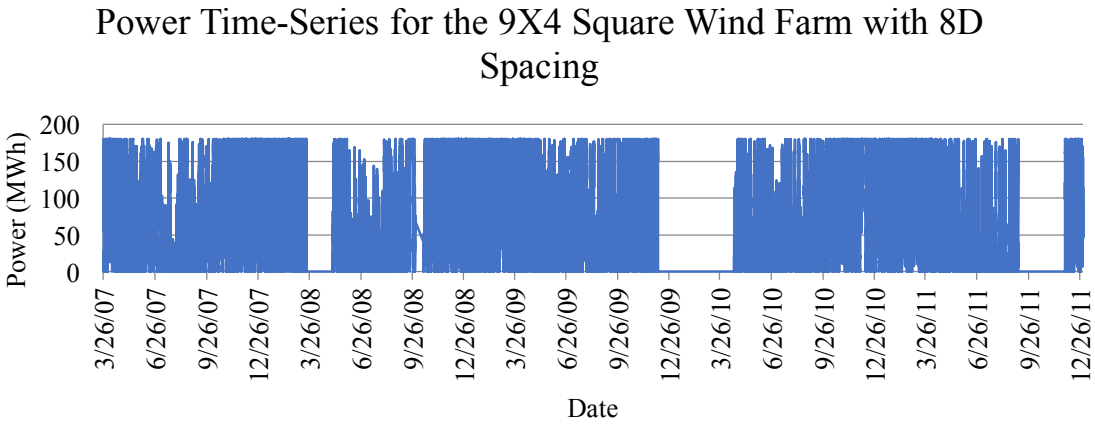

Figure B.4: Power time-series for the 9X4 rectangular wind farm with 8D spacing.

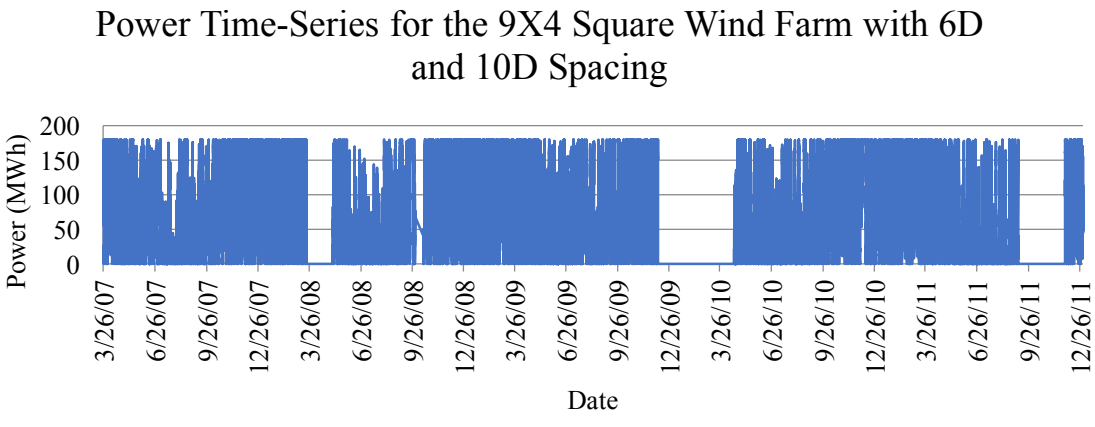

Figure B.5: Power time-series for the 9X4 rectangular wind farm with 6D and 10D spacing.

APPENDIX C

REVENUE TIME-SERIES, ORIENTATIONS, AND TOTALS FOR THE REMAINING CANDIDATE WIND FARMS

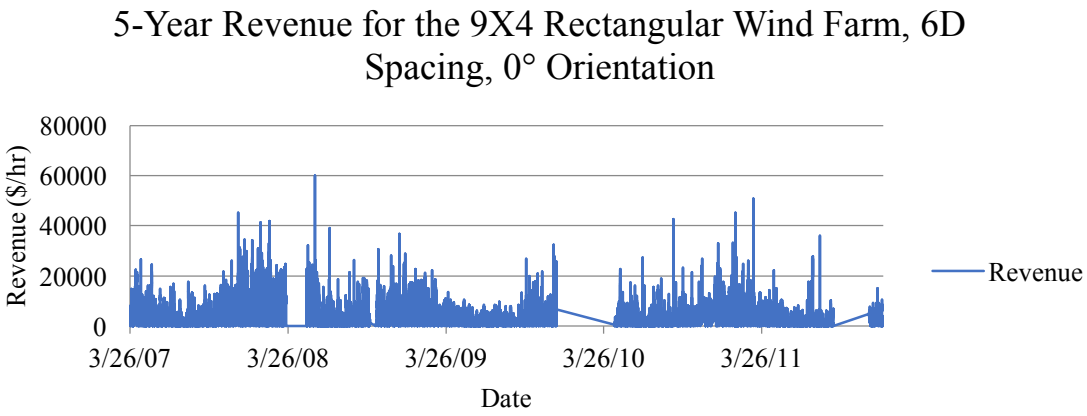

Figure C.1: 5-year revenue time-series for the 9X4 rectangular wind farm, 6D spacing, with a 0° orientation.

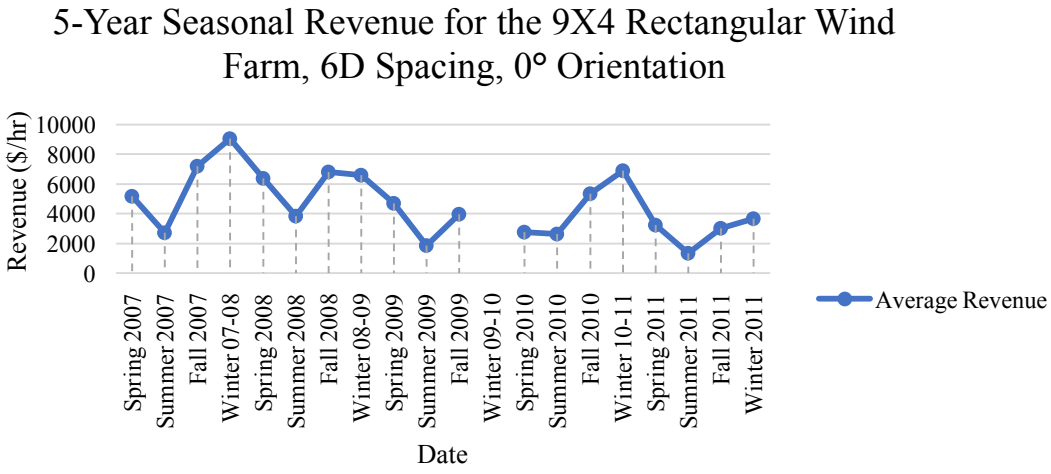

Figure C.2: 5-year seasonal revenue for the 9X4 rectangular wind farm, 6D spacing, with a 0° orientation.

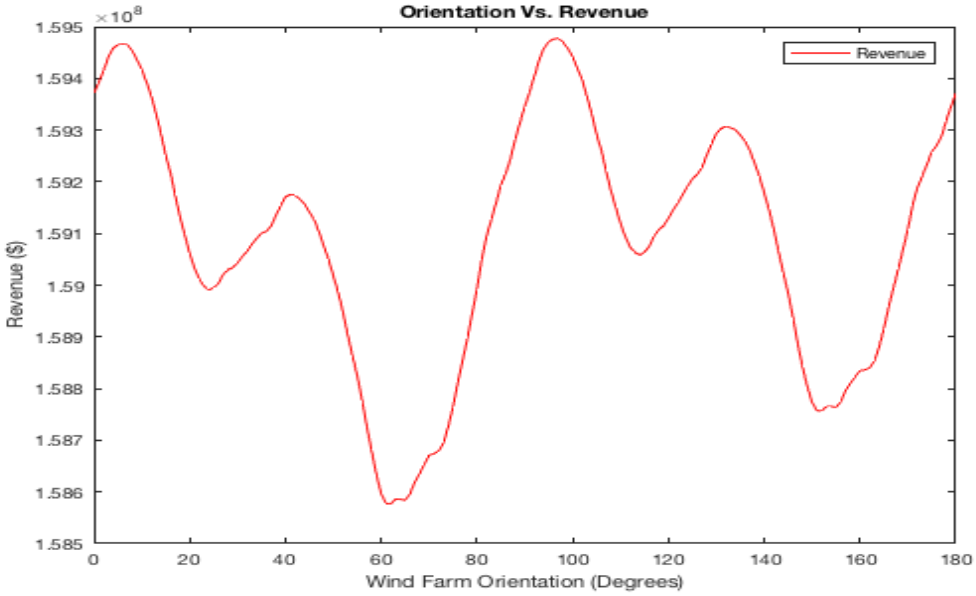

Figure C.3: Total revenue values for the 9X4 rectangular wind farm with 6D spacing at each orientation.

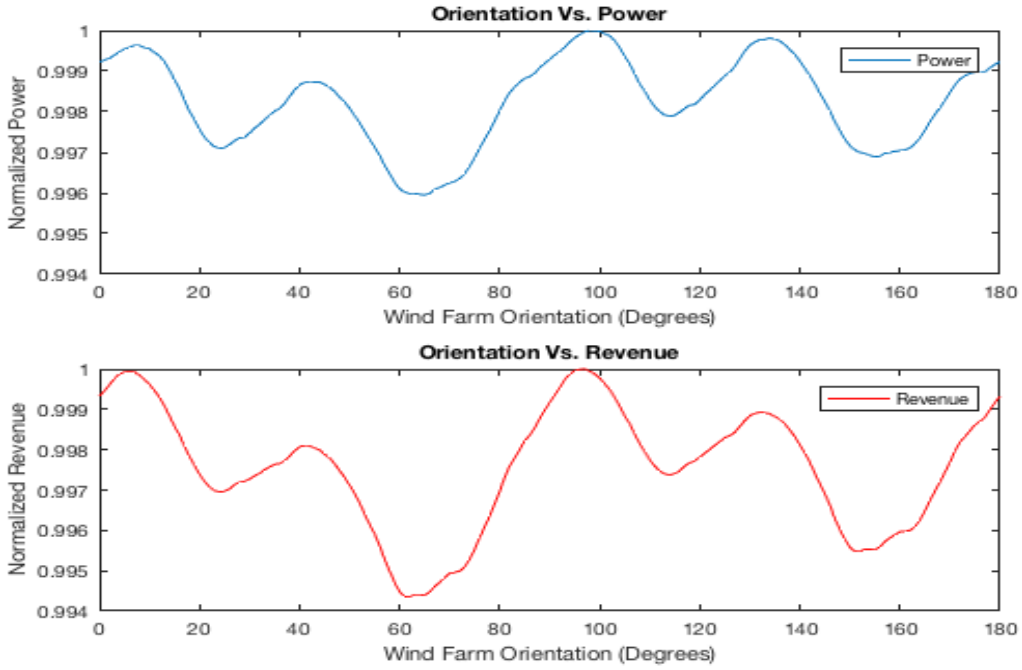

Figure C.4: Relationship between the total revenues and total powers for the 9X4 rectangular wind farm with 6D spacing.

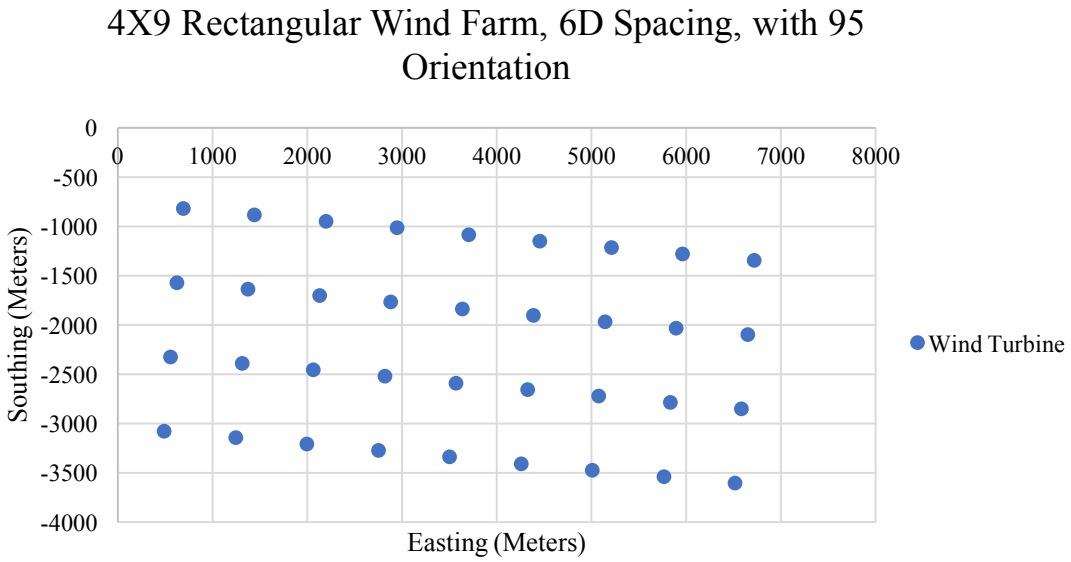

Figure C.5: Orientation that produces the most amount of power and revenue for the 9X4 rectangle wind farm with 6D spacing.

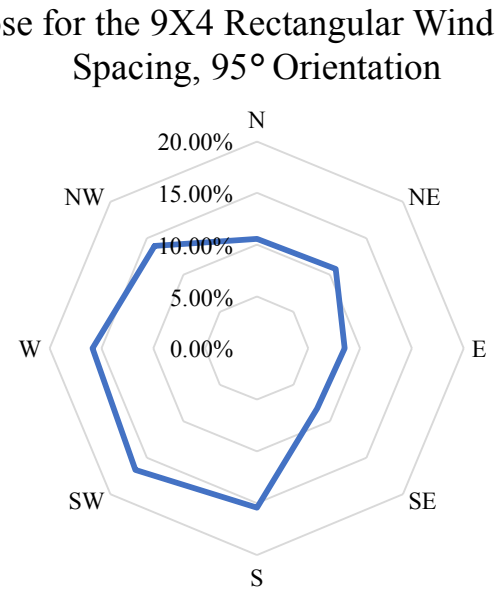

Figure C.6: Wind rose for the 9X4 rectangular wind farm when the orientation is 95°.

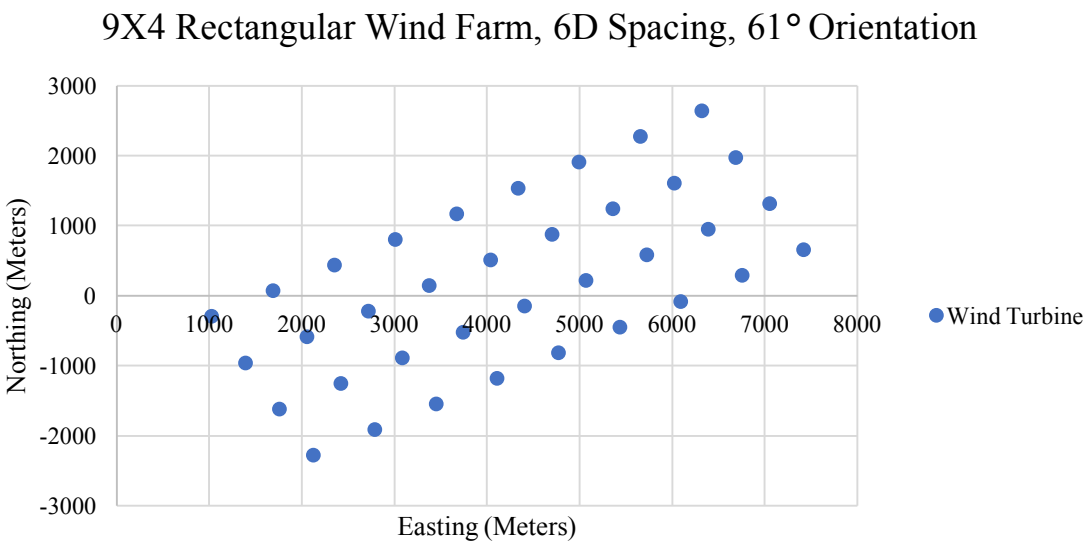

Figure C.7: Orientation that produces the least amount of power and revenue for the 9X4 rectangle wind farm with 6D spacing.

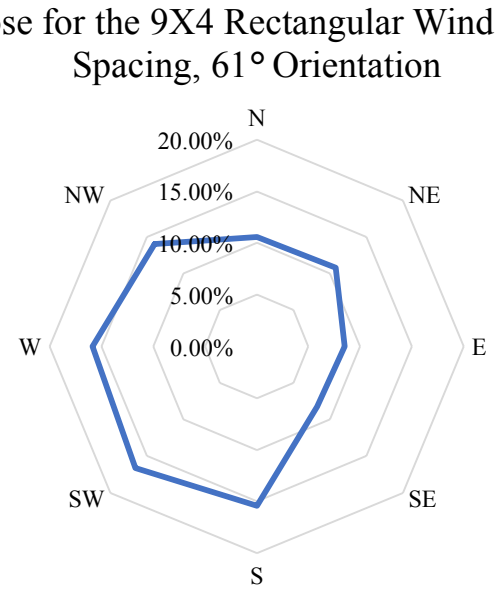

Figure C.8: Wind rose for the 9X4 rectangular wind farm when the orientation is 61°.

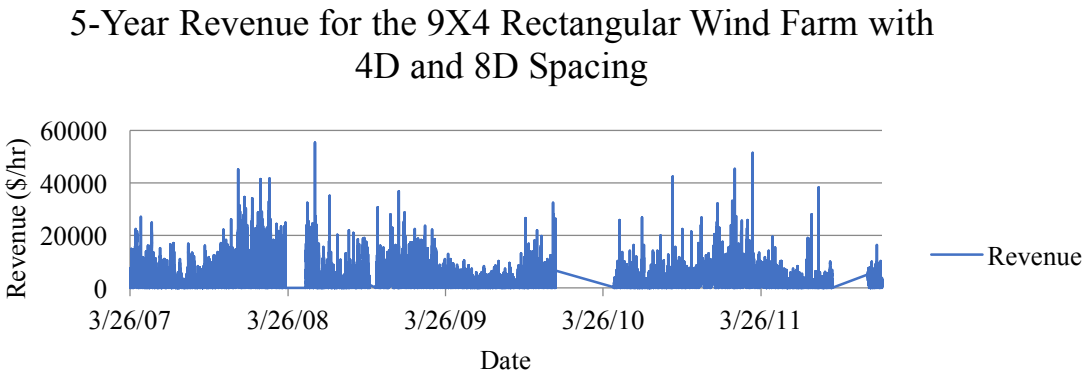

Figure C.9: 5-year revenue time-series for the 9X4 rectangular wind farm, 4D and 8D spacing, at an orientation of 0°.

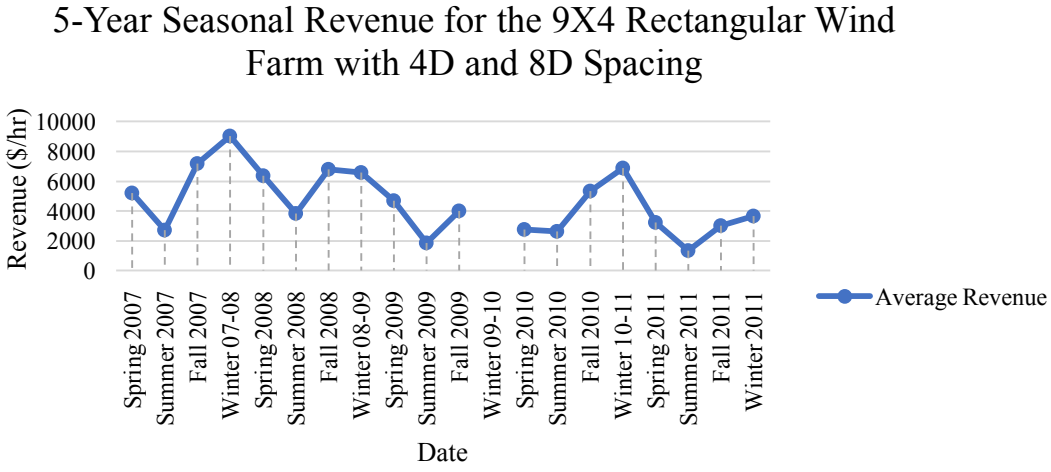

Figure C.10: 5-year average revenues for each season.

Figure C.11: Total revenue values for each orientation of the 9X4 rectangular wind farm with 4D and 8D spacing.

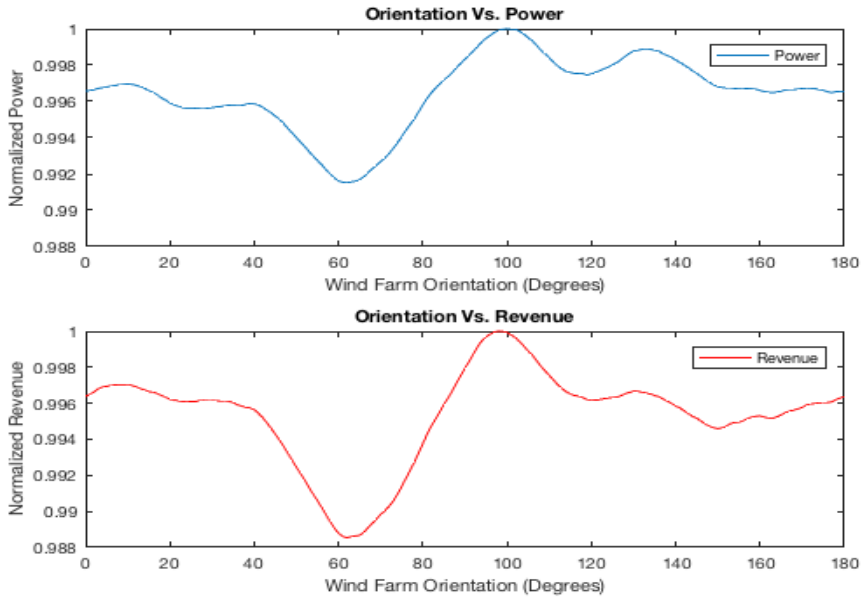

Figure C.12: Total revenue and total power for each orientation of the 9X4 rectangular wind farm with 4D and 8D spacing.

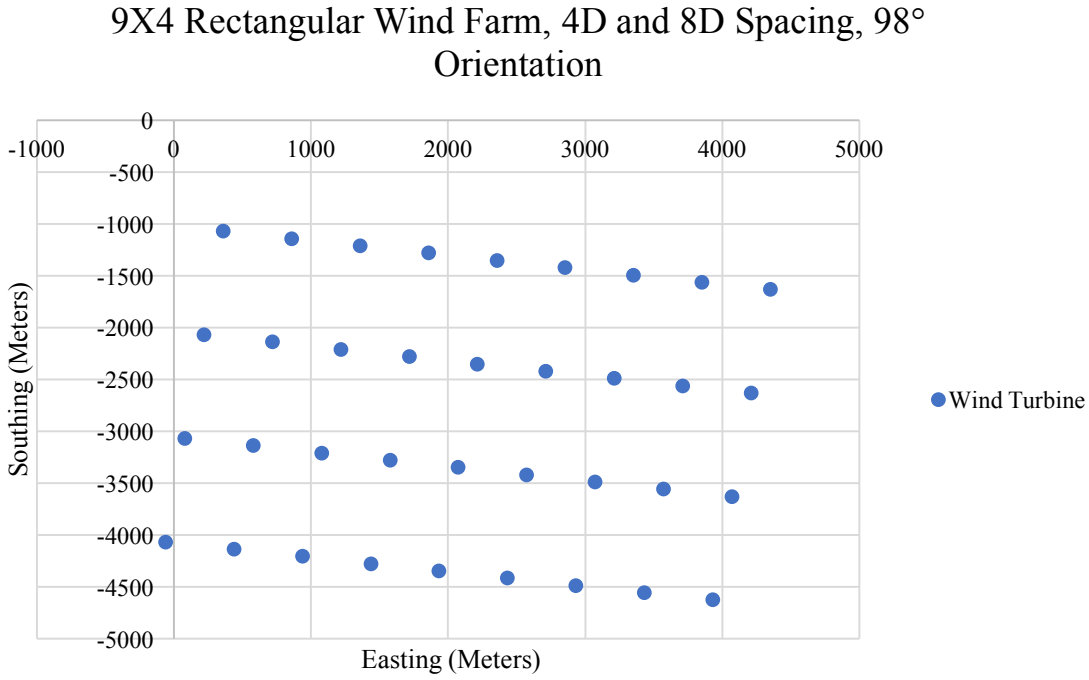

Figure C.13: 9X4 rectangular wind farm, 4D and 8D spacing, with a 98° orientation.

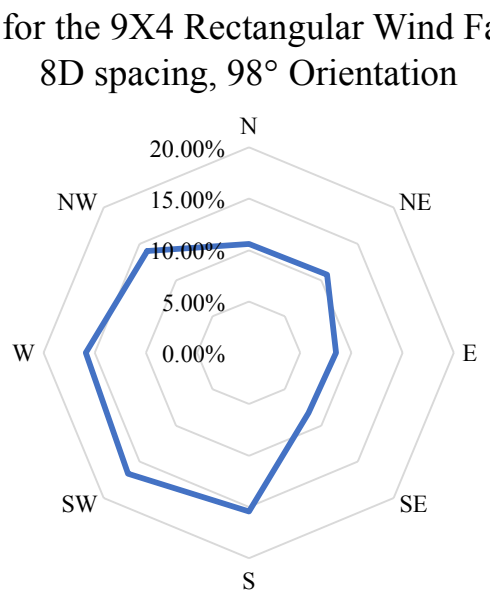

Figure C.14: Wind rose for the 9X4 rectangular wind farm, 4D and 8D spacing, with an orientation of 98°.

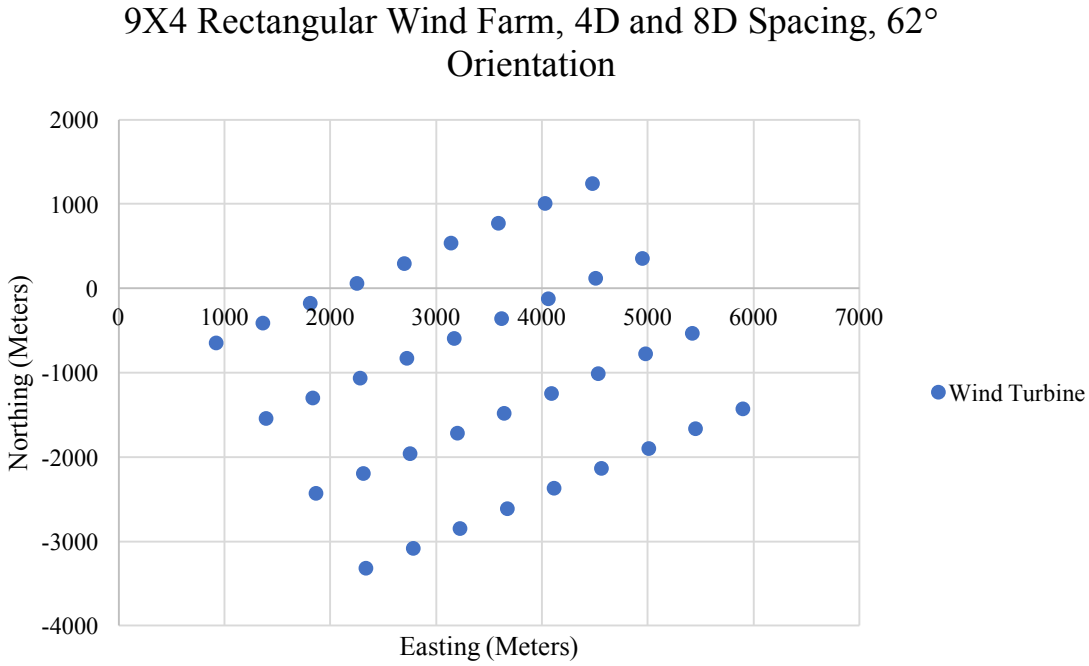

Figure C.15: 9X4 rectangular wind farm, 4D and 8D spacing, with an orientation of 62°.

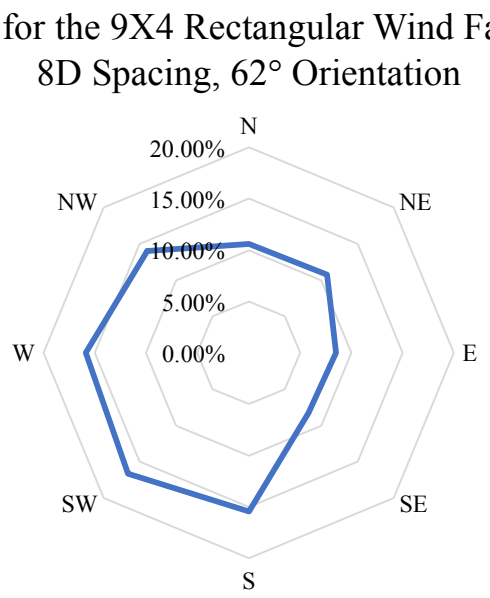

Figure C.16: Wind rose for the 9X4 rectangular wind farm, 4D and 8D spacing, with a 62° orientation.

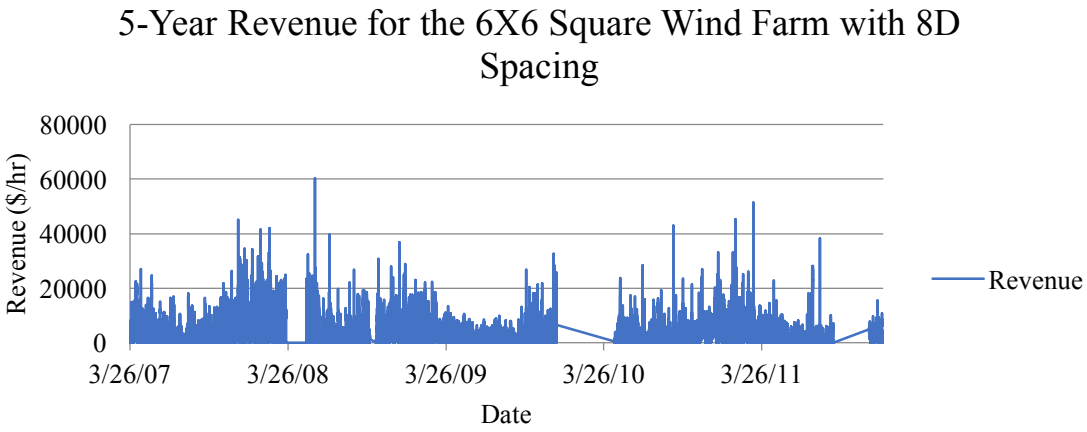

Figure C.17: 5-year revenue time-series for the 6X6 square wind farm with 8D spacing.

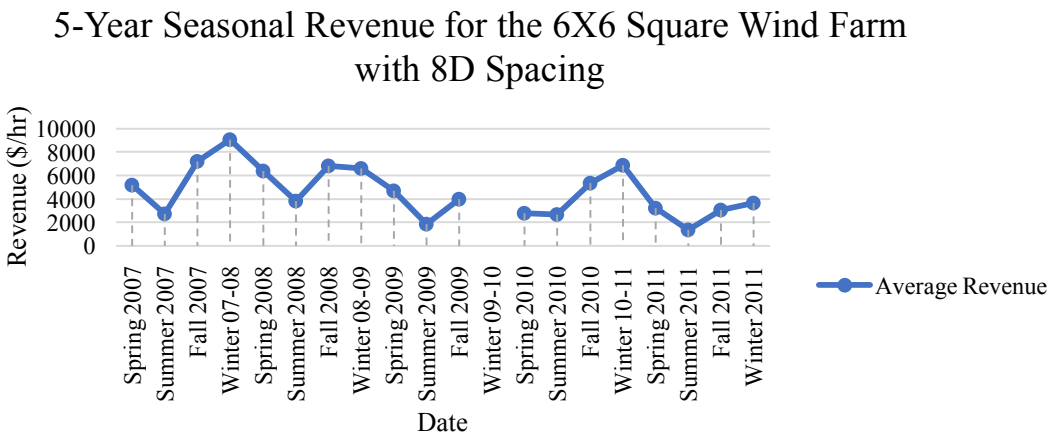

Figure C.18: 5-year average revenue values for each season.

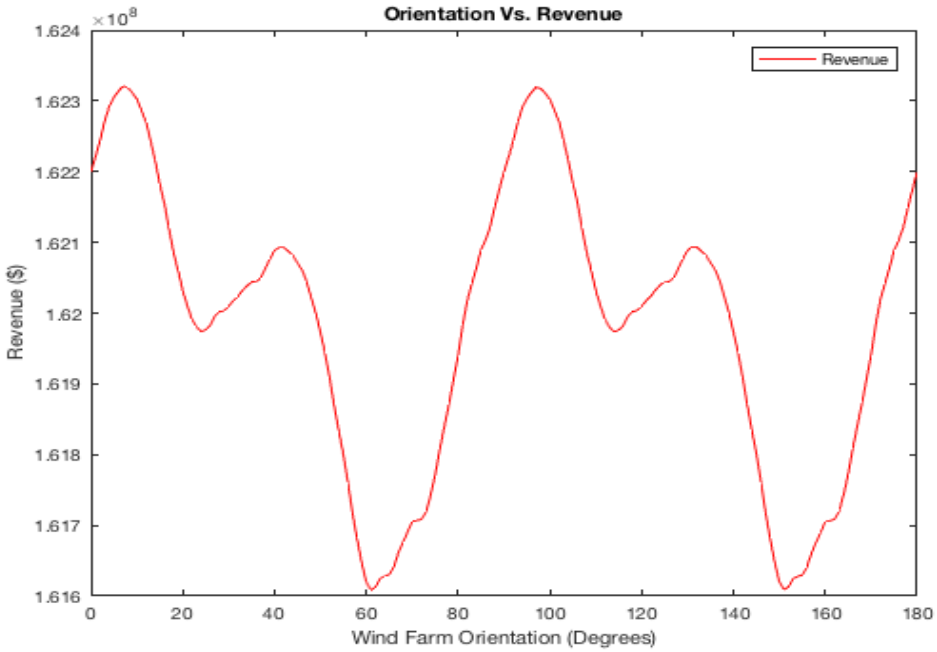

Figure C.19: Total revenue values for each orientation of the 6X6 square wind farm with 8D spacing.

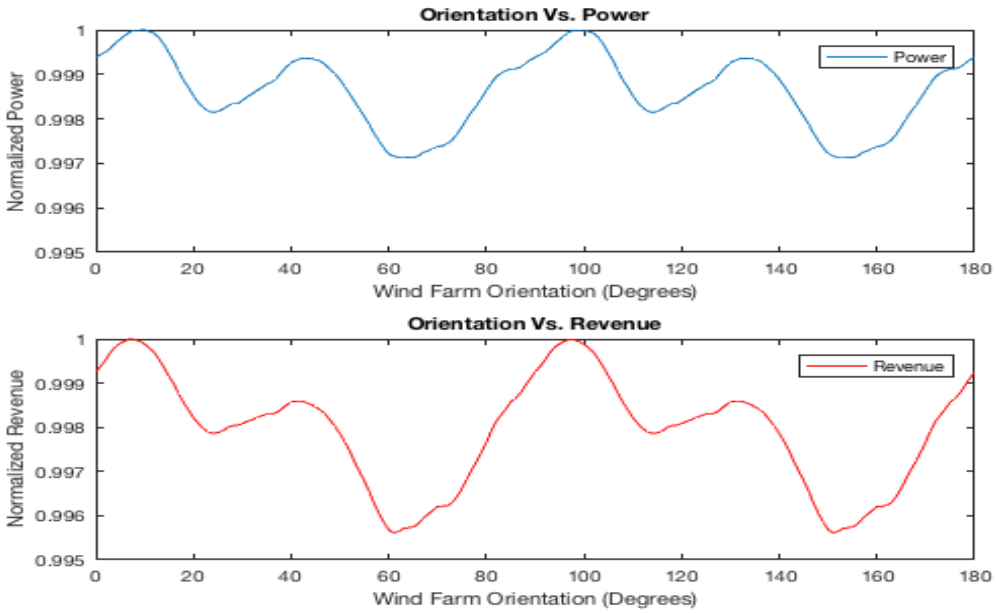

Figure C.20: Total revenue and power values for the 6X6 square wind farm, 8D spacing, at each orientation.

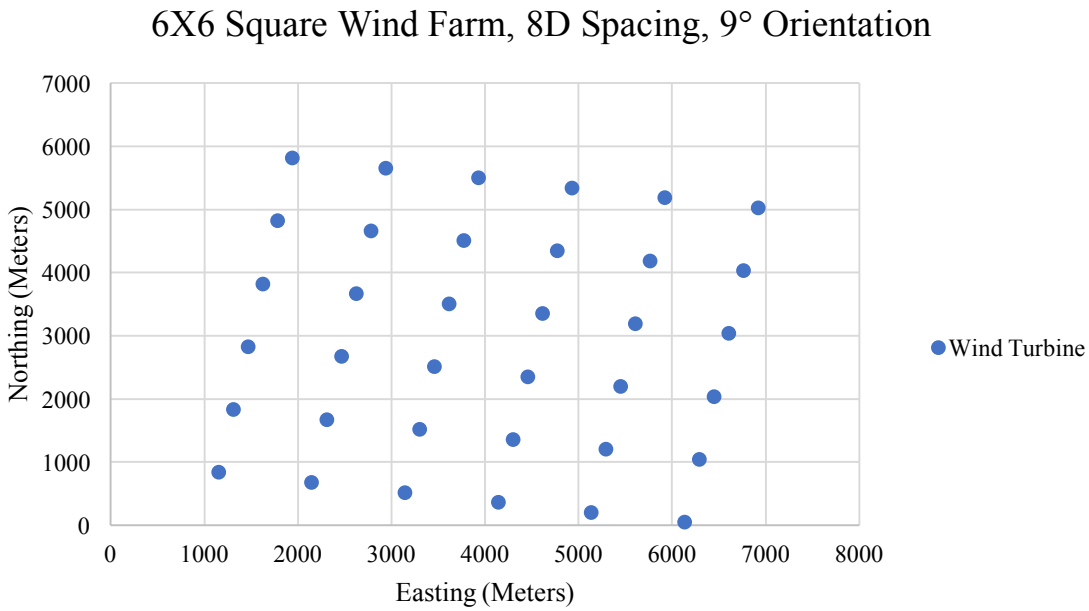

Figure C.21: 6X6 square wind farm, 8D spacing, with a 9° orientation to maximize power and revenue.

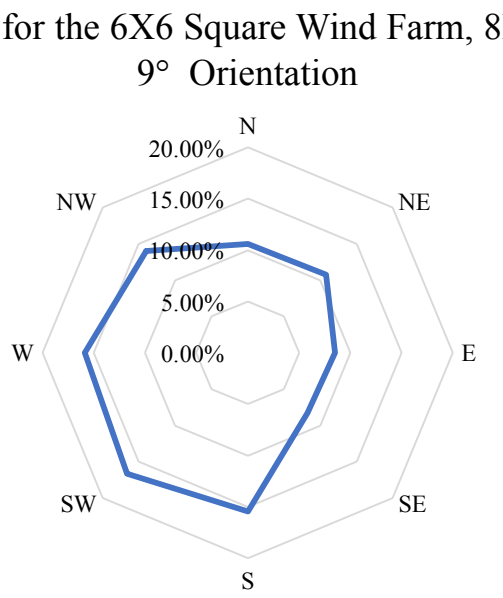

Figure C.22: Wind rose for the 6X6 square wind farm, 8D spacing, with a 9° orientation.

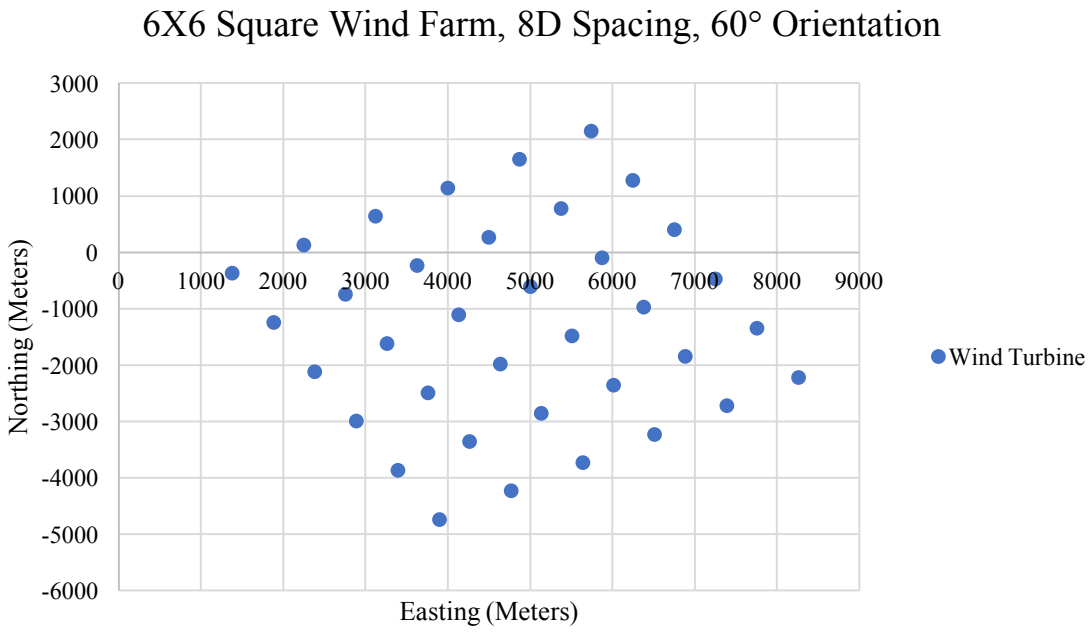

Figure C.23: 6X6 square wind farm, 8D spacing, with a 60° orientation that minimizes power and revenue values.

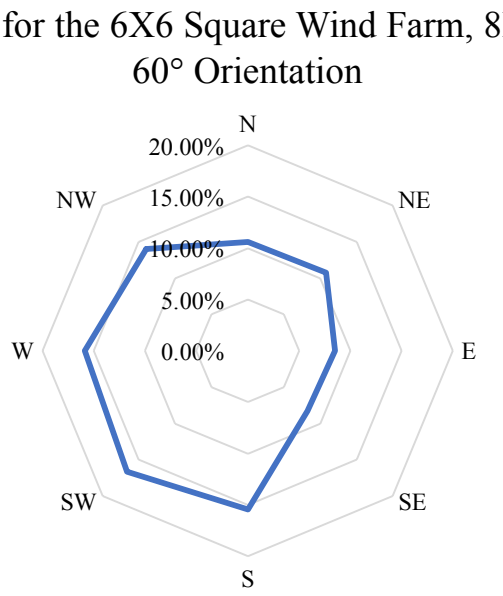

Figure C.24: Wind rose for the 6X6 square wind farm, 8D spacing, with an orientation of 60°.

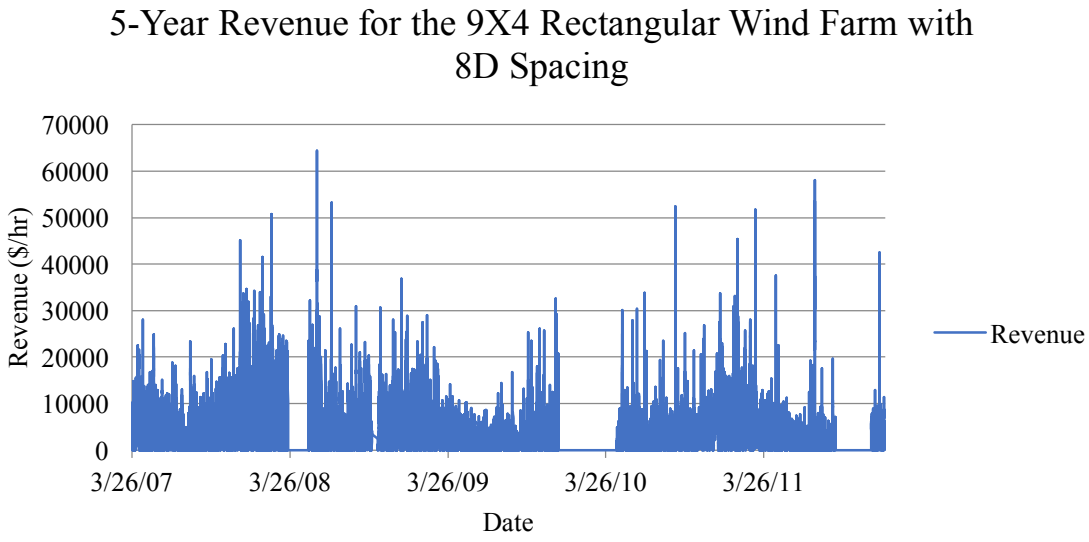

Figure C.25: 5-year revenue time-series for the 9X4 rectangular wind farm with 8D spacing.

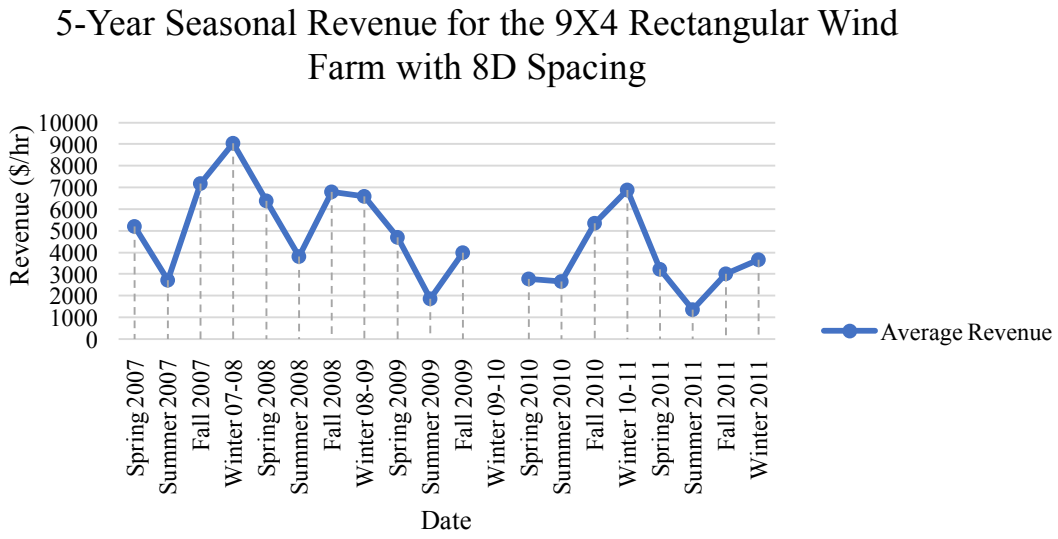

Figure C.26: 5-year seasonal revenue for the 9X4 rectangular wind farm with 8D spacing.

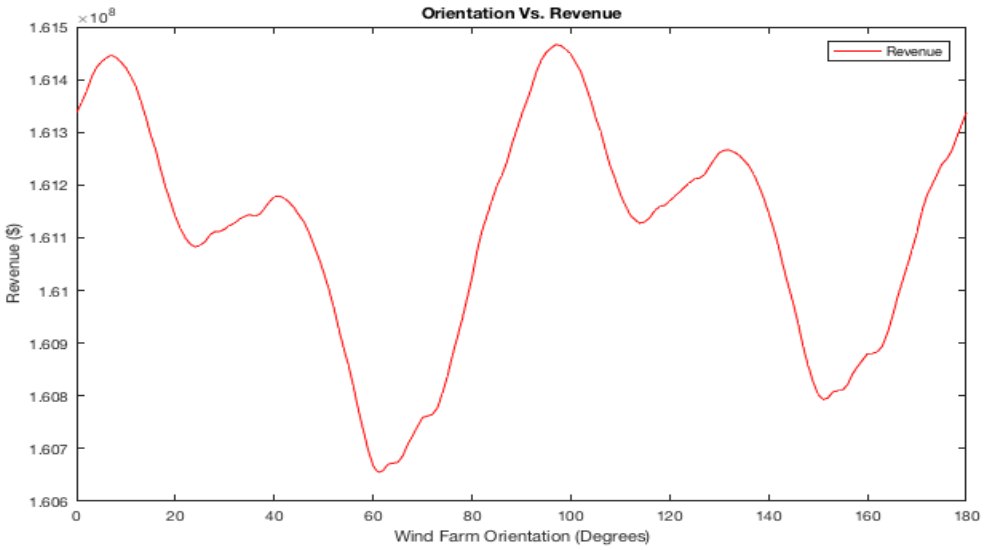

Figure C.27: Total revenue values for each orientation of the 9X4 rectangular farm with 8D spacing.

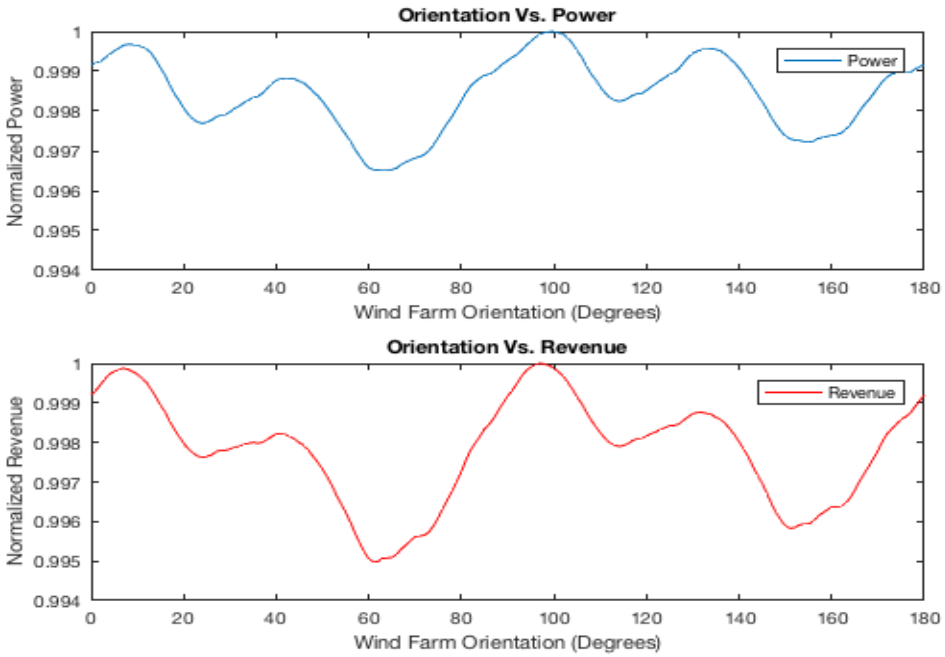

Figure C.28: Total revenue and power totals for each orientation of the 9X4 rectangular farm with 8D spacing.

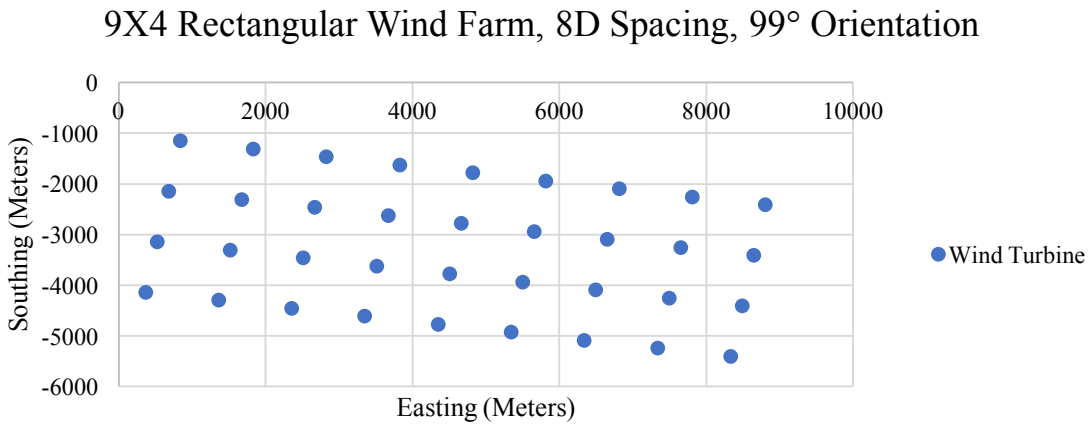

Figure C.29: 99° orientation that maximizes power and revenue for the candidate wind farm.

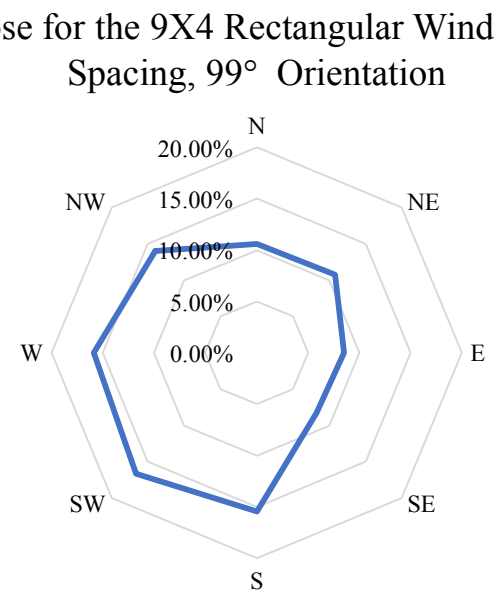

Figure C.30: Wind rose that maximizes power and revenue for the 9X4 rectangular farm with 8D spacing.

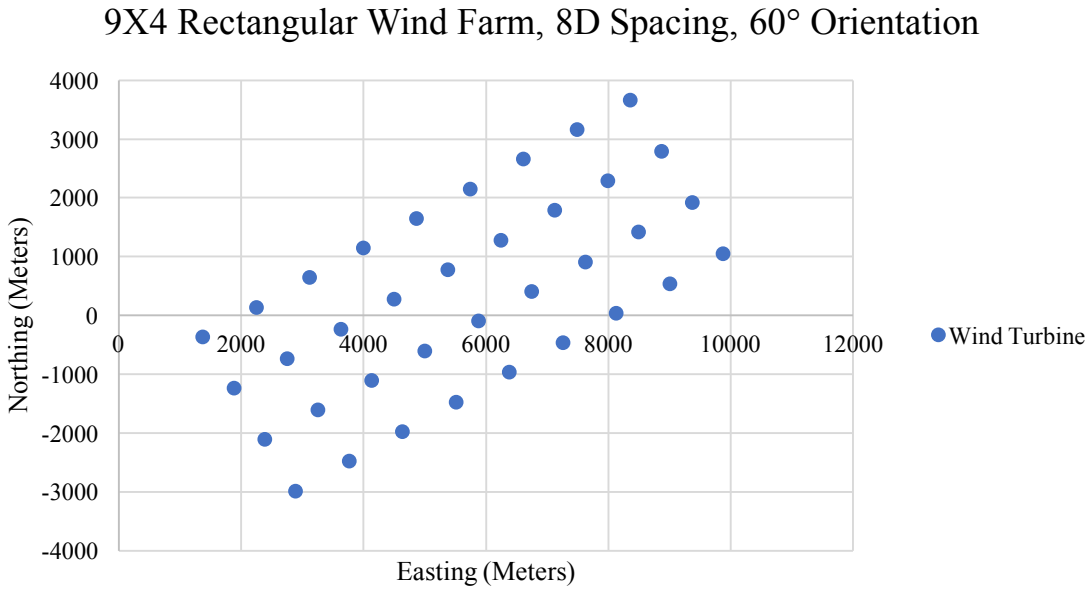

Figure C.31: Orientation that minimizes total power and revenue for the 9X4 rectangular wind farm with 8D spacing.

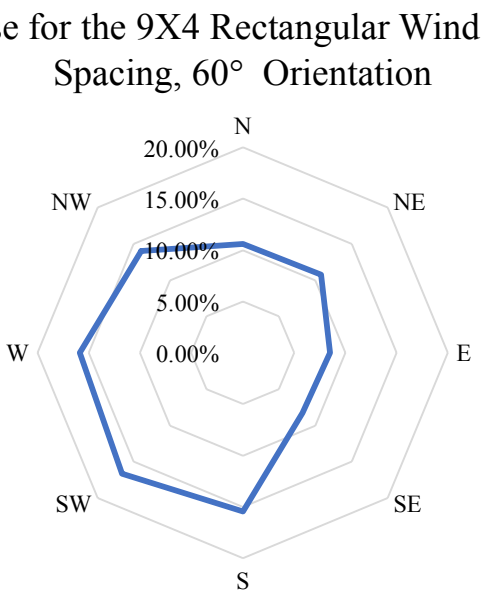

Figure C.32: Wind rose that minimizes total power and revenue for the candidate wind farm.

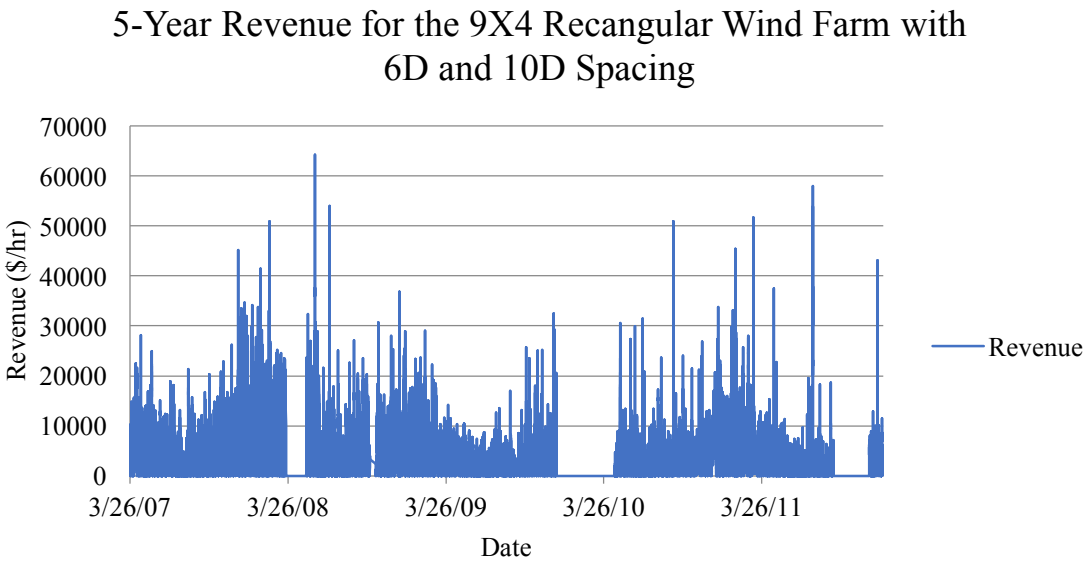

Figure C.33: 5-year revenue time-series for the 9X4 rectangular wind farm with 6D and 10D spacing.

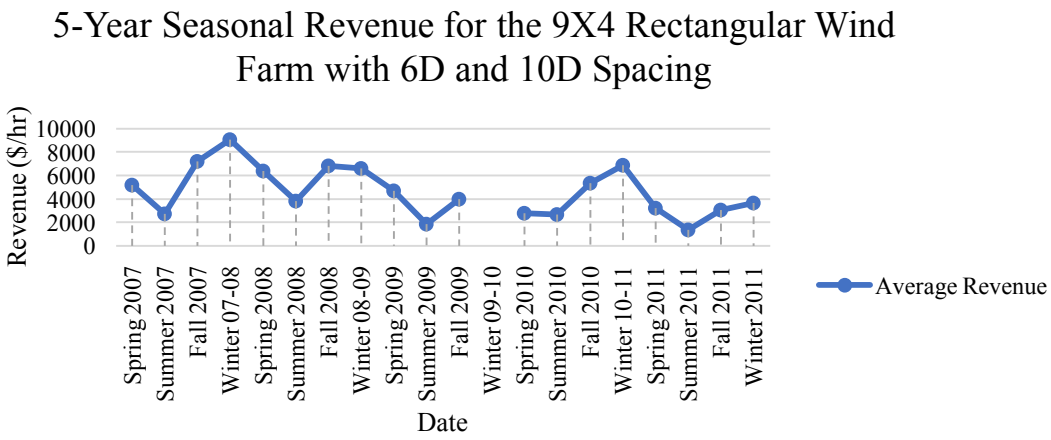

Figure C.34: 5-year seasonal revenue for the 9X4 rectangular wind farm with 6D and 10D spacing.

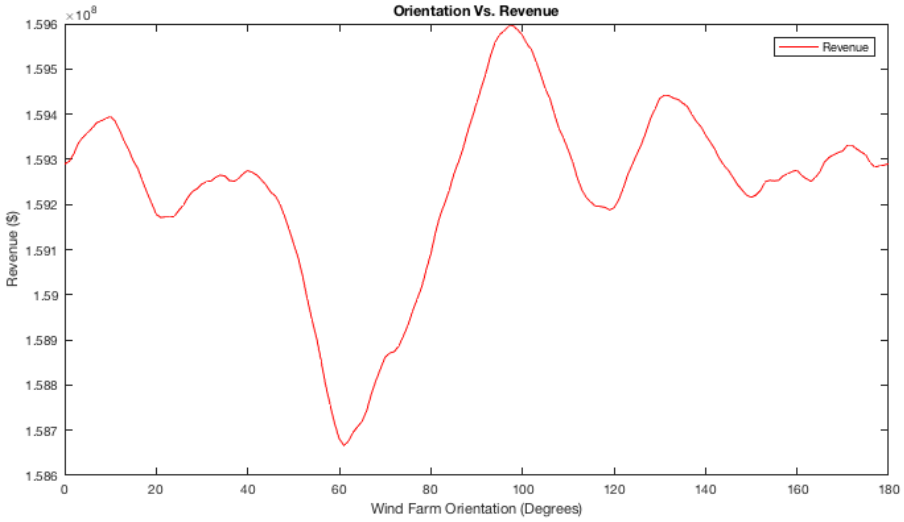

Figure C.35: Revenue totals for each orientation of the candidate wind farm.

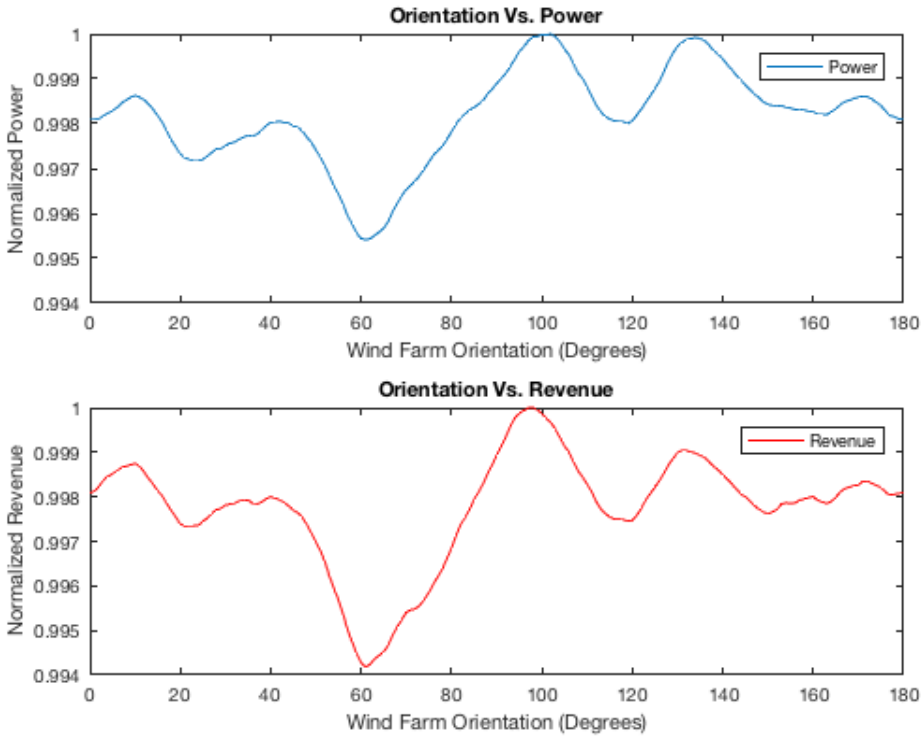

Figure C.36: Power and revenue totals for each orientation of the candidate wind farm.

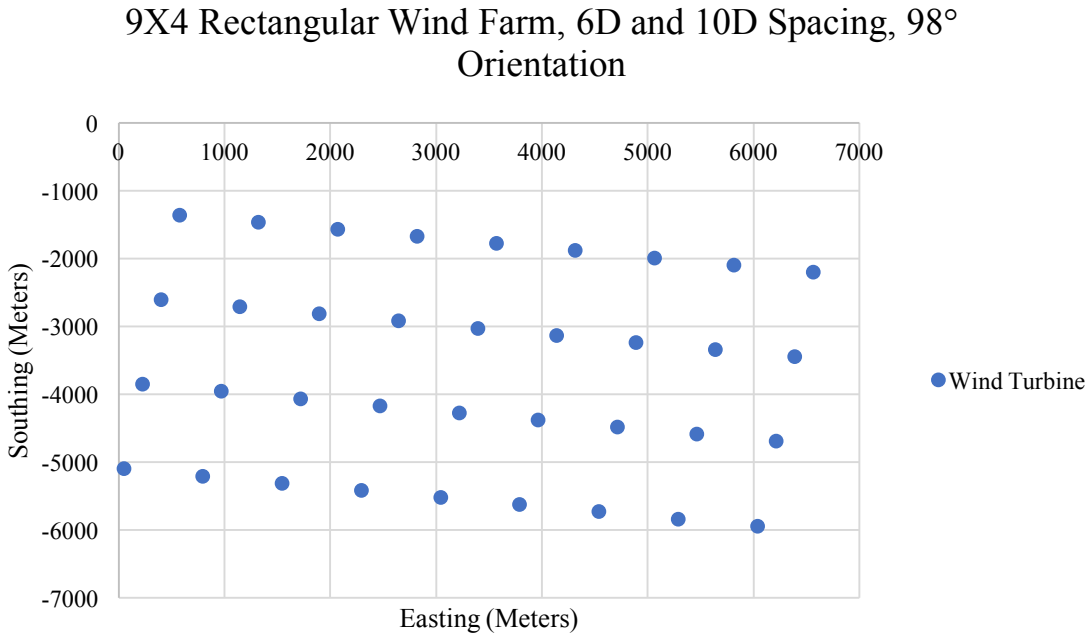

Figure: C.37: Orientation of the candidate wind farm that maximizes revenue and power.

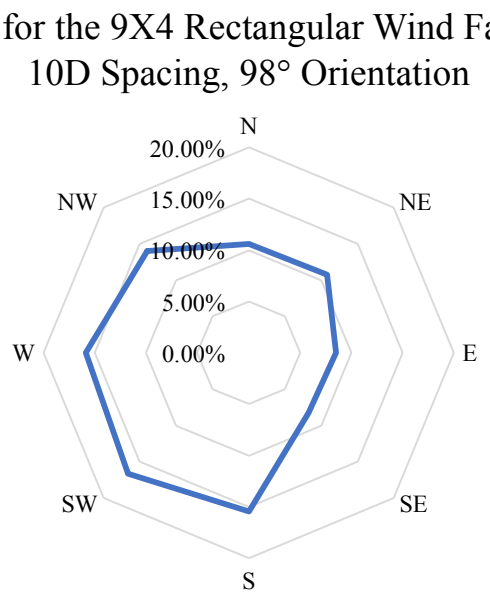

Figure C.38: Wind rose that maximizes revenue and power for the candidate wind farm.

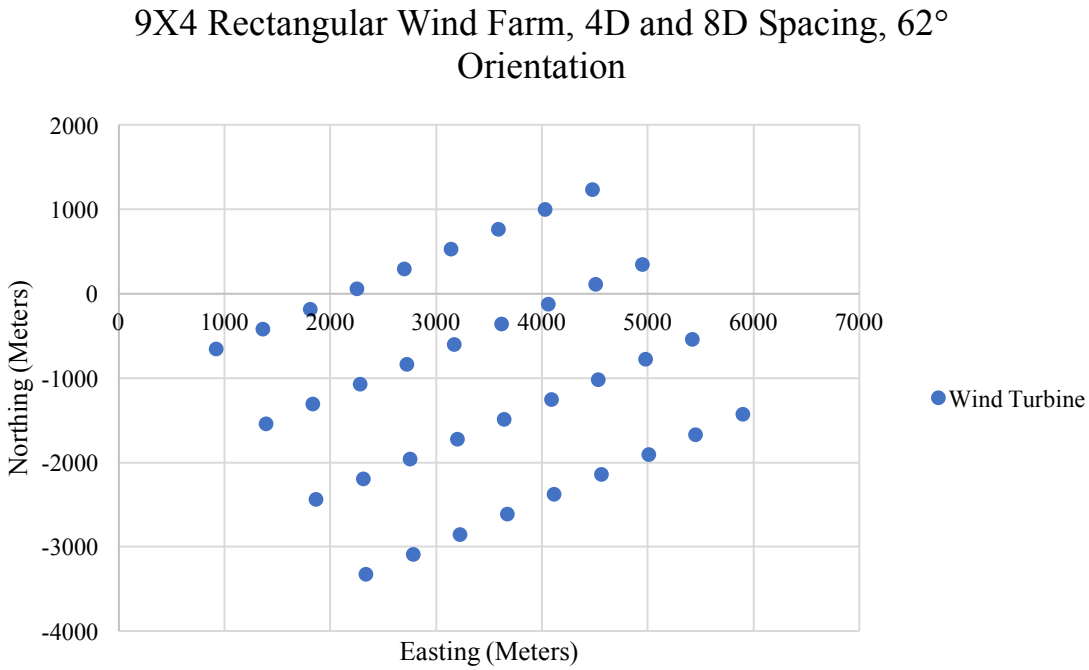

Figure C.39: Orientation that minimizes revenue and power for the candidate wind farm.

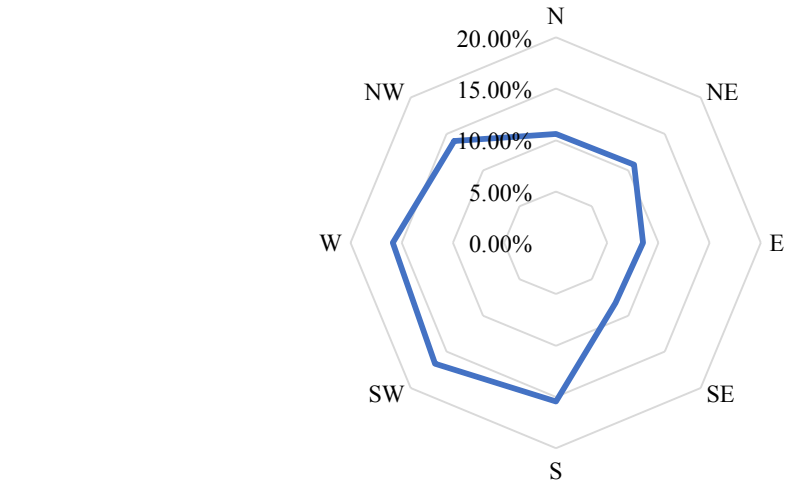

Figure C.40: Wind rose that minimizes revenue and power for the candidate wind farm.

APPENDIX D

MATLAB SCRIPTS FOR THE DWM

This appendix illustrates the MATLAB scripts that were used to run the DWM. This includes a code to run TurbSim and produce a wind file for each wind speed and turbulence intensity, as well as two scripts that alter the input files for FAST. Additionally, the code that runs and parallel processes the DWM simulations with given wind direction, turbulence intensity, and wind speed is given.

Figure D.1 shows the code for TurbSim. This script runs the application with given wind speed and turbulence intensity and then outputs a .wnd file as well as a .bts file.

```
%By: Tim Pfeiffer

function [] = TurbSimFV7()

% Reads and Outputs files in these locations.
TI = [13];
Uambient = [6];

table = [];
file = 'F:\Tim\DWMSquare\5MW_18_4.txt';
outfile_base = 'F:\Tim\DWMSquare\WindFile_TI';
file2 = 'F:\Tim\DWMSquare\5MW_18_4.txt';
outfile2 = 'F:\Tim\DWMSquare\WindFile_TI';

% Loops through array of values changing the TI and Uambient values in the
% 5MW_18_4.txt files.
for i=1:length(TI)
    change.IECturbc = strcat(char(39),num2str(TI(i)),char(39));
    change.URef = Uambient(i);

    % Runs the TurbSim.exe application with the 5MW_18_4.txt file.
    outfile = [outfile2,'_',num2str(TI(i)),'_U_', num2str(Uambient(i)),'.bts'];
    fast_writer(file2,outfile,change,table);
    sys_cmd = strcat('turbsim64
WindFile_TI_',num2str(TI(i)),'_U_',num2str(Uambient(i)),'.bts');
    eval(strcat('system(',char(39) ,sys_cmd ,char(39), ')'));
```

```
end
% Loops through array of values changing the TI and Uambient values in the
% 5MW_18_4.txt files.
for i=1:length(TI)
    change.IECturbc = strcat(char(34),num2str(TI(i)),char(34));
    change.URef = Uambient(i);

    outfile = [outfile_base,'_',num2str(TI(i)),'_U_',
num2str(Uambient(i)),'.wnd'];
    fast_writer(file,outfile,change,table);

    % Runs the TurbSim.exe application with the 5MW_18_4.txt file.
    sys_cmd = strcat('turbsim64
WindFile_TI_',num2str(TI(i)),'_U_',num2str(Uambient(i)),'.wnd');
    eval(strcat('system(',char(39) ,sys_cmd ,char(39), ')'));

end
end
```

Figure D.1: Script to run TurbSim.

Next, two scripts that alter the input files for FAST are given (Figures D.2 and D.3).

```
%By: Tim Pfeiffer

function [] = AeroDynFV7(TI,U,fileBase)

% Reads and Outputs files in these locations.
Table = [];
file2 = 'F:\Tim\DWMR610\DWMSupport\NRELOffshrBsline5MW_AeroDyn.ipt';
outfile2 = strcat(fileBase, '\NRELOffshrBsline5MW_InflowWind');

% Loops through array of values, inputting the WindFiles.
For i=1:length(TI)
    change.WindFile =
strcat(char(39),'WindFile_TI_',num2str(TI(i)),'_U_',num2str(U(i)),'.wnd',
char(39));

    outfile = [outfile2,'_TI_',num2str(TI(i)),'_U_', num2str(U(i)),'.ipt'];
    fast_writer(file2,outfile,change,table);
end
end
```

Figure D.2: Script that alters the .wnd file for FAST.

```
%By: Tim Pfeiffer

function [] = FastGenFV7(TI,U,fileBase)

% Reads and Outputs files in these locations.
table = [];
file = 'F:\Tim\DWMR610\DWMSupport\NRELOffshrBsline5MW_Onshore.fst';
outfile_base = strcat(fileBase, '\NRELOffshrBsline5MW_Onshore');

% Loops through array of values and creates
% NRELOffshrBsline5MW_InflowWind.dat files.
for i=1:length(TI)
    change.ADFile =
strcat(char(34),'NRELOffshrBsline5MW_InflowWind_TI_',num2str(TI(i)),'_U_',num2s
tr(U(i)),'.ipt', char(34));


    outfile = [outfile_base,'_TI_',num2str(TI(i)),'_U_', num2str(U(i)),'.fst'];
    fast_writer(file,outfile,change,table);
end

end
```

Figure D.3: Script that changes the main input file for FAST.

Lastly, the code that runs the DWM and parallel processes the simulations is shown (Figure D.4). Note, two additional scripts, “fast_var_reader” and “fast_writer” are not included in this appendix, but are vital for the application to work properly.

```
%By: Tim Pfeiffer

function [] = runDWMFV7()

% array of Turbulence Intensity, Wind Direction, and Wind Speed values.
TI = [];
U = [];
WD = [];

for i=1:length(WD)
    for j=1:length(TI)
        fileBase = strcat('F:\Tim\DWMR610\',...
                          'DWMExecutions\deg_', int2str(WD(i)),...
                          '\TI_', int2str(TI(j)), '_U_', int2str(U(j)));

        system(['mkdir "' fileBase '"']);
        system(['cd "', fileBase '"']);
        system(['mkdir "', fileBase '\DWM-driver"']);
```

```
        system(['mkdir "', fileBase '\DWM-results"']);

        AeroDynFV7(TI,U,fileBase);
        FastGenFV7(TI,U,fileBase);

        system(['xcopy "F:\Tim\DWMR610\' ...
                'DWMSupport" "', fileBase '"']);
        system(['xcopy "F:\Tim\DWMR610\' ...
                'DWM-driver" "', fileBase '\DWM-driver" /e']);
        system(['xcopy "F:\Tim\DWMR610\' ...
                'WindFiles\TI_', int2str(TI(j)), '_U_',...
                 int2str(U(j)) '" "', fileBase '" /e']);

        table = [];
        windFarmFile = [fileBase '\DWM-driver\wind_farm.txt'];
        % update change var to hold specific WD, TI, and U values
        change.Winddir = WD(i);
        change.TI = TI(j);
        change.Uambient = U(j);
        % change wind farm file for specific WD, TI, and U values
        fast_writer(windFarmFile,windFarmFile,change,table);
    end
end

% loop through array of values running the DWM with each set of values
parfor i=1:length(WD)
    for j=1:length(TI)
        fileBase = strcat('F:\Tim\DWMR610\',...
                          'DWMExecutions\deg_', int2str(WD(i)),...
                          '\TI_', int2str(TI(j)), '_U_', int2str(U(j)));

        % the FastGen file must be in the same folder as the DWM_driver.exe
        % run DWM program using FastGen FAST file
        system(['cd ' fileBase ' & "' fileBase '\DWM_driver_wind_farm.exe" '
fileBase '\NRELOffshrBsline5MW_Onshore_TI_',...
                         num2str(TI(j)),'_U_',num2str(U(j))]);
        % move output files to new location
        destination = strcat('F:\Tim\DWMR610\DWMFinalResults\TI_',...

num2str(TI(j)),'_U_',num2str(U(j)),'_WD_',num2str(WD(i)));
        movefile([fileBase '\DWM-results\*'], destination);
    end
end

% remove execution files
system('rmdir F:\Tim\DWMR610\DWMExecutions /s /q');
end
```

Figure D.4: Script that runs and parallel processes the simulations for the DWM.

BIBLIOGRAPHY

1) "Actuator Disk." N.p., Nov., 2016. <emmanuel.branlard.free.fr/work/paper/htlm/2008ecn/actuatordisk2b.png>.

2) "Analytical modelling of wind speed deficit in large offshore wind farms." Wind Energy 9.1-2 (2006): 39-53.

3) "Block Island Wind Farm." Deepwater Wind. N.p., Nov., 2016. <www.dwwind.com/project/block-island-wind-farm/>.

4) "Horns Rev Wind Farm." Nyheder - Bel Air Aviation A/S. Bel Air, Nov., 2016. <www.mdpi.com/1996-1073/10/3/317/htm>.

5) "Particle Swarm Optimization." Wikipedia. Wikimedia Foundation, Dec., 2016. <https://en.wikipedia.org/wiki/Particle_swarm_optimization>.

6) "The Weather Research & Forecasting Model." The Weather Research&Forecasting Model Website. WRF, Dec., 2016. <www.wrf-model.org/index.php>.

7) "Wind Energy." WIRE. EPFL, 07 Dec. 2010. <www.wire.epfl.ch/page-51662-en.html>.

8) "Wind Rose Diagrams." Wind Rose Diagrams. AutoDesk, Nov., 2016. <http://sustainabilityworkshop.autodesk.com/sites/default/files/styles/large/public/core-page-inserted-images/windrose_freq-dist.png?itok=VEn2sJpr>.

9) "Wind Rose." The Origin Forum. OriginLab, Nov., 2016. <http://www.originlab.com/ftp/forum_and_kbase/images/windrose.png >.

10) "Wind Rose." Wind Rose. NC State University, Nov., 2016. <http://climate.ncsu.edu/dynamic_scripts/windrose/KRDU_windrose.png>.

11) Ainslie, J. F. "Calculating the flowfield in the wake of wind turbines. " Journal of Wind Engineering and Industrial Aerodynamics 27.1-3 (1988): 213-224.

12) Annoni, J., Seiler, P., Johnson, K., Fleming, P., & Gebraad, P. "Evaluating wake models for wind farm control." Proceedings of the American Control Conference (ACC), 2014. IEEE, 2014.

13) Barthelmie, R. J., Frandsen, S. T., Rathmann, O., Hansen, K. S., Politis, E. S., Prospathopoulos, J., Cabezon Martinez, D., Rados, K., Van Der Pijl, S. P., Schepers, J. G., and Schlez, W. "Flow and wakes in large wind farms in complex terrain and offshore." Scientific Proceedings (2008): 0-0.

14) Barthelmie, R. J., Larsen, G. C., Frandsen, S. T., Folkerts, L., Rados, K., Pryor, S. C., Lange, B., and Schepers, G. "Comparison of wake model simulations with offshore wind turbine wake profiles measured by sodar." Journal of atmospheric and oceanic technology 23.7 (2006): 888-901.

15) Barthelmie, R. J., and Jensen, L. E. "Evaluation of wind farm efficiency and wind turbine wakes at the Nysted offshore wind farm." Wind Energy 13.6 (2010): 573-586.

16) Barthelmie, R. J., Hansen, K., Frandsen, S. T., Rathmann, O., Schepers, J. G., Schlez, W., Phillips, J., Rados, K., Zervos, A., Politis, E. S., and Chaviaropoulos, P. K. "Modelling and measuring flow and wind turbine wakes in large wind farms offshore." Wind Energy 12.5 (2009): 431-444.

17) Beyer, H. G., Bernhard, L., and Waldl, H. P. "Modelling tools for wind farm upgrading." European Union Wind Energy Conference, AIAA. 1996.

18) Bianchi, F. D., Mantz, R. J., and Battista, H. G. The Wind and Wind Turbines. Springer London, 2007.

19) Breton, S. P., and Geir, M. "Status, plans and technologies for offshore wind turbines in Europe and North America." Renewable Energy 34.3 (2009): 646-654.

20) Chamorro, L. P., and Porté-Agel, F. "A wind-tunnel investigation of wind-turbine wakes: boundary-layer turbulence effects." Boundary-layer meteorology 132.1 (2009): 129-149.

21) Chowdhury, S., Zhang, J., Messac, A., & Castillo, L. "Unrestricted wind farm layout optimization (UWFLO): Investigating key factors influencing the maximum power generation." Renewable Energy 38.1 (2012): 16-30.

22) Churchfield, M. J., and Lee, S. "NWTC design codes-SOWFA." URL: http://wind. nrel. gov/designcodes/simulator s/SOWFA (2012).

23) Churchfield, M. J., Li, Y., and Patrick J. M. "A large-eddy simulation study of wake propagation and power production in an array of tidal-current turbines." Philosophical Transactions of the Royal Society of London A: Mathematical, Physical and Engineering Sciences 371.1985 (2013): 20120421.

24) Delaunay, D., Chantelot, A., Guyader, T., & Alexandre, P. "Meteodyn WT: A software for wind resource assessment in complex terrain." European Wind Energy Conf., London (UK). 2004.

25) Duckworth, A., and Barthelmie, R. J. "Investigation and validation of wind turbine wake models." Wind Engineering 32.5 (2008): 459-475.

26) Elkinton, C., Manwell, J., and McGowan, J. "Offshore wind farm layout optimization (OWFLO) project: Preliminary results." 44th AIAA aerospace sciences meeting and exhibit. 2006.

27) Elliott, D. L., Wendell, L. L., and Gower, G. L. "An Assessment of the Available Windy Land Area and Wind Energy Potential in the Contiguous United States." Richland, WA: Pacific Northwest National Laboratory, 1991

28) Emami, A., and Noghreh, P. "New approach on optimization in placement of wind turbines within wind farm by genetic algorithms." Renewable Energy 35.7 (2010): 1559-1564.

29) England, ISO New. "ISO New England." ISO New England. ISO New England, Nov., 2016. < https://www.iso-ne.com/>.

30) Fleming, P., Gebraad, P., Van Wingerden, J.W., Lee, S., Churchfield, M., Scholbrock, A., Michalakes, J., Johnson, K., and Moriarty, P. "The SOWFA super-controller: A high-fidelity tool for evaluating wind plant control approaches." Proceedings of the EWEA Annual Meeting, Vienna, Austria. 2013.

31) Fluidyn - Consultancy & Software - CFD & Multiphysics. Fluidyn, Nov., 2016. <http://www.fluidyn.com/fluidyn/>.

32) Frandsen, S., Barthelmie, R., Pryor, S., Rathmann, O., Larsen, S., Højstrup, J., & Thøgersen, M. "Analytical modelling of wind speed deficit in large offshore wind farms." Wind energy 9.1-2 (2006): 39-53.

33) Frandsen, S. T. "Turbulence and turbulence-generated structural loading in wind turbine clusters." Report in draft from Ris (2005).

34) Fyrippis, I., Petros J. A., and Gregoris, P. "Wind energy potential assessment in Naxos Island, Greece." Applied Energy 87.2 (2010): 577-586.

35) González, J. S., Payán, M. B., Santos, J. M. R., & González-Longatt, F. "A review and recent developments in the optimal wind-turbine micro-siting problem." Renewable and Sustainable Energy Reviews 30 (2014): 133-144.

36) González, J. S., Payán, M. B., and Santos, J. R. "Optimum design of transmissions systems for offshore wind farms including decision making under risk." Renewable Energy 59 (2013): 115-127.

37) González, J. S., Rodriguez, A. G. G, Mora, J. C., Santos, J. R., and Payan, M.B. "Optimization of wind farm turbines layout using an evolutive algorithm." Renewable Energy 35.8 (2010): 1671-1681.

38) Grady, S. A., Hussaini, M. Y., and Makola M. A. "Placement of wind turbines using genetic algorithms." Renewable Energy 30.2 (2005): 259-270.

39) Hansen, K. S., Barthelmie, R. J., Jensen, L. E., & Sommer, A. "The impact of turbulence intensity and atmospheric stability on power deficits due to wind turbine wakes at Horns Rev wind farm." Wind Energy 15.1 (2012): 183-196.

40) Hao, Y., and Lackner, M. A. "Wind farm wake modeling using NWTC design codes." Wind Engineering (2016): 0309524X16677883.

41) Hao, Y. "DWM." DWM | NWTC Information Portal. NREL, 2015. <https://nwtc.nrel.gov/DWM>.

42) Jensen, N. O. "A Note on Wind Generator Interaction." Risø National Laboratory 1983.

43) Jonkman, B. J. "TurbSim user's guide: Version 1.50." National Renewable Energy Laboratory, Golden, CO, Technical Report No. NREL/TP-500-46198 (2009).

44) Jonkman, J. M., and Buhl, M. L. Jr. "FAST user's guide." National Renewable Energy Laboratory, Golden, CO, Technical Report No. NREL/EL-500-38230 (2005).

45) Katic, I., Højstrup, J., and Jensen, N. O. "A simple model for cluster efficiency." European Wind Energy Association Conference and Exhibition. 1986.

46) Kusiak, A., and Song, Z. "Design of wind farm layout for maximum wind energy capture." Renewable Energy 35.3 (2010): 685-694.

47) Lackner, M. A., and Elkinton, C. N. "An analytical framework for offshore wind farm layout optimization." Wind Engineering 31.1 (2007): 17-31.

48) Larsen, G. C., Madsen, H. A., Thomsen, K., and Larsen, T. J. "Wake meandering: a pragmatic approach." Wind Energy 11.4 (2008): 377-395.

49) Larsen, G. C., Madsen, H. A., Bingol, F., Mann, J., Ott, S., Sorensen, J. N., Okulov, V., Troldborg, N., Nielsen, N. M., Thomsen, K., and Larsen, T. J. "Dynamic wake meandering modeling." Risø National Laboratory, 2007.

50) Larsen, G. C., Højstrup, J., and Madsen, H. A. "Wind fields in wakes." 1996 European Union wind energy conference (1996).

51) Ltd, OpenCFD. "OpenFoam" The Open Source CFD Toolbox, User's Manual, Version 2.1.0 (2009).

52) Mann, J. "Wind field simulation." Probabilistic engineering mechanics 13.4 (1998): 269-282.

53) Manwell, J. F., McGowan, J. G., and Rogers, A. L. "Wind energy explained: theory, design and application." John Wiley & Sons, 2010.

54) Marden, J., Ruben, S., and Pao, L. "Surveying game theoretic approaches for wind farm optimization." 50th AIAA Aerospace Sciences Meeting including the New Horizons Forum and Aerospace Exposition. 2012.

55) Messac, A., Chowdhury, S., and Zhang, J. "Characterizing and mitigating the wind resource-based uncertainty in farm performance." Journal of Turbulence 13 (2012): N13.

56) Meyers, J., and Meneveau, C. "Optimal turbine spacing in fully developed wind farm boundary layers." Wind Energy 15.2 (2012): 305-317.

57) Mikkelsen, R. "Actuator disc methods applied to wind turbines." Diss. PhD thesis, Technical University of Denmark, 2003.

58) Moeng, C. H., and Sullivan, P. P. "Large eddy simulation." Encyclopedia of Atmospheric Sciences 1140 (2002): 1150.

59) Moriarty, P. J., and Hansen, A. C. "AeroDyn theory manual". Golden, CO: National Renewable Energy Laboratory, 2005.

60) Mortensen, N. G., Heathfield, D.N., Rathmann, O., and Nielsen, M. "Wind atlas analysis and application program: WAsP 10 Help Facility." http://www.wasp.dk/Download/General/~/media/Risoe_dk/WAsP/Download/WAsP/Helpfiles/Wasp (2011).

61) Mosetti, G. P. C. D. B., Poloni, C., and Diviacco, B. "Optimization of wind turbine positioning in large windfarms by means of a genetic algorithm." Journal of Wind Engineering and Industrial Aerodynamics 51.1 (1994): 105-116.

62) Musial, W., Parker, Z., Fields, J., Scott, G., Elliot, D., and Dracl, C. "Assessment of Offshore Wind Energy Leasing Areas for the BOEM Massachusetts Wind Energy Area." Technical Report. NREL/TP-5000-60942. NREL, Golden, CO (US). http://www.nrel.gov/docs/fy14osti/60942.pdf, 2013.

63) Oh, K. Y., Kim, J. Y., Lee, J. K., Ryu, M. S., and Lee, J. S. "An Assessment of Wind Energy Potential at the Demonstration Offshore Wind Farm in Korea." Energy. 46.1 (2012): 555-563. Print.

64) Ozturk, U. A., and Norman, B. A. "Heuristic methods for wind energy conversion system positioning." Electric Power Systems Research 70.3 (2004): 179-185.

65) Rados, K., Larsen, G., Barthelmie, R., Schlez, W., Lange, B., Schepers, G., Hegberg, T., and Magnisson, M. "Comparison of wake models with data for offshore windfarms." Wind Engineering 25.5 (2001): 271-280.

66) Sanderse, and B., Koren, B. "Energy Preservation in the Numerical Calculation of Wind Turbine Wakes." Wind Turbine Wakes (2009): 16.

67) Shen, W. Z. "Numerical modeling of wind turbine wakes." J. Fluids Eng 124.2 (2002): 393-399.

68) Sørensen, J. N. "Aerodynamic aspects of wind energy conversion." Annual Review of Fluid Mechanics 43 (2011): 427-448.

69) Steele, K. E., and Mettlach, T. "NDBC wave data—current and planned." Ocean Wave Measurement and Analysis: ASCE, 1993.

70) Stewart, G. M., Robertson, A., Jonkman, J., & Lackner, M. A. "The creation of a comprehensive metocean data set for offshore wind turbine simulations." Wind Energy (2015).

71) Stull, R. B. "An introduction to boundary layer meteorology." Vol. 13. Springer Science & Business Media, 2012.

72) Thørgersen, M. L., Sorensen, T., Nielsen, P., Grotzner, A., and Chen, S. "WindPRO/PARK: introduction to wind turbine wake modelling and wake generated turbulence." EMD International A/S, Aalborg, Denmark (2005).

73) Troldborg, N., Sørensen, J. N., and Mikkelsen, R. "Actuator line simulation of wake of wind turbine operating in turbulent inflow." Journal of physics: conference series. Vol. 75. No. 1. IOP Publishing, 2007.

74) VanLuvanee, D. R. "Investigation of observed and modeled wake effects at Horns Rev using WindPRO." Technical University of Denmark Department of Mechanical Engineering (2006).

75) Wallbank, T. "WindSim Validation Study." CFD validation in Complex terrain (2008).

76) Wan, C., Wang, J., Yang, G., & Zhang, X. "Optimal micro-siting of wind farms by particle swarm optimization." Advances in swarm intelligence, 2010.

77) Wang, H., Barthelmie, R., Pryor, S. C., and Kim, H. G. "A new turbulence model for offshore wind turbine standards." Wind Energy 17.10 (2014): 1587-1604.

78) Weibull, W. "A statistical distribution function of wide applicability." Journal of applied mechanics 18.3 (1951): 293-297.

79) Wu, Y. T., and Porté-Agel, F. "Atmospheric turbulence effects on wind-turbine wakes: An LES study." Energies 5.12 (2012): 5340-5362.